MICROWAVE IMAGING USING TIME REVERSAL TECHNIQUES AND RESOLUTION ENHANCEMENT IN DISPERSIVE MEDIA

A thesis submitted to The University of Manchester
for the degree of Doctor of Philosophy
in the Faculty of Science and Engineering

2021

Loukas Xanthos

Department of Electrical and Electronic Engineering
Control, Communications and Signal Processing division

Contents

List of Tables

List of Figures

List of Acronyms

AWGN	Additive White Gaussian Noise
CF	Centre Frequency
CFS-PML	Complex Frequency-Shifted Perfectly Matched Layer
CWT	Continuous Wavelet Transform
DFT	Discrete Fourier Transform
DHP	Digital Human Phantom
DORT	Décomposition de l'Opérateur de Retournement Temporel – English: Decomposition of the TR Operator
DTWT	Discrete Time Wavelet Transform
$(FD)^2TD$	Frequency-Dependent Finite Difference Time Domain
FDTD	Finite Difference Time Domain
FFT	Fast Fourier Transform
FQ-MUSIC	Frequency-selective MUSIC
GPR	Ground Penetrating Radar
IDTWT	Inverse Discrete Time Wavelet Transform
LHS	Left-Hand Side
MDM	Multistatic Data Matrix
MISO	Multiple-Input Single-Output
MTI	Moving Target Indication
MUSIC	MUltiple SIgnals Classification
PEC	Perfect Electric Conductor
RHS	Right-Hand Side
SAR	Synthetic Aperture Radar
SNR	Signal-to-Noise Ratio

STFT	Short-Time Fourier Transform
SVD	Singular Value Decomposition
TR	Time Reversal
TR-MUSIC	Time Reversal MUSIC
TRA	Time Reversal Array
TRO	Time Reversal Operator
TWRI	Through-the-Wall Radar Imaging
UWB	Ultra WideBand
UWB-MUSIC	Ultra WideBand MUSIC
WF-MUSIC	Window- and Frequency- selective MUSIC

List of Symbols

$\lceil\,\rceil$	The ceiling function, i.e. $\lceil A \rceil$ is the smallest integer no smaller than A, for every real number A
$\lfloor\,\rfloor$	The floor function, i.e. $\lfloor A \rfloor$ is the largest integer no greater than A, for every real number A
$\langle\,,\rangle$	Inner product
$\|\,\|$	Norm
$\star$	Correlation in time
$*$	Convolution in time
*	(in superscript) The complex conjugation operation
∇^2	Vector Laplacian
$\mathit{\Gamma}$	Attenuation model in the wavelet domain
$\mathit{\Delta}_a$	The DTWT scale step
Δh	Length of the (uniform) spatial step of a FDTD simulation
Δt	Duration of the time step of a FDTD simulation
$\boldsymbol{K}$	The full MDM
$\boldsymbol{K}_{\mathbf{d}}$	The differential MDM
$\boldsymbol{K}_{\mathbf{d}l}$	The l-th spatial window of the spatially windowed $\boldsymbol{K}_{\mathbf{d}}$
$\boldsymbol{K}_{\mathbf{d}l,m}$	The m-th temporal window of the l-th spatial window of the spatially and temporally windowed $\boldsymbol{K}_{\mathbf{d}}$
Ω	Set of frequencies of interest

Ω_k	Range of frequency bins of interest
C_δ	The reconstruction constant of the wavelet transform
$\mathcal{F}^{-1}\{\,\}$	Inverse Fourier transform
$\boldsymbol{F}$	A vector field
G	$G(\boldsymbol{r}_i, \boldsymbol{r}_p, t)$ is the background Green function between locations $\boldsymbol{r}_i$ and $\boldsymbol{r}_p$
H	Inverse filter in the wavelet domain
H_{s}	Stabilised inverse filter in the wavelet domain
$^{\mathrm{H}}$	$\boldsymbol{A}^{\mathrm{H}}$ denotes the Hermitian transpose (conjugate transpose) of $\boldsymbol{A}$
J	The largest DTWT scale index, which corresponds to the largest resolvable DTWT scale factor
L	Total number of spatial windows used for a spatial windowing process
M	Total number of temporal windows used for a temporal windowing process
$\mathcal{M}_{l,m}$	The non-normalised radar image corresponding to the l-th spatial and m-th temporal window
$\tilde{\mathcal{M}}_{l,m}$	The normalised radar image corresponding to the l-th spatial and m-th temporal window
$\tilde{\mathcal{M}}$	The final radar image
N	Total number of samples
$\mathcal{N}$	Total number of TRA elements
$\mathcal{N}^{\Theta}$	The dimension of the signal subspace of the MDM
$\mathcal{N}_{\mathrm{sw}}$	Number of TRA elements in each spatial window
P	Duration of a temporal window
Q	Total number of scatterers

R_{A}	The resolution of the spatial focusing at the time of refocusing using the dispersion compensation method proposed by Abduljabbar *et al.*, 2017
R_{TR}	The resolution of the spatial focusing at the time of refocusing using the conventional TR approach with no dispersion compensation
R_{P}	The resolution of the spatial focusing at the time of refocusing using the compensation approach proposed in this thesis
$\mathrm{Re}\{\,\}$	Real part of its complex argument
R_{ref}	The resolution of the spatial focusing in the reference lossless propagation medium at the time of refocusing using the conventional TR approach with no dispersion compensation
$\tilde{\hat{S}}$	Normalised frequency spectrum
S	A short UWB pulse
$^{\mathrm{T}}$	$\boldsymbol{A}^{\mathrm{T}}$ denotes the transpose of $\boldsymbol{A}$
T_{s}	Sampling period
T_{shift}	Constant time shift
W	A window function in the discrete time domain
Y	Output (compensated) signal in the wavelet domain
α	Attenuation factor
γ	Attenuation in the time domain
δ	The Dirac delta function
ε	Permittivity (real)
ϵ	Complex permittivity
ϵ_0	Vacuum permittivity
ϵ'	Real part of complex permittivity
ϵ''	Imaginary part of complex permittivity
ϵ_∞	Optical permittivity
ϵ_{r}	Relative permittivity
ϵ_{s}	Static permittivity

ζ	Index of the transmitting TRA element
$\kappa_{\zeta,\xi}$	The entry of $\boldsymbol{K}$ formed with the signal received by the ξ-th antenna when the ζ-th antenna probes the scene
λ_i	The i-th eigenvalue of the TRO
μ	Permeability
ν_m	Time shift in discrete time domain
ξ	Index of the receiving TRA element
ρ_q	The scattering coefficient of the q-th scatterer
σ_{s}	Static conductivity
τ_D	Debye dielectric relaxation time constant
ψ_{M0}	The analysing (*mother*) wavelet in time domain. In our work this is the complex Morlet function.
$\hat{\psi}_{\mathrm{M0}}$	The analysing (*mother*) wavelet in the frequency domain.
ω_{M}	Central angular frequency of the analysing (*mother*) wavelet (dimensionless and equal to $2\pi f_{\mathrm{M}}$)
ω_k	The k-th harmonic of the fundamental frequency of the DFT
a_0	The smallest resolvable DTWT scale factor
a_j	The j-th DTWT scale factor
c	Speed of light in propagation medium
f	Frequency (in Hz)
f_{c}	Centre frequency of the excitation pulse
f_{M}	Centre frequency of the analysing (*mother*) wavelet (dimensionless and equal to $\omega_{\mathrm{M}}/2\pi$)
$f_{\max}$	Maximum frequency of interest of the excitation pulse
$f_{\min}$	Minimum frequency of interest of the excitation pulse
$\boldsymbol{g}$	Steering vector
$\mathbf{i}$	Unit vector in the direction of the x axis

$\jmath$	The imaginary unit, i.e. a solution to the quadratic $x^2 + 1 = 0$
j	Index used with discrete scale factors for the DTWT
$\mathbf{j}$	Unit vector in the direction of the y axis
k	Discrete frequency bin
$\mathbf{k}$	Unit vector in the direction of the z axis
k_c	Discrete frequency bin corresponding to the centre frequency f_c
l	Index for the l-th spatial window
m	Index for the m-th slided temporal window
n	The discrete time variable
q	Index for the q-th scatterer
$\boldsymbol{r}$	Position vector
s^2	Stabilisation parameter
v	Speed of wave propagation
x	(with a temporal argument, e.g. $x(t)$) Signal in the time domain
$\boldsymbol{x}$	discretised spatial location vector
z	Propagation distance

Abstract

TR-based techniques have recently been proposed for the microwave imaging of stationary and moving targets. Classical TR-based array processing methods perform poorly for imaging of non-pointlike targets. This thesis proposes a novel TR-MUltiple SIgnals Classification (MUSIC)-based algorithm for the Ultra WideBand (UWB) through-the-wall imaging of multiple extended moving targets. This algorithm performs spatiotemporal windowing on the received signals, to exploit their temporal and spatial diversity. Then, it applies a novel process to identify the signal subspace of each window. Finally, it produces the final radar image by selecting the strongest results obtained by different temporal and spatial windows and frequencies. This thesis applies the proposed algorithm to a simulated practical scenario and achieves the detection of five overlapping human-like targets moving behind a brick wall, whereas the state-of-the-art windowed UWB-MUSIC method detects only two targets.

Dispersive media cause frequency-dependent additional attenuation onto electromagnetic waves propagating through them. Consequently, the resolution of the TR imaging is degraded in such media. This thesis also introduces a new algorithm for the resolution enhancement of UWB TR radar imaging in dispersive environments. This algorithm takes into account the frequency-dependent complex permittivity of the propagation medium across the entire bandwidth of the excitation pulse. Using this complex permittivity, it constructs a Continuous Wavelet Transform (CWT)-based model of the attenuation, to create inverse filters in the wavelet domain, which compensate for the effects of the attenuation. This algorithm also introduces a smart wavelet scaling concept to minimise undesired noise amplification. This thesis applies this proposed algorithm to a practical scenario and enhances the resolution of UWB microwave TR imaging of a simulated brain tumour inside the Digital Human Phantom (DHP), whilst the existing work fails to detect the tumour.

Declaration

No portion of the work referred to in this thesis has been submitted in support of an application for another degree or qualification of this or any other university or other institute of learning.

Copyright

Acknowledgements

This work was supported by the Engineering and Physical Sciences Research Council (EPSRC), U.K. [project reference 1830967].

I owe my supervisor Dr Fumie Costen deep gratitude for her precious and continuous support of my academic efforts. Thank you for all the encouragement, the helpful advice, and the exciting discussions.

Thanks to Dr Mehmet E. Yavuz for his constructive comments on my work.

Thanks to the RIKEN research institute in Saitama, Japan, for providing the Digital Human Phantom and High Performance Computing resources.

I would like to thank my fellow PhD colleagues at The University of Manchester and especially in the Control, Communications and Signal Processing (CCSP) division of the Department of Electrical and Electronic Engineering (formerly, the Information Engineering division and the Microwave and Communication Systems group). Thank you for the good times and the memorable moments we shared.

I would like to warmly thank prof. Vaios Lappas for so generously being available to provide thoughtful comments on my work and for his encouragement.

Last but certainly not least, I would like to heartily thank Dr Savvas Papasavvas FRCEM for all his invaluable support and help during my studies in the U.K., to whom I am most grateful.

Rhodes, Greece — Loukas Xanthos
25 March 2021

To my parents Amalia and Pavlos
and to my brother Nikolaos Georgios.

Chapter 1

Introduction

1.1 Motivation

In recent years, the Time Reversal (TR) method has found several applications, such as acoustics for brain therapy, non-destructive testing, under-water telecommunications, fault diagnosis in wire networks [2]. For electromagnetic TR imaging applications, higher frequencies (smaller wavelengths) can achieve a finer spatial resolution. However, electromagnetic waves generally penetrate matter more effectively at lower frequencies of the electromagnetic spectrum. Hence Ultra Wide-Band (UWB) techniques are widely popular for imaging applications. Wideband and UWB TR techniques have been applied in electromagnetic radar imaging including Ground Penetrating Radar (GPR) [3–5], in communications [6–8] and in biomedical applications [9–11]. UWB microwave imaging utilising TR aimed for microwave breast cancer detection has been studied in [9, 12–14] and references therein.

TR-based radar imaging techniques suffer deterioration of the spatial resolution in cases of wave propagation through lossy media [15, 16]. Compensation methods can tackle this deterioration to improve the refocusing resolution under such conditions. Dispersive media, such as the human body, exhibit attenuation which is dependent on both time and frequency. Hence, TR applications which involve highly dispersive media, such as the radar imaging of the human body, can benefit from approaches that compensate for the effects of medium dispersion, and enhance the imaging resolution. The recent work in [1] presents a computationally efficient approach for the compensation of the effects of medium dispersion on TR imaging which is based on the Continuous Wavelet Transform

(CWT) of the received signals. However, we have identified a few details of the work in [1] which may cause it to be unreliable in UWB imaging settings.

Through-the-Wall Radar Imaging (TWRI) [17] has recently been a subject of scientific interest and of increasing importance, due to a broad range of applications, such as civilian and military applications, surveillance, search-and-rescue, and anti-terrorism [17–24]. A fundamental aspect of any TWRI system is the imaging algorithms, as they affect the overall effectiveness of the system [20, 24–26]. It is considered crucial for urban TWRI systems to be able to detect people walking behind walls [27]. Conventional approaches in high-resolution array processing techniques typically assume point-like targets [28]. In general, TR-based methods are considered to be robust and able to locate multiple targets [4]. However, scenarios which contain multiple extended targets break the well-resolvedness criterion that the algorithms which are based on the classical TR techniques rely on. Radar interrogation of such scenarios gives rise to effects such as target shadowing and multipath propagation phenomena. Hence, targets remain undetected or the corresponding radar images are cluttered and the sensing of true targets is impaired in such scenarios. Recently, [4] provided a TR-MUSIC based method to achieve the UWB radar imaging of multiple extended stationary targets, by means of segregation of the received radar signals in temporal and spatial windows. The segregation of the received radar signals leads to promising results for the radar imaging of multiple stationary targets. In [29], the application of spatial – but not temporal – windows together with the UWB-MUltiple SIgnals Classification (MUSIC) method was examined for the radar imaging of multiple extended expanding targets in inhomogeneous environments. The results achieved by [29] for the case of TWRI of multiple expanding targets are promising for the further development of TR-based methods for the TWRI of multiple extended and human-like moving targets.

1.2 Aims and Objectives

1.2.1 Aims

The purpose of this research is to contribute novel algorithms for the microwave imaging of stationary and moving targets hidden behind unknown optical obstructions. Specifically, this thesis aims

- to introduce a TR-MUSIC-based technique for the UWB radar imaging of multiple extended moving targets which are hidden behind a wall; and
- to propose a method for the resolution enhancement of UWB TR radar imaging of stationary targets in dispersive environments.

1.2.2 Objectives

The objectives of this thesis are:

- Combine the spatial and temporal windowing techniques on differential Multistatic Data Matrix (MDM) data
- Introduce and implement the novel Frequency-selective MUSIC (FQ-MUSIC) imaging functional
- Investigate the performance of different techniques for the setting of the dimension of the signal subspace of the differential MDM
- Introduce and implement the new Window- and Frequency- selective MUSIC (WF-MUSIC) imaging functional
- Develop simulation scenarios to assess the merit of the spatiotemporal windowing of the differential MDM with the WF-MUSIC imaging functional
- Implement the Ultra WideBand MUSIC (UWB-MUSIC) imaging functional with spatiotemporal windowing for differential MDM data
- Apply the novel WF-MUSIC imaging functional for the detection of multiple extended moving targets behind a wall
- Implement the CWT-based dispersion compensation method in [1]
- Develop a novel compensation method, based on the CWT of the received signals and the stabilised inverse filtering technique of [1], that makes use of the complex permittivity of the propagation medium across the whole spectrum of source excitation (rather than the centre frequency)
- Apply the new compensation method to a TR imaging scenario containing a dispersive and homogeneous propagation medium and to a practical scenario containing an inhomogeneous and dispersive background.

1.3 Research contributions

This thesis introduces two radar signal processing methods. One achieves the through-the-wall radar imaging of multiple extended moving targets. This method includes the following original work:

- We perform spatiotemporal windowing on a differential MDM, for the radar imaging of multiple extended moving targets. This is the first time that both spatial *and temporal* windowing on a differential MDM is applied to detect moving targets, to the best of the author's knowledge.

- We propose a process to determine the signal subspace of the sub-differential MDMs.

- We introduce the FQ-MUSIC imaging functional to extract radar images of moving targets from one sub-differential MDM using an UWB interrogation signal.

- We introduce the WF-MUSIC imaging functional to to combine the target information from each sub-differential MDM and form a final radar image for the through-the-wall radar imaging of multiple extended moving targets.

- We apply our proposed imaging method on a through-the-wall UWB radar scenario containing five overlapping human-like targets moving behind a brick wall. Our work detects all five targets, while the state-of-the-art method in [4] detects only two targets.

This thesis also proposes a CWT-based algorithm for the enhancement of the refocusing resolution of UWB TR radar imaging, when applied with lossy and dispersive media such as the human body. The summary of original contributions from this part of our work is:

- Our algorithm incorporates the frequency-dependent complex permittivity of the propagation medium across the *whole* spectrum of interest, for the first time to our knowledge, in the wavelet scale-dependent model of the attenuation, unlike the already existing work in the literature.

- This work introduces algorithm-driven automatic obviation of the noise amplification depending on the spectrum of the interrogating UWB pulse,

contrary to the empirical approaches in relevant prior work, to the best of the author's knowledge.

- This work integrates the minimum entropy criterion to dispersion compensation problems for the first time to the author's knowledge, to objectively determine the time of TR refocusing.

- We apply our algorithm on a scenario involving a brain tumour inside the head of a Digital Human Phantom (DHP) in UWB sensing settings. Our work located the tumour with 1.3 times better resolution than the conventional TR approach along the cross-range direction, and 1.56 times better resolution along the range direction, while the relevant prior work failed to locate the tumour.

- The original contributions in this algorithm correct and improve the method proposed in [1]. In this thesis, we show theoretically and numerically that the prior work [1] performs incorrect calculations when used with UWB signals.

Also, the following journal paper has been published:

L. Xanthos, M. E. Yavuz, R. Himeno, H. Yokota and F. Costen, "Resolution Enhancement of UWB Time-Reversal Microwave Imaging in Dispersive Environments," in *IEEE Transactions on Computational Imaging*, vol. 7, pp. 925-934, 2021, doi: 10.1109/TCI.2021.3104750.

1.4 Outline of this thesis

The rest of this thesis is organised as follows:

- Chapter 2 discusses TR techniques. It starts by studying the conventional TR method. Then, it presents the TR-MUSIC, and UWB-MUSIC subspace methods for radar imaging. Furthermore, it summarises prior approaches on extended targets imaging using TR-based techniques. Moreover, Chapter 2 discusses the effects lossy and dispersive media have on the TR imaging and reviews the existing approaches on the resolution enhancement of TR imaging in dispersive environments.

- Chapter 3 introduces two novel radar signal processing algorithms. Specifically, Chapter 3 proposes an algorithm for the TWRI of multiple extended moving targets under UWB sensing settings. In addition, Chapter 3 proposes an algorithm for the resolution enhancement of UWB electromagnetic TR imaging of stationary targets in stationary, linear and dispersive propagation media by inverse filtering the attenuation caused by the media.

- Chapter 4 prepares the simulation experiments which allow us to investigate the performance of the algorithms we propose in Chapter 3 and compare it against existing work. For our proposed approach regarding the TWRI of multiple extended moving targets, we set up two canonical case experiments and one practical case experiment involving five extended targets moving behind a brick wall. For our proposed approach for the resolution enhancement of UWB electromagnetic TR imaging of stationary targets, we prepare one canonical case experiment and one practical case experiment using the head of a DHP. The electromagnetic fields for the simulation experiments we conduct are computed using the Frequency-Dependent Finite Difference Time Domain ($(FD)^2TD$) [30] method with the Complex Frequency-Shifted Perfectly Matched Layer (CFS-PML) [31] absorbing boundary conditions.

- Chapter 5 performs each experiment detailed in Chapter 4. It presents, examines and discusses the results obtained from each experiment.

- Finally, Chapter 6 draws concluding summaries and suggests future work based upon our research.

1.5 Summary

In this chapter, the thesis objectives, aims, and a summary of the achievements were presented. Also, an outline of the rest of this thesis was provided.

Chapter 2

Background

This chapter discusses the details of TR techniques starting from the conventional TR method. Then, it presents TR-based imaging methods such as the TR-MUSIC, and UWB-MUSIC methods. Next, it reviews existing approaches on TR-based imaging of extended targets. It follows with a discussion on the negative effects lossy and dispersive media have on TR imaging. It then reviews prior approaches to dispersion compensation for TR imaging.

2.1 The TR method for electromagnetic waves

The TR method allows the determination of the location of one or several wave sources from their radiated or scattered field. This can be achieved in lossless and stationary media by solving the wave equation backwards in time, using the known radiated or scattered field as the initial condition. The TR method was pioneered by M. Fink *et al.* [32] in the context of acoustic fields and was later [33–36] extended in electromagnetic studies. A review of the history of the usage of the term *TR* in electromagnetics is found in [37].

Let us consider the following vector wave equation for non-dissipative isotropic media in a source-free region

$$\left(\nabla^2 - \frac{1}{\upsilon^2(\boldsymbol{r})}\frac{\partial^2}{\partial t^2}\right)\boldsymbol{F}(\boldsymbol{r},t) = 0 \tag{2.1}$$

where $\boldsymbol{F}$ is a vector field, υ is the speed of wave propagation, ∇^2 is the vector Laplace operator, $\boldsymbol{r} = x\mathbf{i} + y\mathbf{j} + z\mathbf{k}$ is the spatial position vector, and $\mathbf{i}$, $\mathbf{j}$, $\mathbf{k}$ are unit vectors in the x, y, z directions respectively of the 3D Cartesian coordinate

system. In the context of electromagnetics, we can substitute $\boldsymbol{F}$ in (2.1) with the electric field $\boldsymbol{E}$ or the magnetic flux density field $\boldsymbol{B}$ and then υ becomes the speed of light $\upsilon(\boldsymbol{r}) = c(\boldsymbol{r}) = \dfrac{1}{\sqrt{\mu(\boldsymbol{r})\varepsilon(\boldsymbol{r})}}$, where μ is the medium permeability and ε is the permittivity.

Let $\boldsymbol{C}(\boldsymbol{r}, t)$ be a solution to (2.1) and $\tau \triangleq -t$. For the first and second order temporal derivatives of the time-reversed solution, $\boldsymbol{C}(\boldsymbol{r}, -t) \equiv \boldsymbol{C}(\boldsymbol{r}, \tau)$, it holds

$$\frac{\partial}{\partial t}\boldsymbol{C}(\boldsymbol{r}, \tau) = \frac{\partial}{\partial \tau}\frac{\partial \tau}{\partial t}\boldsymbol{C}(\boldsymbol{r}, \tau) = -\frac{\partial}{\partial \tau}\boldsymbol{C}(\boldsymbol{r}, \tau) \tag{2.2a}$$

$$\begin{aligned}\frac{\partial^2}{\partial t^2}\boldsymbol{C}(\boldsymbol{r}, \tau) &= \frac{\partial}{\partial t}\left(-\frac{\partial}{\partial \tau}\boldsymbol{C}(\boldsymbol{r}, \tau)\right) \\ &= \frac{\partial}{\partial \tau}\frac{\partial \tau}{\partial t}\left(-\frac{\partial}{\partial \tau}\boldsymbol{C}(\boldsymbol{r}, \tau)\right) = \frac{\partial^2}{\partial \tau^2}\boldsymbol{C}(\boldsymbol{r}, \tau).\end{aligned} \tag{2.2b}$$

Thus, substituting $\boldsymbol{F}(\boldsymbol{r}, t)$ with $\boldsymbol{C}(\boldsymbol{r}, \tau)$ into (2.1) and making use of (2.2b) yields

$$\left(\nabla^2 - \frac{1}{\upsilon^2(\boldsymbol{r})}\frac{\partial^2}{\partial \tau^2}\right)\boldsymbol{C}(\boldsymbol{r}, \tau) = 0 \tag{2.3}$$

which is of identical form to (2.1). Therefore, if $\boldsymbol{C}(\boldsymbol{r}, t)$ is a solution to (2.1), then $\boldsymbol{C}(\boldsymbol{r}, -t)$ is also a solution to (2.1). It can be shown in a similar manner that, for any constant time shift T_{shift}, $\boldsymbol{C}(\boldsymbol{r}, T_{\text{shift}} - t)$ is also a solution to (2.1). Hence, the lossless wave equation is invariant under a time-reversal operation. As a consequence, for every wave propagating away from a source (passive or active), there exists a time-reversed wave which can retrace the path of the original wave back to the source [38]. Propagation media which are lossless, or exhibit negligible dissipation of energy and therefore allow for the time-reversal symmetry of the wave equation are called *reciprocal* [39]. The non-dissipative nature of such media is also termed as *reciprocity* or the *reciprocal property* [39].

With the conventional TR method, field signals in reciprocal media are sensed by a set of sensors and are simultaneously recorded on a memory system for a specified duration. This stage of the TR process is termed the *forward propagation*. Conventionally, the sensors are transducers in acoustics applications. Electromagnetic applications conventionally use antennas as the sensors [35] [40]. Next, the recorded field signals are physically or synthetically retransmitted in a time-reversed fashion. This stage of the TR process is termed the *backpropagation*. In this way, causal and physically realisable systems are constructed for

conventional TR applications. Such systems exploit the time-reversal symmetry of the wave equation to focus energy around the location(s) of signal source(s). Synthetic backpropagation is used in conventional TR *imaging*, to form images of sources or scatterers computationally and extract information on their location [40, 41]. Specifically, in synthetic TR for imaging applications, the computational backpropagation is performed in a simulated scenario which contains the exact or approximate background of the scene of interest but not the targets. For the sources, *active* sources can be considered, i.e. the sources that actively provide energy to the propagation scenario, or *passive* ones, e.g. scatterers in a propagation scenario where one or more active sources have initially provided energy.

In the ideal TR situation, wave fields propagating in all possible directions should be considered, so that the whole original wave could be generated [38]. However, in practical electromagnetic scenarios it is often impossible to completely surround the source and record all the wave fields diverging from it [38]. For this reason, the TR method in electromagnetic applications is generally performed with a set of transmit-receive antennas. This set of antennas is called the Time Reversal Array (TRA) [15]. Although the term *array* is commonly used in TR literature, the TRA antennas should ideally be independent transceivers [40]. A TRA with a limited aperture causes "information loss" relative to the ideal situation [40] [42, Section 4.6.2]. In general, the size of the spot of refocusing increases as the TRA aperture size decreases [40]. The amount of lost information can be reduced through the utilisation of propagation multipaths [40]. Propagation multipaths increase the effective TRA aperture and the refocusing precision.

Let a TRA be placed in an infinite reciprocal medium and a point source be placed at $\boldsymbol{r}_q$ in the same medium. Let this point source transmit a short UWB pulse $S(t)$. The signal which the ξ-th antenna receives can be expressed as

$$F_\xi(t) = S(t) * h_{\boldsymbol{r}_q \boldsymbol{r}_\xi}(t) \tag{2.4}$$

where $*$ is the convolution in time, $h_{\boldsymbol{r}_q \boldsymbol{r}_\xi}$ is the impulse response between the point source located at $\boldsymbol{r}_q$ and the ξ-th TRA antenna located at $\boldsymbol{r}_\xi$. Assuming medium reciprocity, it holds $h_{q \leftrightarrow \xi}(t) \triangleq h_{\boldsymbol{r}_q \boldsymbol{r}_\xi}(t) = h_{\boldsymbol{r}_\xi \boldsymbol{r}_q}(t)$ [40, 41, 43]. Let $F_\xi(t)$ be recorded, reversed in time and transmitted back to the propagation medium by the ξ-th antenna. This backpropagated signal observed at $\boldsymbol{r}_q$ due to antenna

ξ is

$$F_q(t) = \underbrace{S(-t) * h_{\boldsymbol{r}_q\boldsymbol{r}_\xi}(-t)}_{F_\xi(-t)} * h_{\boldsymbol{r}_\xi\boldsymbol{r}_q}(t). \tag{2.5}$$

In (2.5), the convolution $h_{\boldsymbol{r}_q\boldsymbol{r}_\xi}(-t) * h_{\boldsymbol{r}_\xi\boldsymbol{r}_q}(t)$ can be thought as an autocorrelation in time of the reciprocal medium's impulse response. Indeed, it is

$$h_{\boldsymbol{r}_q\boldsymbol{r}_\xi}(-t) * h_{\boldsymbol{r}_\xi\boldsymbol{r}_q}(t) = h_{q\leftrightarrow\xi}(t) \star h_{q\leftrightarrow\xi}(t) \tag{2.6}$$

where $\star$ denotes the correlation operation. The autocorrelation in (2.6) has a global maximum at $t = 0$. The value of this maximum is the energy of $h_{q\leftrightarrow\xi}(t)$, that is

$$\max\big(h_{q\leftrightarrow\xi}(t) \star h_{q\leftrightarrow\xi}(t)\big) = h_{q\leftrightarrow\xi}(0) \star h_{q\leftrightarrow\xi}(0) = \int_{-\infty}^{\infty} |h_{q\leftrightarrow\xi}(t)|^2 \, \mathrm{d}t. \tag{2.7}$$

(2.7) shows that the TR process achieves optimal refocusing in time in reciprocal media.

TR systems exhibit better refocusing performance with multiple TRA antennas rather than with few antennas. This is because each antenna's retransmission produces a maximum signal energy at the original source location and the signals from all the TRA elements interfere constructively. Therefore, the TR refocusing signal is stronger at the original source location. That is, if $F_{\boldsymbol{r}_q}(t)$ is the signal observed at $\boldsymbol{r}_q$ due to the backpropagation from all the TRA antennas, and the TRA consists of $\mathcal{N}$ transceivers, then,

$$F_{\boldsymbol{r}_q}(t) = \sum_{\xi=1}^{\mathcal{N}} \underbrace{S(-t) * h_{\boldsymbol{r}_q\boldsymbol{r}_\xi}(-t)}_{F_\xi(-t)} * h_{\boldsymbol{r}_\xi\boldsymbol{r}_q}(t). \tag{2.8}$$

The backpropagated signals converge and focus coherently at the original source location [40]. If we place an ideal receiving element at any point $\boldsymbol{r}'$ in the domain with $\boldsymbol{r}' \neq \boldsymbol{r}_q$, the signal this receiver observes is

$$F_{\boldsymbol{r}'}(t) = \sum_{\xi=1}^{\mathcal{N}} S(-t) * h_{\boldsymbol{r}_q\boldsymbol{r}_\xi}(-t) * h_{\boldsymbol{r}_\xi\boldsymbol{r}'}(t). \tag{2.9}$$

In (2.9), we have that $h_{\boldsymbol{r}_q\boldsymbol{r}_\xi}(-t) * h_{\boldsymbol{r}_\xi\boldsymbol{r}'}(t) = h_{\boldsymbol{r}_q\boldsymbol{r}_\xi}(t) \star h_{\boldsymbol{r}_\xi\boldsymbol{r}'}(t)$. Hence, the magnitude of $F_{\boldsymbol{r}'}(t)$ decreases as the distance between $\boldsymbol{r}'$ and $\boldsymbol{r}_q$ increases, due to the

uncorrelated $h_{\boldsymbol{r}_q \boldsymbol{r}_\xi}(t)$ and $h_{\boldsymbol{r}_\xi \boldsymbol{r}'}(t)$ in (2.9) [40]. Hence, the TR method functions as a correlator in both space and time [44] given that the propagation media are reciprocal. Also, (2.8) shows that the TR method can achieve refocusing even in the case where a limited number of antennas is used (as it is often the case with TR experiments), instead of entirely surrounding the point source target. In propagation media with rich multipath components, the correlation peak in (2.8) becomes sharper relative to the case without rich multipath components and a more precise focusing spot both in space and time can be achieved with the TR method [40].

The TR method has found several applications in recent years, such as acoustics for brain therapy, non-destructive testing, under-water telecommunications, fault diagnosis in wire networks [2]. In electromagnetics, the TR techniques have been applied in radar imaging including GPR [3–5], in communications [6–8] and in biomedical applications [9–11].

2.2 Subspace methods and selective focusing

Subspace techniques based on the TR method can achieve imaging without the need for physical or simulated backpropagation. In this section, we review details of the TR-based subspace techniques TR-Décomposition de l'Opérateur de Retournement Temporel – English: Decomposition of the TR Operator (DORT) [43], TR-MUSIC [41], and UWB-MUSIC [45]. For simplicity, we shall refer to both TR-MUSIC and UWB-MUSIC methods collectively as *MUSIC methods*, wherever appropriate in this section.

The TR-DORT and TR-MUSIC methods achieve imaging using a single frequency of interest of the TRA interrogation signal. The UWB-MUSIC method is practically performed over a wide bandwidth of interest, which usually is the bandwidth of a UWB radar interrogation pulse. TR-DORT and MUSIC methods assume a TRA consisting of ideal point (monopole) elements to perform TR experiments. In practice, real antennas can be used [9, 46, 47]. Each TRA element is used, one at a time, to illuminate the scene of interest. In particular, one TRA element transmits an excitation pulse at a time, and all the TRA elements observe the received signals simultaneously. All the TRA antennas operate as signal receivers at the same time that one receiving TRA antenna also transmits an interrogation signal, hence forming a Multiple-Input Single-Output (MISO)

system. The observed signals are recorded in a matrix termed the MDM. Specifically, every one matrix element of the MDM contains the received signal for a corresponding pair of transmitting and receiving TRA antennas.

By successive TR experiments, using the backpropagated signals of one TR experiment as the forward propagating signals for the next TR experiment, focusing on the most reflective scatterer can be achieved [48]. This process is known as the iterative TR method [48]. The iterative TR process at one frequency can be described by a matrix called the Time Reversal Operator (TRO) [48]. The TRO can be formed by manipulating the MDM and it can be diagonalised. [48] shows that the eigenvectors of the TRO are eigenmodes of the iterative TR process. Also, for the case where multiple scatterers exist in the scene under radar interrogation, selective focusing and selective nulling can be achieved by utilising the eigenvectors of the TRO [40].

The basis for both the TR-DORT and MUSIC methods is the decomposition of the TRO [48]. The eigendecomposition of the TRO requires prior computation for the formation of the TRO matrix. The Singular Value Decomposition (SVD) of the MDM can be used to obtain the eigensystem of the TRO without requiring the formation of the TRO matrix. Using the SVD of the MDM, the signal and null subspaces of the MDM are identified. The TR-DORT method uses the signal subspace of the MDM to achieve synthetic focusing. The MUSIC methods work on the null subspace of the MDM to achieve radar imaging.

TR-based subspace techniques do not require knowledge of the location of the targets, but they do require knowledge of the background Green function. Moreover, the MUSIC methods require that the MDM has a non-trivial null subspace. The TR-based subspace methods we analyse in this section assume ideal pointlike TRA transmit/receive elements, but they can also be applied with finite aperture reciprocal antenna elements [41, 49].

2.2.1 The TR-DORT method

We consider a TRA consisting of $\mathcal{N}$ ideal point antenna elements. Specifically, each antenna ζ, $1 \leq \zeta \leq \mathcal{N}$ is used to transmit a signal, to probe the scene of interest for a TR experiment to be performed. Each antenna ξ, $1 \leq \xi \leq \mathcal{N}$ is used for signal sensing.

The MDM $\boldsymbol{K}$ is defined as

$$\boldsymbol{K}(t) = \begin{pmatrix} \kappa_{1,1}(t) & \dots & \kappa_{1,\mathcal{N}}(t) \\ \vdots & \ddots & \vdots \\ \kappa_{\mathcal{N},1}(t) & \dots & \kappa_{\mathcal{N},\mathcal{N}}(t) \end{pmatrix}. \tag{2.10}$$

We express $\boldsymbol{K}(t)$ in the frequency domain as in

$$\boldsymbol{K}(\omega) = \begin{pmatrix} \kappa_{1,1}(\omega) & \dots & \kappa_{1,\mathcal{N}}(\omega) \\ \vdots & \ddots & \vdots \\ \kappa_{\mathcal{N},1}(\omega) & \dots & \kappa_{\mathcal{N},\mathcal{N}}(\omega) \end{pmatrix}. \tag{2.11}$$

For Q point-like scatterers which are well-resolved by the TRA, we can express $\kappa_{\zeta,\xi}(\omega)$ employing the distorted wave Born approximation [41] as

$$\kappa_{\zeta,\xi}(\omega) = \sum_{q=1}^{Q} S(t) G(\boldsymbol{r}_\zeta, \boldsymbol{r}_q, \omega) G(\boldsymbol{r}_q, \boldsymbol{r}_\xi, \omega) \rho_q \tag{2.12}$$

where q is the index for the q-th scatterer, ρ_q is the scattering coefficient of the q-th scatterer, and $G(\boldsymbol{r}_\zeta, \boldsymbol{r}_q, \omega)$ is the Green function of the reciprocal medium between the ζ-th TRA element and the q-th scatterer. The multiple scattering between the scatterers is negligible and is therefore ignored in (2.12), due to our prior assumption that the well-resolvedness criterion holds [15]. To express the MDM in a more compact form, we employ the background Green function vector, $\boldsymbol{g}$, also termed the *steering vector*, with

$$\boldsymbol{g}(\boldsymbol{r}_q, \omega) = \Big[G(\boldsymbol{r}_{\xi=1}, \boldsymbol{r}_q, \omega), \dots, G(\boldsymbol{r}_{\xi=\mathcal{N}}, \boldsymbol{r}_q, \omega) \Big]^{\mathrm{T}} \tag{2.13}$$

where $^{\mathrm{T}}$ is the transpose operation. $\boldsymbol{g}(\boldsymbol{r}_q, \omega)$ relates the q-th scatterer's location $\boldsymbol{r}_q$ to the TRA elements. In case of inhomogeneous media, approximate steering vectors can be used [41, 45]. $G(\boldsymbol{r}_\xi, \boldsymbol{r}_q, \omega)$ can be substituted by the actual field radiated by the TRA elements in a scenario containing the background medium but not the targets [29, 41]. In this case, $\boldsymbol{g}(\boldsymbol{r}_q, \omega)$ becomes an "antenna vector" whose components are the actual radiated fields in a scenario with the (actual or approximate) background medium and without the targets [29, 41]. Using (2.13),

we can write (2.12) as

$$\boldsymbol{K}(\omega) = S(\omega) \sum_{q=1}^{Q} \rho_q \, \boldsymbol{g}(\boldsymbol{r}_q, \omega) \, \boldsymbol{g}^{\mathrm{T}}(\boldsymbol{r}_q, \omega). \tag{2.14}$$

We note here that our initial assumption that we have Q *well-resolved* scatterers means $Q \leq \mathcal{N}$ and also that the problem's steering vectors are approximately orthogonal [41], i.e.

$$\langle \boldsymbol{g}(\boldsymbol{r}_q, \omega), \boldsymbol{g}(\boldsymbol{r}_{q'}, \omega) \rangle \approx \begin{cases} \|\boldsymbol{g}(\boldsymbol{r}_q, \omega)\|^2 & \text{if } \boldsymbol{r}_q \equiv \boldsymbol{r}_{q'} \\ 0 & \text{otherwise} \end{cases} \tag{2.15}$$

where $\boldsymbol{r}_{q'}$ is a position vector. $\langle \, , \rangle$ is a standard inner product, i.e., for vector arguments $\boldsymbol{a}$ and $\boldsymbol{b}$, $\langle \boldsymbol{a}, \boldsymbol{b} \rangle = \boldsymbol{b}^{\mathrm{H}} \boldsymbol{a}$. $\|\boldsymbol{g}(\boldsymbol{r}_q, \omega)\|$ denotes the norm of $\boldsymbol{g}(\boldsymbol{r}_q, \omega)$, that is

$$\|\boldsymbol{g}(\boldsymbol{r}_q, \omega)\| = \sqrt{\langle \boldsymbol{g}(\boldsymbol{r}_q, \omega), \boldsymbol{g}(\boldsymbol{r}_q, \omega) \rangle}. \tag{2.16}$$

The TRO [15, 48] is defined as the Hermitian (self-adjoint) matrix

$$\boldsymbol{\mathcal{T}}(\omega) \triangleq \boldsymbol{K}^{\mathrm{H}}(\omega) \boldsymbol{K}(\omega) \tag{2.17}$$

where $^{\mathrm{H}}$ denotes the Hermitian adjoint (conjugate transpose). The motivation for defining the TRO emerges from the iterative TR method and is analysed in [48, Section 3.4]. We note here that $\boldsymbol{K}^{\mathrm{H}}(\omega)$ is in fact the Fourier transform of $\boldsymbol{K}(-t)$ [15]. This is because the time-reversal operation $t \to -t$ in time domain corresponds to phase conjugation in frequency domain.

We perform the SVD of the MDM as in

$$\boldsymbol{K}(\omega) = \boldsymbol{U}(\omega) \boldsymbol{\Sigma}(\omega) \boldsymbol{V}^{\mathrm{H}}(\omega) \tag{2.18}$$

where $\boldsymbol{\Sigma}(\omega)$ is the real diagonal matrix containing the singular values in descending order, $\boldsymbol{U}(\omega)$ is a unitary matrix containing the left singular vectors, and $\boldsymbol{V}(\omega)$ is a unitary matrix containing the right singular vectors. These matrices can be

written as

$$\boldsymbol{\Sigma}(\omega) = \mathrm{diag}\{\sigma_1, \ldots, \sigma_{\mathcal{N}}\} = \begin{pmatrix} \sigma_1 & 0 & \cdots & \cdots & 0 \\ 0 & \ddots & \vdots & \vdots & \vdots \\ \vdots & \vdots & \ddots & \vdots & \vdots \\ \vdots & \vdots & \vdots & \ddots & 0 \\ 0 & \cdots & \cdots & 0 & \sigma_{\mathcal{N}} \end{pmatrix} \tag{2.19}$$

with

$$\sigma_1 \geq \sigma_2 \geq \cdots \geq \sigma_{\mathcal{N}} \geq 0, \tag{2.20}$$

$$\boldsymbol{U}(\omega) = \Big[\boldsymbol{u}_1(\omega), \ldots, \boldsymbol{u}_{\mathcal{N}}(\omega)\Big] = \begin{pmatrix} u_{1,1}(\omega) & \ldots & u_{1,\mathcal{N}}(\omega) \\ \vdots & \ddots & \vdots \\ u_{\mathcal{N},1}(\omega) & \ldots & u_{\mathcal{N},\mathcal{N}}(\omega) \end{pmatrix} \tag{2.21}$$

with $u_{\zeta,\xi}(\omega) \in \mathbb{C}$, and

$$\boldsymbol{V}(\omega) = \Big[\boldsymbol{v}_1(\omega), \ldots, \boldsymbol{v}_{\mathcal{N}}(\omega)\Big] = \begin{pmatrix} v_{1,1}(\omega) & \ldots & v_{1,\mathcal{N}}(\omega) \\ \vdots & \ddots & \vdots \\ v_{\mathcal{N},1}(\omega) & \ldots & v_{\mathcal{N},\mathcal{N}}(\omega) \end{pmatrix} \tag{2.22}$$

with $v_{\zeta,\xi}(\omega) \in \mathbb{C}$. We can thus see how the SVD of the MDM is related to the diagonalisation of the TRO:

$$\boldsymbol{\mathcal{T}}(\omega) = \big[\boldsymbol{V}(\omega)\boldsymbol{\Sigma}^{\mathrm{H}}(\omega)\boldsymbol{U}^{\mathrm{H}}(\omega)\big]\big[\boldsymbol{U}(\omega)\boldsymbol{\Sigma}(\omega)\boldsymbol{V}^{\mathrm{H}}(\omega)\big] \tag{2.23}$$

$$= \big[\boldsymbol{V}(\omega)\boldsymbol{\Sigma}(\omega)\boldsymbol{U}^{\mathrm{H}}(\omega)\big]\big[\boldsymbol{U}(\omega)\boldsymbol{\Sigma}(\omega)\boldsymbol{V}^{\mathrm{H}}(\omega)\big] \tag{2.24}$$

because $\boldsymbol{\Sigma}(\omega)$ is real and diagonal. Thus

$$\boldsymbol{\mathcal{T}}(\omega) = [\boldsymbol{V}(\omega)\boldsymbol{\Sigma}(\omega)]\big[\boldsymbol{U}^{\mathrm{H}}(\omega)\boldsymbol{U}(\omega)\big]\big[\boldsymbol{\Sigma}(\omega)\boldsymbol{V}^{\mathrm{H}}(\omega)\big]. \tag{2.25}$$

Since $\boldsymbol{U}(\omega)$ is unitary,

$$\boldsymbol{\mathcal{T}}(\omega) = [\boldsymbol{V}(\omega)\boldsymbol{\Sigma}(\omega)]\boldsymbol{I}\big[\boldsymbol{\Sigma}(\omega)\boldsymbol{V}^{\mathrm{H}}(\omega)\big] \tag{2.26}$$

$$= \boldsymbol{V}(\omega)\boldsymbol{\Sigma}^2(\omega)\boldsymbol{V}^{\mathrm{H}}(\omega) \tag{2.27}$$

$$= \boldsymbol{V}(\omega)\boldsymbol{\Lambda}(\omega)\boldsymbol{V}^{\mathrm{H}}(\omega) \tag{2.28}$$

where $\boldsymbol{I}$ is the identity matrix and $\boldsymbol{\Lambda}(\omega)$ is the real diagonal matrix containing

the eigenvalues $\lambda_i(\omega)$ of $\boldsymbol{\mathcal{T}}(\omega)$. Evidently, it holds

$$\lambda_i(\omega) = \sigma_i^2(\omega), \quad i \in \{1, 2, \ldots, \mathcal{N}\}. \tag{2.29}$$

Similarly, the eigenvectors of the TRO are the columns of $\boldsymbol{V}(\omega)$, i.e. $\boldsymbol{v}_i(\omega)$ with $i \in \{1, 2, \ldots, \mathcal{N}\}$, which are normalised and orthogonal [43, 48]. Therefore, it is possible to study the eigenstructure of the TRO by performing the SVD of the MDM [48].

By performing the SVD of the MDM, the following singular system is formed

$$\boldsymbol{K}(\omega)\boldsymbol{v}_i(\omega) = \sigma_i(\omega)\boldsymbol{u}_i(\omega) \tag{2.30}$$

$$\boldsymbol{K}^{\mathrm{H}}(\omega)\boldsymbol{u}_i(\omega) = \sigma_i^*(\omega)\boldsymbol{v}_i(\omega) \tag{2.31}$$

where * (in superscript) indicates complex conjugation. We substitute the expression for $\boldsymbol{K}(\omega)$ in (2.14) into (2.30) and obtain

$$S(\omega) \sum_{q=1}^{Q} \rho_q \, \boldsymbol{g}(\boldsymbol{r}_q, \omega) \, \boldsymbol{g}^{\mathrm{T}}(\boldsymbol{r}_q, \omega)\boldsymbol{v}_i(\omega) = \sigma_i(\omega)\boldsymbol{u}_i(\omega). \tag{2.32}$$

It holds

$$\boldsymbol{g}^{\mathrm{T}}(\boldsymbol{r}_q, \omega)\boldsymbol{v}_i(\omega) = \langle \boldsymbol{v}_i(\omega), \boldsymbol{g}^*(\boldsymbol{r}_q, \omega) \rangle. \tag{2.33}$$

Therefore, $\boldsymbol{g}^{\mathrm{T}}(\boldsymbol{r}_q, \omega)\boldsymbol{v}_i(\omega)$ is a scalar. Solving (2.32) for the left singular vector yields

$$\boldsymbol{u}_i(\omega) = \sum_{q=1}^{Q} \underbrace{\frac{S(\omega)\rho_q \langle \boldsymbol{v}_i(\omega), \boldsymbol{g}^*(\boldsymbol{r}_q, \omega) \rangle}{\sigma_i(\omega)}}_{\text{scalar factor}} \boldsymbol{g}(\boldsymbol{r}_q, \omega). \tag{2.34}$$

(2.34) shows that each left singular vector $\boldsymbol{u}_i(\omega)$ is a linear combination of all $\boldsymbol{g}(\boldsymbol{r}_q, \omega)$ (for all scatterers q). Similarly, by substituting the expression for $\boldsymbol{K}(\omega)$ in (2.14) into (2.31) we obtain

$$\boldsymbol{v}_i(\omega) = \sum_{q=1}^{Q} \underbrace{\frac{S^*(\omega)\rho_q \langle \boldsymbol{u}_i(\omega), \boldsymbol{g}(\boldsymbol{r}_q, \omega) \rangle}{\sigma_i^*(\omega)}}_{\text{scalar factor}} \boldsymbol{g}^*(\boldsymbol{r}_q, \omega). \tag{2.35}$$

Also, since $\boldsymbol{K}(\omega)$ is symmetric, it holds that

$$\boldsymbol{u}_i = \boldsymbol{v}_i^* \qquad \text{for } i = 1, 2, \ldots, \mathcal{N}. \tag{2.36}$$

(2.34) and (2.35) satisfy (2.36). Since $\boldsymbol{u}_i(\omega)$ is a linear combination of all the steering vectors, using (2.15) for the special case of well-resolved targets shows that $\langle \boldsymbol{u}_i(\omega), \boldsymbol{g}(\boldsymbol{r}_q, \omega)\rangle = 0$ for $\boldsymbol{u}_i(\omega) \neq A_0 \boldsymbol{g}(\boldsymbol{r}_q, \omega)$, where A_0 is a scalar. Similarly for the right singular vector, $\langle \boldsymbol{v}_i(\omega), \boldsymbol{g}^*(\boldsymbol{r}_q, \omega)\rangle = 0$ for $\boldsymbol{v}_i(\omega) \neq A_1 \boldsymbol{g}^*(\boldsymbol{r}_q, \omega)$, where A_1 is a scalar. Therefore, for the case where the well-resolvedness criterion holds, the following normalised linear combinations satisfy the singular system of (2.30) and (2.31) for the non-zero $\boldsymbol{u}_i(\omega)$ and $\boldsymbol{v}_i(\omega)$

$$\boldsymbol{u}_q(\omega) = \frac{\boldsymbol{g}(\boldsymbol{r}_q, \omega)}{\|\boldsymbol{g}(\boldsymbol{r}_q, \omega)\|} \tag{2.37}$$

$$\boldsymbol{v}_q(\omega) = \frac{\boldsymbol{g}^*(\boldsymbol{r}_q, \omega)}{\|\boldsymbol{g}(\boldsymbol{r}_q, \omega)\|} \tag{2.38}$$

for $q = 1, \ldots, Q$. Therefore, in the case where all targets are pointlike and well-resolved by the TRA, the singular system of (2.30) and (2.31) is associated to the targets in a one-to-one manner [41] in isotropic media. Moreover, in this case, the scatterer strengths are directly related to the singular values as in

$$\sigma_q(\omega) = S(t)\rho_q \|\boldsymbol{g}(\boldsymbol{r}_q, \omega)\|^2 \qquad \text{for } q = 1, \ldots, Q. \tag{2.39}$$

The vectors $\{\boldsymbol{u}_1(\omega),\ \ldots,\ \boldsymbol{u}_{\mathcal{N}^\Theta(\omega)}(\omega)\}$ whose corresponding singular values $\{\sigma_1(\omega),\ \ldots,\ \sigma_{\mathcal{N}^\Theta(\omega)}(\omega)\}$ are significant form the *signal subspace* of $\boldsymbol{K}$ [41, 45], where $\mathcal{N}^\Theta(\omega)$ is the dimension of the signal subspace of $\boldsymbol{K}(\omega)$. For the case of isotropic scattering from $Q < \mathcal{N}$ well-resolved pointlike scatterers, it is $\mathcal{N}^\Theta(\omega) = Q$ for all ω and $\sigma_1(\omega) \geq \cdots \geq \sigma_{\mathcal{N}^\Theta(\omega)}(\omega) > 0$. The vectors $\{\boldsymbol{u}_{\mathcal{N}^\Theta(\omega)+1}(\omega),\ \ldots,\ \boldsymbol{u}_{\mathcal{N}}(\omega)\}$ form the *null subspace* of $\boldsymbol{K}$. The signal and null subspaces of $\boldsymbol{K}$ are orthogonal subspaces. For the case of isotropic scattering from $Q < \mathcal{N}$ well-resolved pointlike scatterers in a noiseless environment, it holds for the null subspace of $\boldsymbol{K}$ that $\sigma_{\mathcal{N}^\Theta(\omega)+1}(\omega) = \cdots = \sigma_{\mathcal{N}}(\omega) = 0$ [50].

For the case of discrete scatterers, backpropagation of each $\boldsymbol{v}_q$ produces wavefront focusing on scatterer q [43], assuming isotropically scattered fields. Imaging of individual discrete scatterers using the signal subspace of $\boldsymbol{K}$ at a particular frequency can be performed with the TR-DORT imaging functional. The TR-DORT imaging functional at frequency ω_0 is given by [45]

$$\mathcal{M}^{\mathrm{DORT}}(i, \boldsymbol{r}, \omega_0) = \langle \boldsymbol{g}(\boldsymbol{r}, \omega_0), \boldsymbol{v}_i^*(\omega_0)\rangle \qquad \text{for } i = 1, \ldots, \mathcal{N}^\Theta(\omega_0) \tag{2.40}$$

which is also the point spread function of the TRA [41, 45].

2.2.2 The TR-MUSIC method

The TR-DORT method we studied in Section 2.2.1 achieves a one-to-one association of each singular vector in the signal subspace of $\boldsymbol{K}$ to each discrete well-resolved scatterer interrogated by the TRA, assuming isotropically scattered fields. In the case of electromagnetic TR practically no scatterer produces isotropically scattered electromagnetic fields in 3D, therefore, more than one eigenvalues of $\boldsymbol{K}$ can be associated to any single scatterer [38, 51]. Also, for the case of non-well resolved scatterers the one-to-one relation between each singular vector in the signal subspace of $\boldsymbol{K}$ and each discrete scatterer does not hold. Backpropagation of the signal subspace eigenvectors of $\boldsymbol{K}$ yields degraded refocusing performance (broader refocusing spots) relative to the well-resolved case, thus hindering target imaging and localisation [45]. Although the vectors $\boldsymbol{g}(\boldsymbol{r}_q, \omega)$ are not orthogonal in the case of non-well resolved (not well separated in space) scatterers, these vectors remain contained in the signal subspace of $\boldsymbol{K}$ [41]. Therefore, the vectors $\boldsymbol{g}(\boldsymbol{r}_q, \omega)$ are orthogonal to the null subspace of $\boldsymbol{K}$ even in the case of non-well resolved scatterers [41, 45], that is

$$\sum_{i=\mathcal{N}^{\Theta}(\omega)+1}^{\mathcal{N}} \langle \boldsymbol{g}(\boldsymbol{r}_q, \omega), \boldsymbol{v}_i^*(\omega) \rangle \approx 0 \tag{2.41}$$

and $\sigma_{\mathcal{N}^{\Theta}(\omega)+1}(\omega) \approx \sigma_{\mathcal{N}^{\Theta}(\omega)+2}(\omega) \approx \cdots \approx \sigma_{\mathcal{N}}(\omega) \approx 0$.

The conventional TR-MUSIC method utilises (2.41) by applying the *pseudospectrum*

$$\mathcal{M}^{\mathrm{TR}}(\boldsymbol{r}, \omega) = \frac{1}{\displaystyle\sum_{i=\mathcal{N}^{\Theta}(\omega)+1}^{\mathcal{N}} \Big| \langle \boldsymbol{g}(\boldsymbol{r}, \omega), \boldsymbol{v}_i^*(\omega) \rangle \Big|} \tag{2.42}$$

where $\mathcal{M}^{\mathrm{TR}}(\boldsymbol{r}, \omega)$ is the TR-MUSIC imaging functional. Ideally, the poles of $\mathcal{M}^{\mathrm{TR}}(\boldsymbol{r}, \omega)$ for a specific $\omega = \omega_0$ correspond to the locations of the scatterers. Hence, $\mathcal{M}^{\mathrm{TR}}(\boldsymbol{r}, \omega)$ ideally peaks at the locations of the scatterers and its value is close to zero away from the scatterers.

2.2.3 The UWB-MUSIC method

The TR-MUSIC method is not statistically stable. This means that inaccuracies in $\boldsymbol{g}(\boldsymbol{r},\omega)$ may have a significant effect on $\mathcal{M}^{\mathrm{TR}}(\boldsymbol{r},\omega)$ such as the appearance of artefacts (spurious peaks) in the final radar image [45, 52]. The UWB-MUSIC method combines the information from all frequencies in the bandwidth of interest Ω to produce a statistically stable radar imaging functional with the disadvantage of exhibiting poorer imaging precision [45]. The UWB-MUSIC imaging functional is given by

$$\mathcal{M}^{\mathrm{UWB}}(\boldsymbol{r}) = \frac{1}{\displaystyle\int_{\Omega} \sum_{i=\mathcal{N}^{\Theta}(\omega)+1}^{\mathcal{N}} \left| \langle \boldsymbol{g}(\boldsymbol{r},\omega), \boldsymbol{v}_i^*(\omega) \rangle \right| \mathrm{d}\omega} \tag{2.43}$$

and it is also a pseudospectrum. As with $\mathcal{M}^{\mathrm{TR}}(\boldsymbol{r},\omega)$, $\mathcal{M}^{\mathrm{UWB}}(\boldsymbol{r})$ ideally has maxima at the locations of the scatterers and minima at locations away from the scatterers.

2.3 Through-the-wall radar imaging of extended targets

The authors in [27] propose a method for the TWRI of human targets, based on the solution of linear integral equations derived from Physical Optics. [27] assumes that the electrical and geometrical properties of the front-wall are either known or accurately estimated and models the human targets as perfectly conducting cylinders. [27] applies time-gating onto the received radar responses to filter-out the direct coupling signals and the front-wall echoes.

TR-based methods can localise targets of interest with high resolution. Because of this, TR-based methods have been considered to be suitable for TWRI applications [53]. The differential TR technique [54, 55] is capable of locating and tracking moving targets in the presence of stationary targets. As with the conventional TR technique for the imaging of still targets, the differential TR technique also assumes that the moving targets are all *well-resolved*.

The authors in [52] developed a theory of TR-MUSIC-based imaging of extended targets which applies in both acoustics and electromagnetics. [52] demonstrates that imaging of extended targets using the TR-MUSIC method is possible. Assuming the number of TRA transmitters and receivers is enough, [52] shows

that the TR-MUSIC method can image extended targets and their approximate region of localisation or shape given the MDM.

The work in [56] carries out high resolution TWRI of spatially extended targets by using a Beamspace MUSIC approach. [56] assumes that the electrical properties of the front-wall are known. Also, [56] assumes that prior radar interrogation of the scene, which includes the wall but not the targets, is possible, to mitigate clutter and to suppress the echo due to the presence of the wall.

The method in [4] achieves the TWRI of stationary extended targets. [4] introduces the spatiotemporal windowing technique. To perform imaging, [4] combines the spatiotemporal windowing of the MDM with each of the methods Centre Frequency (CF)-MUSIC and UWB-MUSIC. Hence, [4] achieves the radar imaging of targets hidden behind a wall, which is not possible in the case where spatiotemporal windowing is not applied. The work in [4] assumes no knowledge of the geometrical or electrical properties of the obscuring wall.

As the TR-MUSIC-based approaches work on the null subspace of a MDM (or a differential MDM for the radar imaging of moving targets), methods to identify the signal and null subspace are important to the imaging performance of any TR-MUSIC-based approaches [52]. This is especially true for the case of extended targets, where the MDM is nonrank-deficient and the singular value spectrum decays more gradually to zero, rather than having a value gap and hence the determination of the signal and null subspaces is difficult [52, 57]. In the case of radar imaging of stationary well-resolved pointlike targets in homogeneous propagation media under isotropic scattering, we can computationally estimate [58] the size of the signal subspace of the MDM equal to the number of the targets which return echoes to the TRA [56, 58]. The works in [56, 59] assume that prior information on the number of targets is available and fix the dimension of the signal subspace *a priori*.

Threshold criteria on singular values can be used to determine the dimension of the signal subspace of the MDM in cases where there are anisotropic scattering and/or significant clutter or noise [45], and/or extended targets [55, 57, 60–63]. Such criteria may depend on the characteristics of each individual imaging scenario, including the frequency of interest, the intensity of clutter and noise [45], different background media [58] and discrepancies between the assumed versus true background [52]. [52] manually inspects the semilogarithmic plot of the MDM's singular values distribution for a "knee"to set the dimension of the signal

subspace approximately equal to the index of the singular value where the "knee" occurs. [62, 63] set the dimension of the signal subspace based on the ratio of the largest singular value to the first null subspace singular value and a threshold derived from the Signal-to-Noise Ratio (SNR) of the received signals. [57] proposes a double-thresholding strategy based on the total signal energy of the MDM. A threshold of 10% of the maximum singular value at each frequency is commonly exercised with the TR-MUSIC method [45]. In this thesis, we call this approach as *the 10% approach*. The authors in [4, 29, 64] set the dimension of the signal subspace based on the maximum ratio of consecutive singular values. We name this approach as *the ratios approach*.

2.4 Effects of lossy media on TR techniques

Media whose constitutive parameters are functions of frequency are called *dispersive* [65]. In dispersive media, different temporal frequencies travel with different speeds. In many real world applications, UWB electromagnetic waves penetrate lossy and dispersive media, e.g. concrete or brick in through-the-wall imaging applications; soil, rocks, and ice in GPR applications; and most human tissues in biomedical applications.

2.4.1 The vector wave equation for the electric field in lossy media

In dispersive non-magnetic media, the permittivity ε is frequency-dependent. For the case of inhomogeneous and dispersive media, the constitutive relation of the electric flux density $\boldsymbol{D}$ (in C/m^2) to the $\boldsymbol{E}$ field (in V/m) is given by

$$\boldsymbol{D} = \varepsilon(\boldsymbol{r}, t) * \boldsymbol{E}(\boldsymbol{r}, t) \tag{2.44}$$

where $\varepsilon(\boldsymbol{r}, t)$ is the permittivity of the dispersive medium assuming non-magnetised stationary linear and isotropic media. By the term *linear* medium is meant that the conductivity, dielectric constant, and permeability of the medium are all independent of the level of the applied fields [66]. In (2.44), $\varepsilon(\boldsymbol{r}, t)$ varies with frequency, as in $\varepsilon(\boldsymbol{r}, t) = \mathcal{F}^{-1}\{\varepsilon(\boldsymbol{r}, \omega)\}$ where $\mathcal{F}^{-1}\{\,\}$ denotes the inverse Fourier transform. In stationary non-magnetic inhomogeneous dispersive isotropic linear media, Gauss's law for the electric field, the Maxwell-Faraday equation, and the

Maxwell-Ampère equation are written as

$$\nabla \cdot \boldsymbol{E}(\boldsymbol{r},t) = 0 \qquad \text{Gauss's law for } \boldsymbol{E} \tag{2.45}$$

$$\nabla \times \boldsymbol{E}(\boldsymbol{r},t) = -\frac{\partial}{\partial t}\boldsymbol{B}(\boldsymbol{r},t) \qquad \text{Maxwell-Faraday} \tag{2.46}$$

$$\nabla \times \boldsymbol{H}(\boldsymbol{r},t) = \sigma_{\mathrm{s}}(\boldsymbol{r})\boldsymbol{E}(\boldsymbol{r},t) + \frac{\partial}{\partial t}\boldsymbol{D}(\boldsymbol{r},t) \qquad \text{Maxwell-Ampère} \tag{2.47}$$

where $\boldsymbol{B}(\boldsymbol{r},t)$ is the magnetic flux density in $\mathrm{Wb/m^2} \equiv \mathrm{T}$, $\boldsymbol{H}(\boldsymbol{r},t)$ is the magnetic field intensity in A/m, $\sigma_{\mathrm{s}}(\boldsymbol{r})$ is the static conductivity in S/m. The constitutive relation of $\boldsymbol{H}(\boldsymbol{r},t)$ and $\boldsymbol{B}(\boldsymbol{r},t)$ is

$$\boldsymbol{B}(\boldsymbol{r},t) = \mu(\boldsymbol{r})\boldsymbol{H}(\boldsymbol{r},t) \tag{2.48}$$

where $\mu(\boldsymbol{r})$ is the magnetic permeability. Substituting $\boldsymbol{D}(\boldsymbol{r},t)$ in (2.44) and $\boldsymbol{H}(\boldsymbol{r},t)$ in (2.48) into (2.47)

$$\nabla \times \boldsymbol{B}(\boldsymbol{r},t) = \mu(\boldsymbol{r})\big(\sigma_{\mathrm{s}}(\boldsymbol{r})\boldsymbol{E}(\boldsymbol{r},t)\big) + \mu(\boldsymbol{r})\frac{\partial}{\partial t}\big(\varepsilon(\boldsymbol{r},t) * \boldsymbol{E}(\boldsymbol{r},t)\big). \tag{2.49}$$

Differentiating both sides of (2.49) with respect to t

$$\frac{\partial}{\partial t}\big(\nabla \times \boldsymbol{B}(\boldsymbol{r},t)\big) = \mu(\boldsymbol{r})\frac{\partial}{\partial t}\big(\sigma_{\mathrm{s}}(\boldsymbol{r})\boldsymbol{E}(\boldsymbol{r},t)\big) + \mu(\boldsymbol{r})\frac{\partial^2}{\partial t^2}\big(\varepsilon(\boldsymbol{r},t) * \boldsymbol{E}(\boldsymbol{r},t)\big). \tag{2.50}$$

Taking the curl of (2.46)

$$\nabla \times \big(\nabla \times \boldsymbol{E}(\boldsymbol{r},t)\big) = -\frac{\partial\big(\nabla \times \boldsymbol{B}(\boldsymbol{r},t)\big)}{\partial t}. \tag{2.51}$$

The left-hand side (LHS) of (2.51) can be expressed using the definition of the vector Laplacian

$$\nabla^2\boldsymbol{E}(\boldsymbol{r},t) \equiv \nabla\big(\nabla \cdot \boldsymbol{E}(\boldsymbol{r},t)\big) - \nabla \times \big(\nabla \times \boldsymbol{E}(\boldsymbol{r},t)\big). \tag{2.52}$$

Using (2.45), (2.52) becomes

$$\nabla \times \big(\nabla \times \boldsymbol{E}(\boldsymbol{r},t)\big) = -\nabla^2\boldsymbol{E}(\boldsymbol{r},t). \tag{2.53}$$

With (2.53), we re-write (2.51) as

$$\nabla^2 \boldsymbol{E}(\boldsymbol{r},t) = \frac{\partial\big(\nabla \times \boldsymbol{B}(\boldsymbol{r},t)\big)}{\partial t}. \tag{2.54}$$

Using (2.54) into (2.50), we obtain

$$\nabla^2 \boldsymbol{E}(\boldsymbol{r},t) - \mu(\boldsymbol{r})\frac{\partial}{\partial t}\big(\sigma_{\mathrm{s}}(\boldsymbol{r})\boldsymbol{E}(\boldsymbol{r},t)\big) - \mu(\boldsymbol{r})\frac{\partial^2}{\partial t^2}\big(\varepsilon(\boldsymbol{r},t) * \boldsymbol{E}(\boldsymbol{r},t)\big) = 0. \tag{2.55}$$

(2.55) is a wave equation in the case of electromagnetic wave propagation in lossy and dispersive media under the assumptions of linear and isotropic media and a source-free environment. As compared to (2.1), we note the presence of a first order temporal derivative in (2.55). The presence of a first order temporal derivative in (2.55) is sufficient for the breaking of the time-reversal invariance of the wave equation and hence the corresponding propagation media are non-reciprocal.

2.4.2 Complex permittivity

We write (2.47) in frequency domain, assuming propagation in an infinite homogeneous conductive medium (such as a lossy dielectric), for simplicity, as in

$$\nabla \times \boldsymbol{H}(\omega) = \sigma_{\mathrm{s}}\boldsymbol{E}(\omega) + \jmath\omega\varepsilon(\omega)\boldsymbol{E}(\omega) \tag{2.56}$$

$$= \jmath\omega \underbrace{\left(\varepsilon(\omega) - \jmath\frac{\sigma_{\mathrm{s}}}{\omega}\right)} \boldsymbol{E}(\omega). \tag{2.57}$$

The underlined expression in (2.57) can be replaced by a single frequency-dependent complex quantity. Hence, the complex permittivity $\epsilon(\omega)$ in (2.57) can be considered as [65] [66]

$$\epsilon(\omega) = \varepsilon(\omega) - \jmath\frac{\sigma_{\mathrm{s}}}{\omega} \tag{2.58}$$

in F/m. $\epsilon(\omega)$ is defined in terms of its real and imaginary parts, as in [65] [66]

$$\epsilon(\omega) \triangleq \epsilon'(\omega) - \jmath\epsilon''(\omega) \tag{2.59}$$

where $\epsilon'(\omega), \epsilon''(\omega)$ are real functions of ω. Comparing (2.59) with (2.58) yields

$$\varepsilon(\omega) = \epsilon'(\omega) \qquad \sigma_{\mathrm{s}} = \omega\epsilon''(\omega) \tag{2.60}$$

for the case where (2.57) holds. (2.60) shows that $\epsilon'(\omega)$ is equal to the real permittivity, which corresponds to electric field energy storage in the dielectric, whereas $\omega\epsilon''(\omega)$ assumes the role of conductivity in a lossy dielectric. By substituting (2.60) into (2.57) we obtain

$$\nabla \times \boldsymbol{H}(\omega) = \omega\epsilon''(\omega)\boldsymbol{E}(\omega) + \jmath\omega\epsilon'(\omega)\boldsymbol{E}(\omega). \tag{2.61}$$

In (2.61), the conduction current density $\boldsymbol{J}(\omega) = \sigma_{\mathrm{s}}\boldsymbol{E}(\omega)$ is not explicitly noted, since comparing (2.61) with (2.56) shows that an *equivalent conduction loss* process is accounted for by the term $\omega\epsilon''(\omega)\boldsymbol{E}(\omega)$ in (2.61) [66].

A dispersive medium acts as a filter on UWB signals that propagate in it [40]. For such a medium, the electric field at a single frequency ω can be expressed as [66]

$$\boldsymbol{E}(\boldsymbol{r},\omega) = \boldsymbol{E}_0(\boldsymbol{r})e^{-\jmath\omega\sqrt{\mu\epsilon(\omega)}\boldsymbol{r}} \tag{2.62}$$

where $\boldsymbol{E}_0(\boldsymbol{r})$ is a frequency-independent vector. In (2.62), we also assume that the complex permittivity $\epsilon(\omega)$ is spatially invariant, for simplicity. The positive $\epsilon'(\omega)$ introduces phase delays to $\boldsymbol{E}(\boldsymbol{r},\omega)$. $\epsilon''(\omega)$ causes attenuation to $\boldsymbol{E}(\boldsymbol{r},\omega)$. The Kramers-Kronig relations dictate that when ϵ' varies as a function of frequency, then ϵ'' also varies with frequency due to causality [15] [65, p. 79]. Hence, waves travelling in a dispersive medium are affected by both frequency-dependent phase shifts and frequency-dependent attenuation.

These effects due to $\epsilon(\omega)$ get accumulated during both forward propagation and backpropagation in a TR experiment [40]. Phase delays on $\boldsymbol{E}(\boldsymbol{r},\omega)$ caused due to dispersive media during TR forward propagation are exactly compensated by the TR process during backpropagation. This is because the signals participating in the TR process are phase conjugated coherently along the entire bandwidth. However, TR techniques do not compensate the attenuation forward- and back-propagating signals undergo. As a result, the refocusing performance of TR techniques is degraded in dispersive media relative to the lossless case [15, 16, 45], i.e. the refocusing spot is wider (the refocusing resolution is degraded) and the magnitude of the refocusing field is weaker, or refocusing is not achieved at all.

2.5 Compensation for the effects of medium dispersion

As demonstrated in Section 2.4, the TR invariance of the wave equation breaks in the presence of lossy propagation media. While the TR process itself compensates for the additional phase shift incurred by dispersion, it does not compensate for the amplitude attenuation the TR signals undergo during both forward and back-propagations [15, 16]. This attenuation degrades the resolution of the TR refocusing relative to the lossless and non-dispersive case. Inverse filters can be employed to compensate for the attenuation of the TR signals and enhance the resolution of the TR imaging. In the case of random and/or inhomogeneous propagation media, approximate inverse filters can be used [12, 15]. This practice can be applied for TR-based microwave imaging applications where the obtainment of qualitative radar images, rather than quantitative fields, is acceptable [12] [67, Section 7.2.3.3]. Early literature dealing with the enhancement of the TR refocusing resolution by compensating the effects of the additional attenuation caused by propagation media can be found in studies on acoustics. A method for the refocusing and steering of an ultrasonic beam through the human skull bone has been developed by [68], as the focusing performance of the TR method is affected by the severe ultrasonic attenuation in the skull. The work in [69] performs the DORT method for the ultrasonic localisation of a single point-like scatterer inside a water tank. [69] proposes an amplitude compensation technique to enhance the resolution of target localisation and to improve the SNR at the target location while backpropagating the TRO eigenvectors.

The authors in [12] employ the conventional TR technique together with a modified Finite Difference Time Domain (FDTD) method to achieve microwave detection of breast cancer. The work in [12] assumes an inhomogeneous 2D breast model which is lossy, however nondispersive. The method in [12] requires knowledge of average real-valued permittivity and conductivity for the breast model. Also, [12] assumes that certain properties of the lossy but nondispersive background are unknown, such the thickness of the breast's skin and various inhomogeneities of the breast. The authors in [12] propose a modification of the standard FDTD [70] technique by considering the time-reversed $\boldsymbol{E}$ and $\boldsymbol{H}$ fields and incorporating the additive inverse of the medium's conductivity for the TR

backpropagation. The modified FDTD method introduced by [12] effectively performs the TR backpropagation in an inversed version of the background medium that compensates losses rather than cause them. The authors in [12] speculate that their work can be applied as an approximation on cases involving dispersive propagation media, but no such study is made in [12]. [13] applies the method from [12] considering a dispersive human breast model during the backpropagation stage. However, [13] does not modify the method from [12] to account for medium dispersiveness.

The work in [16] compensates the dispersive effects in UWB TR applications by making use of time-dependent inverse filtering with Short-Time Fourier Transforms (STFTs). In this way, [16] improves the refocusing of time-reversed electromagnetic waves and to increase the signal strength at the location of refocusing. The work in [16] constructs the windowed inverse filters by comparing the solution of the wave equation in the dispersive propagation medium at various propagation distances against a corresponding nondispersive test medium. There are three major drawbacks to adopting the inverse filter production proposed by [16]. First, it is empirical, as it requires a manual examination of the spectral density of the received signals to assess whether the noise levels at individual frequencies are unacceptably high, depending on the application. The amplification of noise-affected frequencies is minimised by manually adjusting the filtering process. Second, it assumes perfect knowledge of the dispersive characteristics of the propagation media. Finally, it is time consuming, as it implies prior realisation of one experiment with the nondispersive test medium.

Later, [71] improved the method in [16] by introducing a threshold approach to minimise the amplification of the noise in the inverse filters in [16]. The work in [71] investigates the application of different window function types and lengths to optimise the selection of the parameters of the STFT filters. While [71] automates the noise reduction process, the requirements of performing one extra experiment with the non-dispersive test medium and of perfect knowledge of the dispersive characteristics of the propagation media persist. Another limitation imposed by [71] is that it assumes knowledge of the location of the scatterers during the optimisation process. Such information may not be available in real-life applications. Besides, both [71] and [16] consider only point-like Perfect Electric Conductor (PEC) scatterers.

More recently, the authors in [1] propose an adaptive-window scheme based on

the CWT of discrete-time signals received by a TRA. Hence, [1] performs the Discrete Time Wavelet Transform (DTWT) [72] of the received signals. The wavelet transform method applies a temporally long window to the received signals at the lower frequencies of the spectrum (large scales) and a temporally short window at the higher frequencies of the spectrum (small scales). Therefore, it is well-suited for time-dependent filter implementations in terms of time and frequency localisation [1]. A wavelet transform-based technique similar to [1] was earlier proposed by [73] for the resolution enhancement of seismic records. The method in [1] uses stabilised inverse filters in the wavelet domain to increase the resolution of the TR refocusing of UWB signals. Each of these stabilised inverse filters is produced using the complex permittivity of the propagation medium, which is assumed to be known. [1] investigates the statistical stability of the proposed approach and applies its algorithm to the detection of a lung tumour in a DHP by considering implantable TRA elements in the fat around the torso. The work in [1] uses the value of the complex permittivity of one dominant propagation medium at the centre frequency of the interrogating UWB pulse to create the inverse filters without taking into account the frequency dependency of propagation media. Also, [1] does not apply inverse filtering on the lower half scales to avoid amplification of high frequency noise without accounting for the actual frequency spectrum of the interrogating pulse.

2.6 Summary

This chapter presented the conventional TR technique and its applications in the fields of electromagnetics and imaging. In this chapter, we discussed selective focusing effects by utilising the decomposition of the TRO. We presented conventional TR-based subspace imaging methods, including the TR-MUSIC method for a single frequency of interest and the UWB-MUSIC method which is practically performed over a wide bandwidth. Further, we reviewed TR-based techniques for the TWRI of extended targets. Dispersive media degrade the imaging performance of TR-based methods relative to lossless environments. In this chapter, we reviewed recently introduced methods for the compensation of the effects medium losses have on the TR imaging and the enhancement of the TR imaging in dispersive environments. We identified possible limitations with the state-of-the-art compensation method.

Chapter 3

Methodology

In this chapter, we introduce two novel algorithms. One performs the through-the-wall radar imaging of multiple extended moving targets under UWB sensing settings. The other algorithm achieves the enhancement of the resolution of UWB electromagnetic TR imaging of stationary targets in stationary dispersive propagation media.

3.1 Through-the-wall radar imaging of extended moving targets

This section introduces our proposed algorithm for the TWRI of multiple extended moving targets, which overlap in the range or cross-range directions. We call this algorithm the WF-MUSIC algorithm. The WF-MUSIC algorithm is based on the TR-MUSIC method and is applied over a UWB frequency spectrum. The WF-MUSIC algorithm employs the spatiotemporal windowing of the differential MDM. Hence, instead of relying on the null subspace from the whole differential MDM, we partition the differential MDM and diversify null subspaces that correspond to different scattering centres in such scenarios. This adaptive null subspace partitioning unveils hidden scattering phenomena otherwise dominated by other stronger ones. Moreover, we propose a method to identify the dimension of the signal subspace of a differential MDM.

3.1.1 Formation of the differential MDM

The TR-MUSIC method makes use of a TRA to form an MDM [74]. The MDM can be expressed in time domain as

$$\boldsymbol{K}(t) = \begin{pmatrix} \kappa_{1,1}(t) & \dots & \kappa_{1,\mathcal{N}}(t) \\ \vdots & \ddots & \vdots \\ \kappa_{\mathcal{N},1}(t) & \dots & \kappa_{\mathcal{N},\mathcal{N}}(t) \end{pmatrix} \tag{3.1}$$

where $\kappa_{\zeta,\xi}$ is the signal recorded by the ξ-th TRA element when the scene is probed by the ζ-th TRA element and $\mathcal{N}$ is the total number of antenna elements in the TRA.

We probe the scene of interest twice: at t_1 and at a later time t_2, when the targets have moved with a displacement shorter than the wavelength [75]. For the variable t in (3.1), we assume $t = 0$ when the radar interrogation starts each time we probe the scene. However, the experiments in this thesis are carried out in the discrete domain. For this reason, this thesis adopts discrete-time notation. Hence, (3.1) becomes

$$\boldsymbol{K}[n] = \begin{pmatrix} \kappa_{1,1}[n] & \dots & \kappa_{1,\mathcal{N}}[n] \\ \vdots & \ddots & \vdots \\ \kappa_{\mathcal{N},1}[n] & \dots & \kappa_{\mathcal{N},\mathcal{N}}[n] \end{pmatrix} \qquad n = 1, 2, \dots, N \tag{3.2}$$

with $\boldsymbol{K}[n] = \boldsymbol{K}((n-1)T_{\mathrm{s}})$, where n is the discrete time variable, T_{s} is the sampling period and N is the total number of sampling points in the time domain signal. We obtain the discrete time domain MDMs $\boldsymbol{K}|_{t_1}[n]$ and $\boldsymbol{K}|_{t_2}[n]$ respectively. We form the differential MDM, $\boldsymbol{K}_{\mathbf{d}}$, by taking the difference of $\boldsymbol{K}|_{t_1}$ and $\boldsymbol{K}|_{t_2}$ in time domain, as in

$$\boldsymbol{K}_{\mathbf{d}}[n] = \boldsymbol{K}|_{t_2}[n] - \boldsymbol{K}|_{t_1}[n]. \tag{3.3}$$

This differential operation has two functions. First, with (3.3), $\boldsymbol{K}_{\mathbf{d}}[n]$ contains the perturbation signal due to the displacement of the targets [29] [76]. Second, (3.3) helps with the partial elimination of the fixed background scattering in $\boldsymbol{K}_{\mathbf{d}}[n]$ [29] [76]. For example, in the case of through-the-wall radar imaging, while both $\boldsymbol{K}|_{t_2}[n]$ and $\boldsymbol{K}|_{t_1}[n]$ would contain strong radar returns from the intervening wall, these are eliminated in $\boldsymbol{K}_{\mathbf{d}}[n]$.

3.1.2 Spatial windowing

We form a set of spatial windows [4] of $\mathcal{N}_{\text{sw}}$ antennas out of the whole available TRA where $1 \leq \mathcal{N}_{\text{sw}} \leq \mathcal{N}$. The l-th sub-differential MDM $\boldsymbol{K}_{\mathbf{d}l}$ is obtained as in

$$\boldsymbol{K}_{\mathbf{d}l}[n] = \begin{pmatrix} \kappa_{\text{d}l,l}[n] & \dots & \kappa_{\text{d}l,\mathcal{L}}[n] \\ \vdots & \ddots & \vdots \\ \kappa_{\text{d}\mathcal{L},l}[n] & \dots & \kappa_{\text{d}\mathcal{L},\mathcal{L}}[n] \end{pmatrix} \tag{3.4}$$

where $\mathcal{L} = l + \mathcal{N}_{\text{sw}} - 1$ and $1 \leq l \leq \mathcal{N} + 1 - \mathcal{N}_{\text{sw}}$. The total number of spatial windows L is given by

$$L = \mathcal{N} + 1 - \mathcal{N}_{\text{sw}}. \tag{3.5}$$

In case where spatial windowing is not applied, we can equivalently consider that there is only one spatial window with $L = 1$ and $\mathcal{N}_{\text{sw}} \equiv \mathcal{N}$.

3.1.3 Temporal windowing

We use the Hann window function, W, to perform the temporal windowing [4] of each spatial window $\boldsymbol{K}_{\mathbf{d}l}[n]$. We shift $W[n]$ in time to obtain a set of temporal windows which covers the signal $\boldsymbol{K}_{\mathbf{d}l}[n]$ for the time duration of interest. The m-th temporal window of duration P is obtained as

$$W_m[n] = \begin{cases} \frac{1}{2}\left(1 - \cos\left(\frac{2\pi((n-1) - \nu_m)}{P}\right)\right), & \frac{P(m-1)}{2} \leq n - 1 \leq P + \frac{P(m-1)}{2} \\ 0, & \text{otherwise} \end{cases} \tag{3.6}$$

where ν_m is the time shift applied so that adjacent Hann windows overlap by 50% in time domain.

A 50% overlap in time is chosen for the shifted Hann windows, as no signal is lost and the windows add up to unit magnitude [77]. Let m be an index for the m-th slided temporal window, W_m, and $m = 1$ correspond to the non-slided first window $W_1(t) \equiv W(t)$. The m-th slided window has a time shift ν_m. As the Hann windows have an overlap of 50%, it holds for the m-th temporal window

$$\nu_m = \lfloor (m-1)(0.5P) \rfloor \tag{3.7}$$

where $\lfloor\ \rfloor$ is the floor function. To find the number M of Hann temporal windows

needed to cover a signal of duration N, we require that the time shift in (3.7) is equal to the duration of the signal on which to apply temporal windowing, minus one temporal window duration P, so that we discard any windows that last past time $n = N$. That is, we set $m \triangleq M$ and $\nu_M = N - P$ into (3.7), and thus obtain

$$M = 1 + \left\lceil \frac{N - P}{0.5P} \right\rceil \tag{3.8}$$

where $\lceil\ \rceil$ is the ceiling function. M sub-differential MDMs are formed as in

$$\begin{aligned} \boldsymbol{K}_{\mathbf{d}l,m}[n] &= W_m[n]\boldsymbol{K}_{\mathbf{d}l}[n] \\ &= \begin{pmatrix} W_m[n]\kappa_{\mathrm{d}l,l}[n] & \dots & W_m[n]\kappa_{\mathrm{d}l,\mathcal{L}}[n] \\ \vdots & \ddots & \vdots \\ W_m[n]\kappa_{\mathrm{d}\mathcal{L},l}[n] & \dots & W_m[n]\kappa_{\mathrm{d}\mathcal{L},\mathcal{L}}[n] \end{pmatrix} \end{aligned} \tag{3.9}$$

with $1 \leq m \leq M$. The set of all the sub-differential MDMs provide temporal and spatial diversity in addition to being UWB signals. In case where the temporal windowing technique is not applied, we can equivalently consider that there is only one rectangular temporal window, that is $m = M = 1$ and $W_1[n] = 1$, $1 \leq n \leq N$.

3.1.4 Limits on the selection of the windowing parameters

Like the method in [4], the effectiveness of our spatiotemporal windowing approach depends on the size of each spatial window $\mathcal{N}_{\mathrm{sw}}$ and on the width P of each temporal window. The value of P has to be large enough to contain the full excitation pulse width and also for $\boldsymbol{K}_{\mathbf{d}l,m}[n]$ to contain sufficient signal diversity to obtain reasonable imaging results [4].

The optimal value of $\mathcal{N}_{\mathrm{sw}}$ depends on each specific scenario. The choice of $\mathcal{N}_{\mathrm{sw}}$ needs to allow at least one signal subspace vector per target returning significant echoes in each $\boldsymbol{K}_{\mathbf{d}l,m}[n]$ and at least one null subspace vector for the TR-MUSIC method to operate on [52]. More than one null subspace vectors may be needed in case of a noisy propagation environment [52].

3.1.5 The WF-MUSIC imaging functional

3.1.5.1 Decomposition of the sub-differential MDMs

We form $\boldsymbol{K}_{\mathbf{d}l,m}[k]$ by applying the Fast Fourier Transform (FFT) on the elements of $\boldsymbol{K}_{\mathbf{d}l,m}[n]$, where k is the discrete FFT frequency bin that corresponds to frequency f. By performing the SVD of $\boldsymbol{K}_{\mathbf{d}l,m}[k]$ we obtain

$$\boldsymbol{K}_{\mathbf{d}l,m}[k] = \boldsymbol{U}_{l,m}[k]\, \boldsymbol{\Sigma}_{l,m}[k]\, \boldsymbol{V}^{\mathrm{H}}_{l,m}[k] \tag{3.10}$$

where $\boldsymbol{U}_{l,m}[k]$ and $\boldsymbol{V}_{l,m}[k]$ are $\mathcal{N}_{\mathrm{sw}} \times \mathcal{N}_{\mathrm{sw}}$ complex unitary matrices whose columns are the left and right singular vectors of $\boldsymbol{K}_{\mathbf{d}l,m}[k]$, $\boldsymbol{u}_\iota[k]$ and $\boldsymbol{v}_\iota[k]$ respectively, with $1 \leq \iota \leq \mathcal{N}_{\mathrm{sw}}$ respectively. $\boldsymbol{\Sigma}_{l,m}[k]$ is a rectangular diagonal matrix with real non-negative entries. The entries of $\boldsymbol{\Sigma}_{l,m}[k]$ are the singular values $\sigma^{l,m}_\iota[k]$ of $\boldsymbol{K}_{\mathbf{d}l,m}[k]$, where $\sigma^{l,m}_1[k] \geq \sigma^{l,m}_2[k] \geq \cdots \geq \sigma^{l,m}_{\mathcal{N}_{\mathrm{sw}}}[k] \geq 0$.

3.1.5.2 Establishing the dimension of the signal subspace

We regard the first $\mathcal{N}^{\Theta}_{l,m}[k]$ ($< \mathcal{N}_{\mathrm{sw}}$) singular vectors of $\boldsymbol{K}_{\mathbf{d}l,m}[k]$ as its signal subspace. Contrary to the 10% approach [45] and the ratios approach [4, 29], we select $\mathcal{N}^{\Theta}_{l,m}[k] = \mathcal{N}^{\Theta\Sigma}_{l,m}[k]$ as the minimum value which satisfies

$$\sum_{i=1}^{\mathcal{N}^{\Theta\Sigma}_{l,m}[k]} \sigma^{l,m}_i[k] \geq 90\% \cdot \sum_{p=1}^{\mathcal{N}_{\mathrm{sw}}} \sigma^{l,m}_p[k] \tag{3.11}$$

where the constant factor (90%) was empirically selected.

The 10% approach [45] sets the signal subspace dimension as $\mathcal{N}^{\Theta}_{l,m}[k] = \mathcal{N}^{\Theta 10\%}_{l,m}[k]$ where $\mathcal{N}^{\Theta 10\%}_{l,m}[k]$ is the largest integer which satisfies

$$\sigma^{l,m}_{\mathcal{N}^{\Theta 10\%}_{l,m}[k]}[k] \geq 10\% \cdot \sigma^{l,m}_1[k]. \tag{3.12}$$

The ratios approach [4] considers the signal space dimension as $\mathcal{N}^{\Theta}_{l,m}[k] = \mathcal{N}^{\Theta\div}_{l,m}[k]$ where $\mathcal{N}^{\Theta\div}_{l,m}[k]$ is the integer which satisfies

$$\frac{\sigma^{l,m}_{\mathcal{N}^{\Theta\div}_{l,m}[k]}[k]}{\sigma^{l,m}_{\mathcal{N}^{\Theta\div}_{l,m}[k]+1}[k]} = \max_{1 \leq \iota \leq (\mathcal{N}_{\mathrm{sw}}-1)} \left(\frac{\sigma^{l,m}_\iota[k]}{\sigma^{l,m}_{\iota+1}[k]} \right). \tag{3.13}$$

3.1.5.3 Obtainment of radar images

We propose a novel imaging functional, $\mathcal{M}_{l,m}[\boldsymbol{x}]$, to perform radar imaging of each spatiotemporal window, where $\boldsymbol{x}$ is the discretised spatial location vector. For the l-th spatial window and m-th temporal window, we define $\mathcal{M}_{l,m}[\boldsymbol{x}]$ as

$$\mathcal{M}_{l,m}[\boldsymbol{x}] = \frac{1}{\min\limits_{k\in\Omega_k}\left(\sum\limits_{\iota=\mathcal{N}^{\Theta}_{l,m}[k]+1}^{\mathcal{N}_{\text{sw}}} \left|\langle \boldsymbol{g}[\boldsymbol{x},k], \boldsymbol{v}_{\iota}^{*}[k]\rangle\right|\right)} \tag{3.14}$$

where Ω_k is the set of frequency bins of interest and $\boldsymbol{g}[\boldsymbol{x},k]$ is the free space Green function steering vector [41] at spatial location $\boldsymbol{x}$ in the discretised domain. We call the right-hand side (RHS) of (3.14) as the FQ-MUSIC imaging functional. The FQ-MUSIC imaging functional effectively performs the TR-MUSIC technique across all frequency bins in Ω_k, for each imaging pixel $\boldsymbol{x}$. Then, for each imaging pixel, the FQ-MUSIC technique "selects" the value of the TR-MUSIC functional at the frequency that yields the strongest value. The FQ-MUSIC can therefore be used as a broadband technique. If Ω_k contains only one frequency, the FQ-MUSIC functional reduces to the TR-MUSIC one. In this thesis, we use a UWB spectrum for Ω_k in our experiments. We normalise $\mathcal{M}_{l,m}[\boldsymbol{x}]$ as in

$$\tilde{\mathcal{M}}_{l,m}[\boldsymbol{x}] = \frac{\mathcal{M}_{l,m}[\boldsymbol{x}]}{\max\limits_{\boldsymbol{x}}(\mathcal{M}_{l,m}[\boldsymbol{x}])}. \tag{3.15}$$

Our final radar image $\tilde{\mathcal{M}}[\boldsymbol{x}]$ is

$$\tilde{\mathcal{M}}[\boldsymbol{x}] = \max_{l,m}\Big(\tilde{\mathcal{M}}_{l,m}[\boldsymbol{x}]\Big). \tag{3.16}$$

We call (3.16) the WF-MUSIC imaging functional. The WF-MUSIC imaging functional ensures that no shadowing of any moving target occurs in the final radar image, as long as each target is successfully detected in at least one spatiotemporal window. We summarise our proposed radar imaging approach in Figure 3.1 as a block diagram.

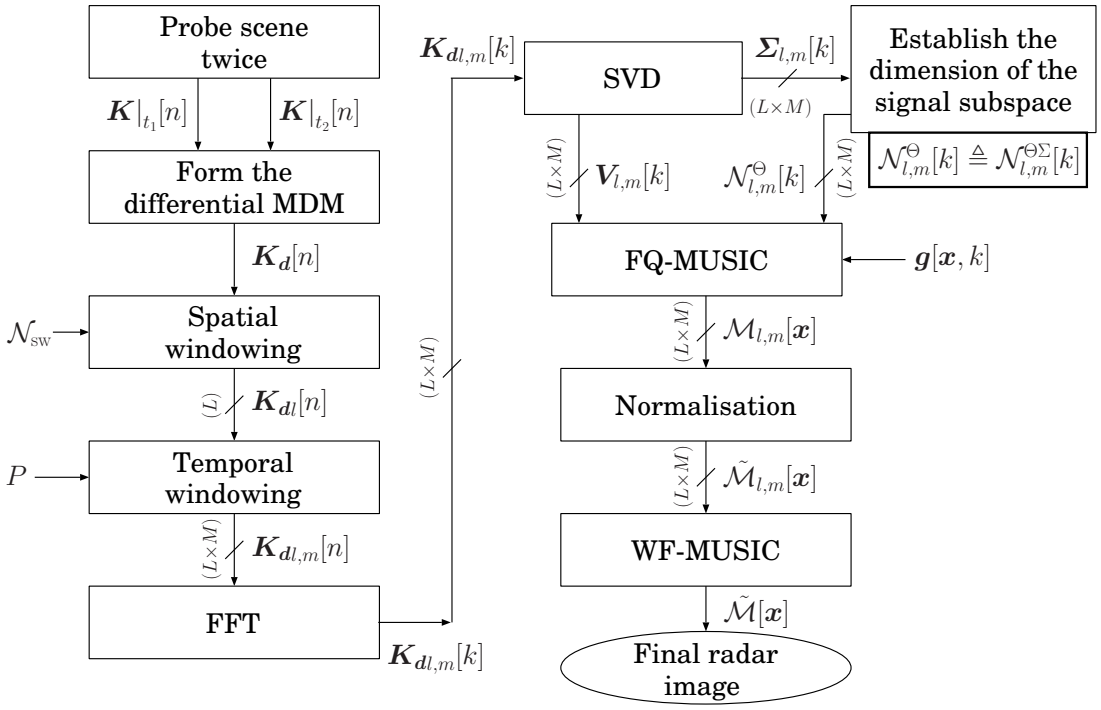

Figure 3.1: Block diagram of our proposed radar imaging approach for the detection of multiple extended moving targets.

3.2 Resolution enhancement of TR imaging in dispersive media

This section introduces our proposed algorithm for the resolution enhancement of UWB electromagnetic TR imaging of stationary targets in dispersive propagation media.

There have been proposed a few methods for the resolution enhancement of UWB TR imaging in dispersive media by the existing literature. As we detailed in Section 2.5, the STFT-based approaches proposed by [16] and [71] require a prior realisation of one experiment with a nondispersive test medium, which may be time-consuming. Also [71] assumes knowledge of the location of the scatterers, to automate the otherwise manual adjustment of noise levels. Prior information of the targets' location may not be available in most scenarios. The wavelets-based method in [1] overcomes the aforementioned requirements of the STFT-based approaches. However, the method in [1] considers only the centre-frequency permittivity of one dominant propagation medium and does not adjust the inverse filtering automatically according to the spectrum of the interrogating

pulse. Here, we propose a wavelet-based method which corrects and improves the method in [1].

3.2.1 Creation of the inverse filters

Let $x(t)$ be the signal received by one TRA element. The signal $x(t)$ is sampled and represented in discrete time domain as

$$x[n] = x((n-1)T_{\mathrm{s}}) \qquad n = 1, 2, 3, \ldots, N. \tag{3.17}$$

We use the complex Morlet function as the analysing (*mother*) wavelet for the DTWT of $x[n]$, following [1]. Let $\psi_{\mathrm{M0}}(\eta)$ of (3.18)

$$\psi_{\mathrm{M0}}(\eta) = \frac{1}{\sqrt[4]{\pi}} e^{\jmath\omega_{\mathrm{M}}\eta} e^{-\eta^2/2} \tag{3.18}$$

be the mother wavelet function where $\omega_{\mathrm{M}} = 2\pi f_{\mathrm{M}}$ is the dimensionless central angular frequency of the mother wavelet, f_{M} is the corresponding frequency, and $\jmath = \sqrt{-1}$. For (3.18), a value of $\omega_{\mathrm{M}} > \pi\sqrt{2/\ln 2} \approx 5.336$ must be chosen so that $\psi_{\mathrm{M0}}(t)$ is approximately admissible [78, 79], since the complex Morlet function does not strictly meet the admissibility condition. The value $\omega_{\mathrm{M}} = 6$ is commonly employed in practice [78, 80, 81]. We express $\psi_{\mathrm{M0}}(\eta)$ in the scaled discrete frequency domain, to produce the *daughter* wavelets [82] as in [80]

$$\hat{\psi_{\mathrm{M0}}}[a_j\omega_k] = \begin{cases} \dfrac{1}{\sqrt[4]{\pi}} e^{-\frac{1}{2}(a_j\omega_k - \omega_{\mathrm{M}})^2} & \omega_k > 0 \\ 0 & \text{otherwise} \end{cases} \tag{3.19}$$

where a_j is the scale factor associated with each individual scale with index $j = 0, 1, \ldots, J$, given as a relation between the smallest resolvable scale a_0, the index j, and the scale step Δ_a by

$$a_j = 2^{j\cdot\Delta_a} a_0. \tag{3.20}$$

The number $1/\Delta_a$ corresponds to scales per scale factor octave (doubling). For this reason, $1/\Delta_a$ is termed the number of *voices per octave* [82] of the wavelet transform. ω_k is the $(k-1)$-th harmonic of the fundamental frequency which is

defined as

$$\omega_k = \begin{cases} \dfrac{2\pi(k-1)}{NT_\mathrm{s}} & k \leq \left\lfloor \dfrac{N}{2} \right\rfloor + 1 \\ -\dfrac{2\pi(N-k+1)}{NT_\mathrm{s}} & k > \left\lfloor \dfrac{N}{2} \right\rfloor + 1 \end{cases} \tag{3.21}$$

where $k = 1, 2, 3, \ldots, N$ is the frequency bin. The index of the largest scale J is computed by [80]

$$J = \left\lceil \frac{1}{\Delta_a} \log_2 \left(\frac{NT_\mathrm{s}}{a_0} \right) \right\rceil. \tag{3.22}$$

Δ_a controls the scale discretisation. Smaller values of Δ_a achieve finer discretisation of the scale parameter, which typically results in a higher-fidelity signal analysis. However, with smaller values of Δ_a, the amount of required computation increases, because there is a larger total number of scales and the DTWT is computed at each scale.

We normalise the wavelet function so that it has unit energy at each scale and to therefore guarantee that the DTWTs at each a_j are comparable to each other [80]:

$$\hat{\psi_\mathrm{M}}[a_j\omega_k] = \sqrt{\frac{2\pi a_j}{T_\mathrm{s}}} \hat{\psi_\mathrm{M0}}[a_j\omega_k]. \tag{3.23}$$

Our resolution enhancement process first converts $x[n]$ to the wavelet domain. Using the frequency-domain representation of the input signal and the normalised wavelet function, the DTWT of the signal $x[n]$ is expressed as

$$X[a_j, n] = \sum_{k=1}^{N} \frac{1}{N} X[k]\, \hat{\psi_\mathrm{M}}^{*}[a_j\omega_k]\, e^{\jmath\omega_k n T_\mathrm{s}} \tag{3.24}$$

where * represents the complex conjugation. The factor

$$X[k] \triangleq \sum_{\tau=1}^{N} x[\tau] e^{-\jmath\tau\frac{2\pi k}{N}} \tag{3.25}$$

is the Discrete Fourier Transform (DFT) of $x[n]$. By performing the convolution of $x[n]$ with $\psi_\mathrm{M0}[n/a_j]$ N times for each scale, we can approximate the CWT of $x(t)$ [80]. (3.24) achieves this by employing the convolution theorem, thus working with $\hat{x}[k]$ and $\hat{\psi_\mathrm{M}}[a_j\omega_k]$ instead of the time domain signals $x[n]$ and $\psi_\mathrm{M0}[n/a_j]$.

We apply inverse filtering to $X[a_j, n]$ in the wavelet domain to compensate the attenuation caused by the dispersive medium. To form the inverse filters, we compute the attenuation corresponding to $X[a_j, n]$. We assume a single point source of band-limited electromagnetic radiation placed inside a homogeneous and isotropic non-magnetic dispersive medium of infinite size. Let the complex permittivity of the linear and lossy propagation medium be noted as

$$\epsilon(f) = \epsilon'(f) - \jmath\epsilon''(f) \triangleq \epsilon_0\epsilon_{\mathrm{r}}(f) \tag{3.26}$$

where $\epsilon(f)$ has units of F/m, ϵ_0 is the vacuum permittivity, ϵ_{r} is the complex relative permittivity, and f is the frequency in Hz. We use the one-pole Debye relaxation model for the human tissues [71]

$$\epsilon_{\mathrm{r}}(f) = \epsilon_\infty + \frac{\epsilon_{\mathrm{s}} - \epsilon_\infty}{1 + \jmath 2\pi f\tau_D} - \jmath\frac{\sigma_{\mathrm{s}}}{2\pi f\epsilon_0} \tag{3.27}$$

where ϵ_∞ is the optical relative permittivity, ϵ_{s} is the static relative permittivity, τ_D is the relaxation time constant, σ_{s} is the static conductivity.

The attenuation factor of the propagation medium can be expressed as [66]

$$\alpha(f) = 2\pi f\frac{1}{\sqrt{2}c}\left[\sqrt{1 + \left(\frac{\epsilon''(f)}{\epsilon'(f)}\right)^2} - 1\right]^{1/2} \tag{3.28}$$

where $\alpha(f)$ is the attenuation factor associated with f in Np/m and c is the speed of light in the propagation medium.

Suppose a sinusoidal signal with frequency f at propagation distance z from the excitation source. This signal is subject to attenuation $\gamma(f, z)$ which is given by [66]

$$\gamma(f, z) = \exp(-\alpha(f) \cdot z). \tag{3.29}$$

We can express z in terms of time as

$$z(t) = c \cdot t \tag{3.30}$$

where t is the time of travel of the electric field plane wave. Using (3.30), (3.29)

becomes

$$\begin{aligned}\gamma(f,t) &= \exp(-\alpha(f)\cdot z(t)) \\ &= \exp\left(-\frac{2\pi f}{\sqrt{2}}\left[\sqrt{1+\left(\frac{\epsilon''(f)}{\epsilon'(f)}\right)^2}-1\right]^{1/2}\cdot t\right).\end{aligned} \tag{3.31}$$

We model (3.31) in wavelet domain as $\Gamma(a_j,t)$. To express $\Gamma(a_j,t)$ algebraically, we consider the relation between a_j and f. When (3.18) is used as the mother wavelet, an analytical relation between each scale factor a_j and one equivalent Fourier frequency $f = f_{\mathrm{e}}(\omega_{\mathrm{M}}, a_j)$ can be found. This relation can be obtained by taking the wavelet transform of a complex sinusoid at a known frequency and deriving the scale a_j at which the wavelet energy density is maximised, following the method in [83]. This yields [80, 83, 84]

$$f_{\mathrm{e}}(\omega_{\mathrm{M}}, a_j) = \frac{\omega_{\mathrm{M}} + \sqrt{2+\omega_{\mathrm{M}}{}^2}}{4\pi a_j}. \tag{3.32}$$

The derivation of (3.32) is provided in Section 3.2.2. Hence we express our wavelet domain model of the forward attenuation as

$$\begin{aligned}\Gamma(a_j,t) &= \exp\Big(-\alpha\big(f_{\mathrm{e}}(\omega_{\mathrm{M}},a_j)\big)\cdot z(t)\Big) \\ &= \exp\left(-\frac{2\pi f_{\mathrm{e}}(\omega_{\mathrm{M}},a_j)}{\sqrt{2}}\left[\sqrt{1+\left(\frac{\epsilon''\big(f_{\mathrm{e}}(\omega_{\mathrm{M}},a_j)\big)}{\epsilon'\big(f_{\mathrm{e}}(\omega_{\mathrm{M}},a_j)\big)}\right)^2}-1\right]^{1/2}\cdot t\right).\end{aligned} \tag{3.33}$$

By sampling (3.33) we have that

$$\begin{aligned}\Gamma[a_j,n] = \exp\Bigg(&-\frac{2\pi f_{\mathrm{e}}(\omega_{\mathrm{M}},a_j)}{\sqrt{2}} \\ &\cdot\left[\sqrt{1+\left(\frac{\epsilon''\big(f_{\mathrm{e}}(\omega_{\mathrm{M}},a_j)\big)}{\epsilon'\big(f_{\mathrm{e}}(\omega_{\mathrm{M}},a_j)\big)}\right)^2}-1\right]^{1/2}\cdot(n-1)T_{\mathrm{s}}\Bigg).\end{aligned} \tag{3.34}$$

The work in [1] does not make use of relation (3.32). Conversely, [1] dilates the central frequency of $x[n]$, i.e. f_c, by each scale factor to arbitrarily associate each scale factor to a frequency, as in

$$f = \frac{f_\mathrm{c}}{a_j}. \tag{3.35}$$

(3.35) has no physical meaning relating to the frequency content of $X[a_j, n]$ for constant a_j. In addition, the attenuation model in [1] uses the value for the permittivity of one medium only at f_c instead of taking into account the functional relationship of ϵ and f, and therefore ϵ and a_j. Thus, the model of attenuation in [1] is invalid for non-monochromatic waves propagating in dispersive media. With (3.34), our approach considers the effect of the attenuation on $x[n]$ across all scales – and hence, frequencies – of interest of $x[n]$.

To compensate for the effects of the frequency- and time-dependent attenuation, we construct inverse filters in the wavelet domain as in

$$H[a_j, n] = \frac{1}{\mathit{\Gamma}[a_j, n]}. \tag{3.36}$$

As the excitation wave travels beyond a certain distance from the source, its magnitude at high frequencies (small scales) becomes weaker than the noise. The inverse filters in (3.36) would amplify noise-dominated scales by an exponential function of time. To minimise such amplification of noise after long travel times, we stabilise (3.36) and form the stabilised inverse filters [73, 85, 86] of

$$H_\mathrm{s}[a_j, n] = \frac{\mathit{\Gamma}[a_j, n]}{\mathit{\Gamma}^2[a_j, n] + s^2} \tag{3.37}$$

where $s^2 \neq 0$ is the real stabilisation parameter. This parameter can be set empirically [73, 86, 87]. Alternatively, s^2 can be set as a ratio of variances of signal and noise, as a measure of SNR [73].

We produce the compensated wave sequence $Y[a_j, n]$ by applying $H_\mathrm{s}[a_j, n]$ on $X[a_j, n]$ in the wavelet domain as

$$Y[a_j, n] = \begin{cases} H_\mathrm{s}[a_j, n] X[a_j, n] & \text{if } f_\mathrm{min} \leq f_\mathrm{e}(\omega_\mathrm{M}, a_j) \leq f_\mathrm{max} \\ X[a_j, n] & \text{otherwise} \end{cases} \tag{3.38}$$

where f_min and f_max are the minimum and maximum frequencies of the spectrum

of the source excitation respectively. We do not apply the inverse filters outside of the frequency range of interest to practically avoid amplification of noise outside this range. With (3.38) our approach takes into account the entire frequency range of interest for the stabilised inverse filtering of $x[n]$.

The work in [1] sets H_{s} to 1 only for $0 \leq j \leq J/2$ to prevent the amplification of high frequency noise. While this choice of scale indices selects the higher part of the frequency spectrum used by the DTWT, it does not specify the exact frequency range where we are not interested. Consequently, the amplification of noise beyond $f_{\max}$ and below $f_{\min}$ is possible in [1].

Finally, we obtain the compensated signal in time domain $y[n]$ by taking the Inverse Discrete Time Wavelet Transform (IDTWT) of $Y[a_j, n]$ as in

$$y[n] = \frac{\Delta_a {T_{\mathrm{s}}}^{1/2}}{C_\delta \psi_{\mathrm{M0}}(0)} \sum_{j=0}^{J} \frac{\mathrm{Re}\{Y[a_j, n]\}}{\sqrt{a_j}} \tag{3.39}$$

where C_δ is a constant for each wavelet function and Re{ } is the real part of its complex argument. For the Morlet wavelet of (3.18), C_δ is calculated as [80]

$$C_\delta = \frac{\Delta_a {T_{\mathrm{s}}}^{1/2}}{\psi_{\mathrm{M0}}(0)} \sum_{j=0}^{J} \frac{\mathrm{Re}\{W_\delta[a_j]\}}{\sqrt{a_j}} \tag{3.40}$$

and $W_\delta[a_j, n]$ is the DTWT of the Kronecker delta sequence:

$$W_\delta[a_j] = \frac{1}{N} \sum_{k=1}^{N} \hat{\psi_{\mathrm{M}}}^{*}[a_j \omega_k]. \tag{3.41}$$

We apply the same process for each $x(t)$ received at each TRA element before the back-propagation stage. When we utilise our filter in an inhomogeneous scenario, we set ϵ in (3.33) to the complex permittivity of the dominant medium. We define as dominant the medium which covers the largest area of the propagation space between the TRA and the electric field source. Figure 3.2 summarises our proposed TR imaging resolution enhancement approach in a block diagram.

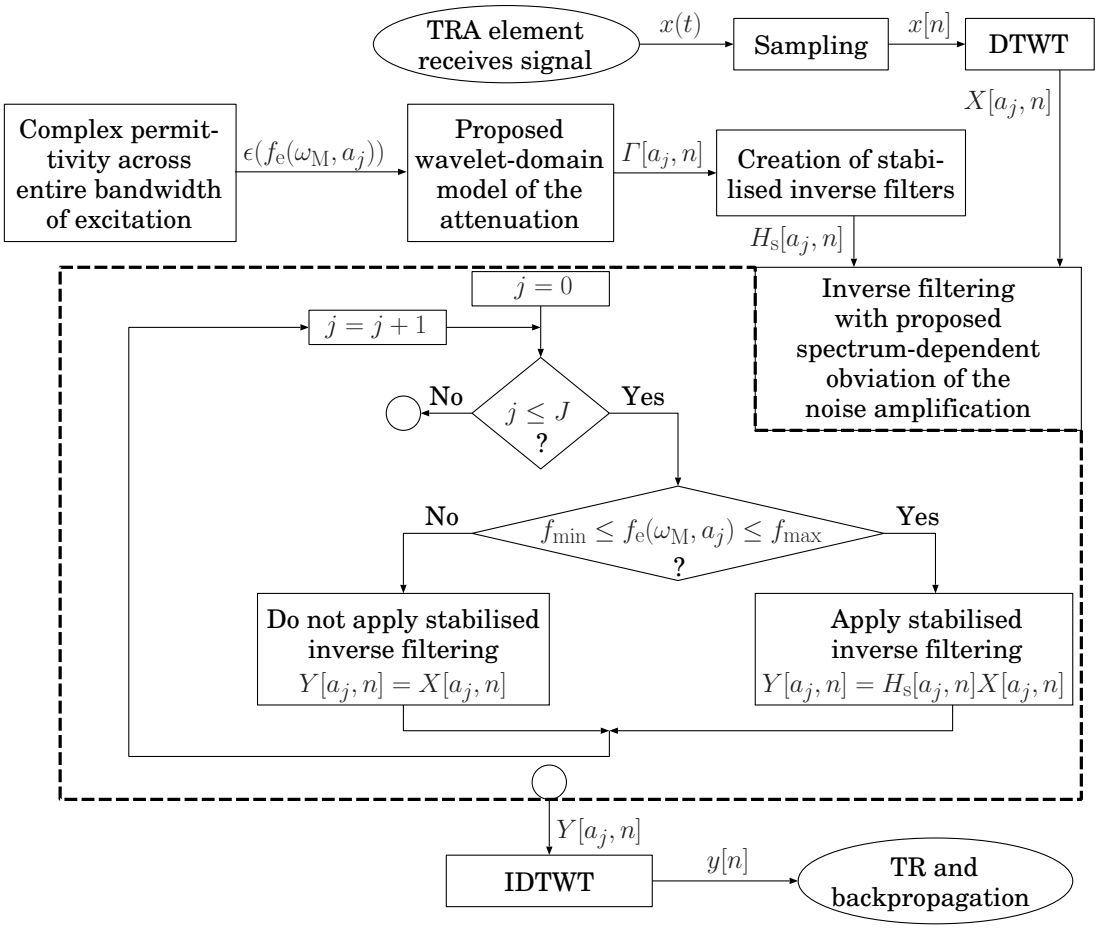

Figure 3.2: Block diagram of our proposed algorithm for the resolution enhancement of the UWB TR imaging in dispersive media.

3.2.2 Relating wavelet transform scales to Fourier frequencies

The scales of the wavelet transform are not *per se* related to frequencies analysed by the transform. Rather, wavelet scales define a stretch of the wavelet function in time domain. For cases where the mother wavelet contains dominant periodic components, an analytical relation can be found between each wavelet transform scale and one equivalent Fourier frequency. The complex Morlet mother wavelet is such a wavelet, since it is a complex sinusoid enveloped by a Gaussian distribution. In this section, we derive (3.32), which relates each wavelet transform scale factor to one equivalent Fourier frequency when the complex Morlet mother wavelet is used as the analysing wavelet, following the approach in [83] (which relates wavelet scale factors to equivalent Fourier wavelengths). The gist of this approach is that a monochromatic wave at a known frequency maximises the wavelet energy density at the scale associated to this frequency.

Let $f(t)$ be a complex sinusoid of known frequency $\omega_\mathrm{r} > 0$ and $\hat{f}(\omega)$ denote the Fourier transform of $f(t)$, then

$$\begin{aligned} f(t) &= e^{\jmath\omega_\mathrm{r} t} \\ \therefore \hat{f}(\omega) &= 2\pi\delta(\omega - \omega_\mathrm{r}) \end{aligned} \tag{3.42}$$

where $\delta(\ )$ is the Dirac delta function. The complex Morlet wavelet is expressed in frequency domain as

$$\hat{\psi_{\mathrm{M}0}}(\omega) = \pi^{1/4}\sqrt{2}e^{-\frac{1}{2}(\omega-\omega_\mathrm{M})^2}. \tag{3.43}$$

We take the CWT of $f(t)$ at scale factor a and with a translation in time of b temporal units:

$$T(a,b) = \frac{1}{\sqrt{a}}\int_{-\infty}^{\infty} f(t){\psi_{\mathrm{M}0}}^*\left(\frac{t-b}{a}\right)\mathrm{d}t. \tag{3.44}$$

We write the normalised scaled and translated wavelet function in a compact manner:

$$\psi_{\mathrm{M}0a,b}(t) = \frac{1}{\sqrt{a}}\psi_{\mathrm{M}0}\left(\frac{t-b}{a}\right). \tag{3.45}$$

Hence, (3.44) becomes

$$T(a,b) = \int_{-\infty}^{\infty} f(t)\psi_{\mathrm{M}0_{a,b}}^{*}(t)\,\mathrm{d}t. \tag{3.46}$$

By employing Parseval's identity on the inner product in (3.46) we get

$$T(a,b) = \int_{-\infty}^{\infty} \hat{f}(\omega)\hat{\psi_{\mathrm{M}0_{a,b}}}^{*}(\omega)\,\mathrm{d}\omega. \tag{3.47}$$

The Fourier transform of $\psi_{\mathrm{M}0_{a,b}}(\omega)$ is expressed as

$$\hat{\psi_{\mathrm{M}0_{a,b}}}(\omega) = \int_{-\infty}^{\infty} \frac{1}{\sqrt{a}}\psi_{\mathrm{M}0}\left(\frac{t-b}{a}\right)e^{-\jmath\omega t}\,\mathrm{d}t. \tag{3.48}$$

We simplify the integral in (3.48) with the substitution

$$t' \triangleq (t-b)/a \qquad \therefore \mathrm{d}t = a\,\mathrm{d}t' \tag{3.49}$$

and obtain

$$\hat{\psi_{\mathrm{M}0_{a,b}}}(\omega) = \int_{-\infty}^{\infty} \frac{1}{\sqrt{a}}\psi_{\mathrm{M}0}(t')e^{-\jmath\omega(at'+b)}a\,\mathrm{d}t' \tag{3.50}$$

$$= \sqrt{a}e^{-\jmath\omega b}\int_{-\infty}^{\infty} \psi_{\mathrm{M}0}(t')e^{-\jmath\omega at'}\,\mathrm{d}t'. \tag{3.51}$$

The integral in (3.51) is the Fourier transform of the wavelet at scaled frequency $a\omega$, therefore

$$\hat{\psi_{\mathrm{M}0_{a,b}}}(\omega) = \sqrt{a}\hat{\psi_{\mathrm{M}0}}(a\omega)e^{-\jmath(a\omega)t}. \tag{3.52}$$

Hence,

$$\hat{\psi_{\mathrm{M}0_{a,b}}}^{*}(\omega) = \sqrt{a}\hat{\psi_{\mathrm{M}0}}^{*}(a\omega)e^{\jmath(a\omega)t}. \tag{3.53}$$

We can thus expand (3.47) as

$$T(a,b) = \sqrt{a}\int_{-\infty}^{\infty} \hat{f}(\omega)\hat{\psi_{\mathrm{M}0}}^{*}(a\omega)e^{\jmath\omega b}\,\mathrm{d}\omega. \tag{3.54}$$

Substituting $\hat{f}(\omega)$ in (3.42) and $\hat{\psi_{\mathrm{M0}}}(a\omega)$ in (3.43) into (3.54), we obtain

$$T(a,b) = \sqrt{a}\int_{-\infty}^{\infty} 2\pi\delta(\omega-\omega_{\mathrm{r}})\pi^{1/4}\sqrt{2}e^{-\frac{1}{2}(a\omega-\omega_{\mathrm{M}})^2}e^{\jmath\omega b}\,\mathrm{d}\omega \tag{3.55}$$

$$= 2\pi\sqrt{a}e^{\jmath\omega_{\mathrm{r}}b}\left(\pi^{1/4}\sqrt{2}e^{-\frac{1}{2}(a\omega_{\mathrm{r}}-\omega_{\mathrm{M}})^2}\right) \tag{3.56}$$

$$= 2\pi\sqrt{a}e^{\jmath\omega_{\mathrm{r}}b}\hat{\psi_{\mathrm{M0}}}(a\omega_{\mathrm{r}}). \tag{3.57}$$

The wavelet energy density function (also called the *wavelet power spectrum* by some authors [83, 88]) is

$$|T(a,b)|^2 = 4\pi^2 a\left|\hat{\psi_{\mathrm{M0}}}(a\omega_{\mathrm{r}})\right|^2 \tag{3.58}$$

$$= 4\pi^2\pi^{1/2}2ae^{-(a\omega_{\mathrm{r}}-\omega_{\mathrm{M}})^2} \tag{3.59}$$

To derive the scale $a = a_{\mathrm{r}}$ where the wavelet energy density is maximised, we require

$$\left.\frac{\partial|T(a,b)|^2}{\partial a}\right|_{a=a_{\mathrm{r}}} = 0. \tag{3.60}$$

Therefore,

$$4\pi^2\pi^{1/2}2e^{-(a_{\mathrm{r}}\omega_{\mathrm{r}}-\omega_{\mathrm{M}})^2}\left(-2{\omega_{\mathrm{r}}}^2a_{\mathrm{r}}^2+2a_{\mathrm{r}}\omega_{\mathrm{r}}\omega_{\mathrm{M}}+1\right) = 0 \tag{3.61}$$

$$\therefore -2{\omega_{\mathrm{r}}}^2a_{\mathrm{r}}^2+2\omega_{\mathrm{r}}\omega_{\mathrm{M}}a_{\mathrm{r}}+1 = 0. \tag{3.62}$$

The accepted realistic root of the quadratic equation (3.62) is

$$a_{\mathrm{r}} = \frac{1}{2}\left[\frac{\omega_{\mathrm{M}}+\sqrt{2+{\omega_{\mathrm{M}}}^2}}{\omega_{\mathrm{r}}}\right] \tag{3.63}$$

because the rejected solution would suggest $a_{\mathrm{r}} < 0$. By setting $f_{\mathrm{e}}(\omega_{\mathrm{M}}, a) \triangleq \omega_{\mathrm{r}}/2\pi$ and $a \triangleq a_{\mathrm{r}}$ into (3.63) and rearranging, we obtain (3.32).

The function $\cos(\omega_{\mathrm{r}}t)$ can be used in place of $f(t)$ into (3.44) to derive (3.63), provided that the analysing wavelet is progressive. A wavelet ψ is *progressive* if and only if $\hat{\psi}(\omega) \cong 0$ for $\omega \leq 0$ [89, p. 130] [90]. The complex Morlet wavelet, as it is described in (3.43), is progressive for $\omega_{\mathrm{M}} \gg 1$.

3.3 Summary

This chapter introduced our proposed approaches for the through-the-wall imaging of multiple extended moving targets in UWB sensing settings and for the enhancement of resolution of UWB TR imaging in lossy and dispersive media.

For our approach for the TWRI of multiple extended moving targets, we apply both spatial and temporal windowing on a differential MDM for the detection of moving targets for the first time to our knowledge. We also proposed two novel imaging functionals: the TR-MUSIC-based FQ-MUSIC functional in (3.14), and the WF-MUSIC functional in (3.16). Moreover, we introduced a new process to determine the dimension of the signal subspace $\mathcal{N}_{l,m}^{\Theta} = \mathcal{N}_{l,m}^{\Theta\Sigma}$ of a sub-differential MDM with (3.11). Our proposed algorithm employs the spatiotemporal windowing of the differential MDM together with the FQ-MUSIC functional and $\mathcal{N}_{l,m}^{\Theta\Sigma}$ to extract radar images of moving targets from each spatiotemporal window. Finally, it uses the WF-MUSIC imaging functional to combine the target information from each spatiotemporal window and form the final radar image. A block diagram of our proposed approach is shown in Figure 3.1.

Our method for the enhancement of the resolution of UWB TR imaging in dispersive media corrects and improves the work in [1]. Our proposed algorithm takes into account the frequency-dependent complex permittivity of the propagation medium across the entire bandwidth of the radar interrogation pulse, for the first time to the author's knowledge. Using this complex permittivity, our method models the medium-, time-, and frequency- dependent attenuation in the wavelet domain in (3.34) that the interrogating pulse undergoes inside the medium. Our method uses this attenuation model to create stabilised inverse filters which compensate for the effects of the attenuation. Our work also introduces algorithm-driven automatic obviation of the noise amplification depending on the spectrum of the interrogating UWB pulse using (3.38), contrary to the empirical approaches in relevant prior work. A block diagram of our new method is illustrated in Figure 3.2.

Chapter 4

Simulation Settings

In Chapter 3, we proposed a novel approach for the radar imaging of multiple extended moving targets and a wavelet domain – based algorithm for the compensation of the effects of dispersive attenuation in TR microwave imaging methods. In this chapter, we prepare the simulation experiments which allow us to investigate the performance of the aforementioned methods.

4.1 Through-the-wall radar imaging of extended moving targets

In this section, we detail the simulation settings which we use with our TWRI approach.

4.1.1 Canonical test: Two targets overlapping in the downrange direction

The purpose of the experiments with this scenario is to highlight the merit of temporal windowing, in the case where two moving targets overlap in the range direction, i.e. when the line of sight between one target and some of the TRA elements is obstructed by another target, or, a moving obstruction closer to the TRA clutters the full-differential MDM and effectively hides another target further away from the TRA.

4.1.1.1 Geometry

This scenario consists of two moving targets in free space: a cylindrical wooden object (infinite cylinder), which is effectively hidden behind a rectangular timber board. The initial geometry for this scenario is illustrated in Figure 4.1. During the time interval $t_1 < t < t_2$, the wooden board moves by 2 mm away from the TRA, whereas the wooden cylinder moves by 2 mm towards the TRA.

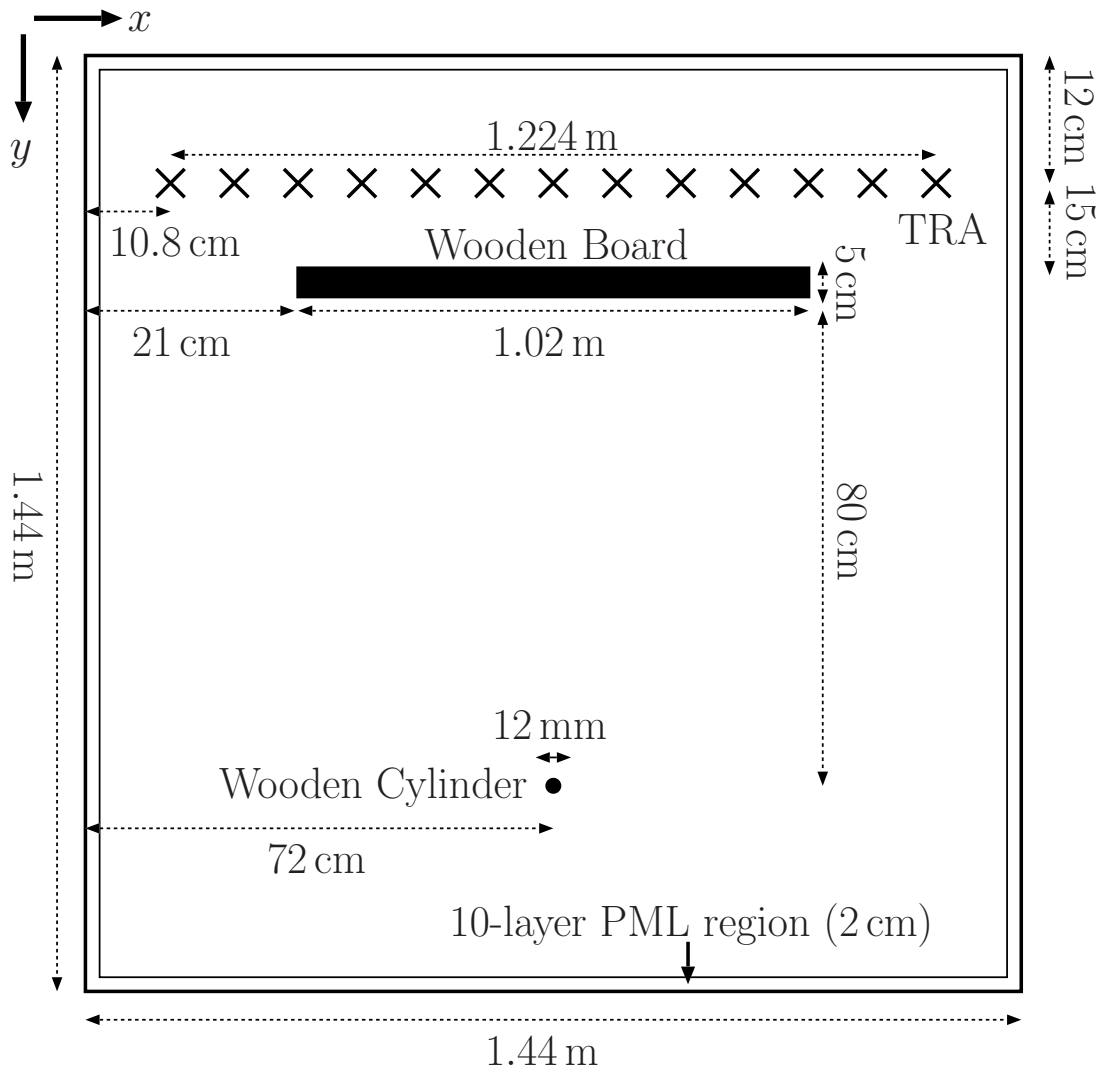

Figure 4.1: The initial configuration of the FDTD canonical case scenario for use with our TWRI approach with and without temporal windowing.

4.1.1.2 Setup of the window parameters and acquisition of results

We initially perform imaging using the WF-MUSIC imaging functional without applying spatial or temporal windowing. In this case, only one sub-differential MDM is formed; that is, $\boldsymbol{K}_{\mathbf{d}1,1}[n]$ which is identical to $\boldsymbol{K}_{\mathbf{d}}[n]$. The wooden board is physically larger and is placed closer to the TRA than the wooden cylinder. We thus expect that the contribution of the moving wooden board to $\boldsymbol{K}_{\mathbf{d}1,1}[n]$ predominates.

Next, we perform imaging using the WF-MUSIC imaging functional and also using temporal windowing, but without using spatial windowing. We apply temporal windowing with $P = 2000$. We choose this value of P because we simulate 3000 FDTD time steps. Hence, $P = 2000$ is large enough to contain the full excitation pulse and for $\boldsymbol{K}_{\mathbf{d}l,m}[n]$ to contain sufficient signal diversity to obtain reasonable imaging results. We expect that the temporal windowing of the differential MDM effectively isolates the differential signals due to the displacement of the two targets, i.e. the moving board and the moving cylindrical target.

For all our simulations in Section 4.1.1, we assume that the initial and final locations of the two wooden targets, their electrical properties, size, and shape are unknown. In this thesis, we do not consider effects due to finite dipole size or mutual coupling between the TRA elements, as we focus more on the development of the radar imaging algorithm.

4.1.2 Canonical test: Three targets overlapping in the cross-range direction

The purpose of this experiment is to emphasise the merit of spatial windowing in the case where multiple extended moving targets are arranged in the cross-range direction in the scene under radar interrogation.

4.1.2.1 Geometry

This scenario involves three moving wooden boards placed in parallel to the TRA in free space. We illustrate geometry of this scenario in Figure 4.2. During the time interval $t_1 < t < t_2$ all wooden boards move closer to the TRA by 2 mm in the range direction.

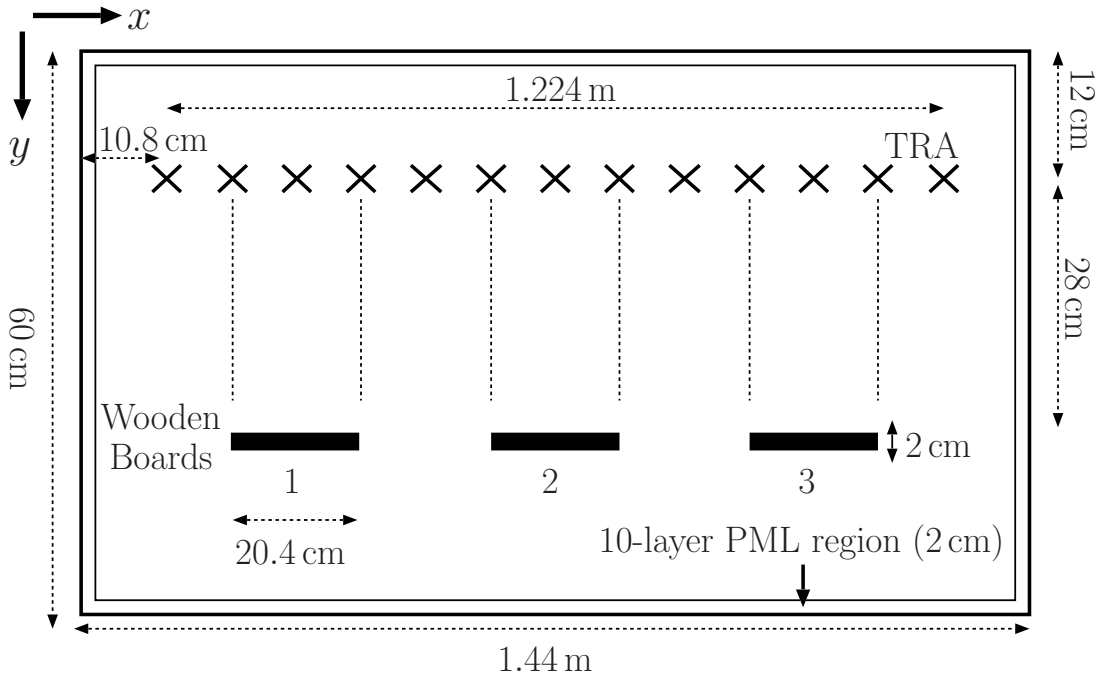

Figure 4.2: The initial configuration of the FDTD canonical case scenario for use with our TWRI approach with and without spatial windowing.

4.1.2.2 Setup of the window parameters and acquisition of results

Initially, we carry out radar imaging using our approach without segregating the signals in $\boldsymbol{K}_{\mathbf{d}}$ into temporal or spatial windows. In this case, we expect that the differential signal due to the displacement of wooden board 2 dominates the signal subspace content of $\boldsymbol{K}_{\mathbf{d}1,1}[n]$, since wooden board 2 is closest to the centre of the TRA. We therefore expect that the imaging of moving targets 1 and 3 is impaired. As wooden boards 1 and 3 are not significantly further away from the TRA elements relative to each other, we expect that their contributions in $\boldsymbol{K}_{\mathbf{d}1,1}[n]$ have similar strength. Because of this together with the expectation for a dominant signal contribution from board 2, we expect that targets 1 and 3 are detected weakly and appear faint in the final radar image.

Next, we apply spatial windowing on the same scenario with $\mathcal{N}_{\text{sw}} = 9$. We do not apply temporal windowing. Thus, five spatial windows are formed. We choose this value for $\mathcal{N}_{\text{sw}}$ because the separation distance between 9 adjacent TRA antennas is larger than the spatial span of two targets in the cross-range direction but smaller than the span of three targets. Hence, we expect that $\mathcal{N}_{\text{sw}} = 9$ virtually divides the returns from the three targets into the returns of two

targets, which form a signal subspace and that this allows for $13-9=4$ singular vectors for the noise subspace of each sub-differential MDM to be formed. For example, we expect that $\boldsymbol{K}_{\mathbf{d}5}[n]$ contains strong differential signal contributions from both wooden boards 2 and 3. This is because the time for the differential signals created by the movement of wooden board 3 to reach the i-th TRA element employed by the fifth spatial window, with $1 \leq i \leq \mathcal{N}_{\text{sw}} = 9$, is theoretically equal to the time for the differential signals created by the movement of wooden board 2 to reach the $(\mathcal{N}_{\text{sw}} - i + 1) = (9 - i + 1)$-th element employed by the same spatial window. Similarly, we expect that $\boldsymbol{K}_{\mathbf{d}1}[n]$ contains strong differential signal contributions from wooden boards 1 and 2. Hence, we anticipate that $\tilde{\mathcal{M}}_{1,1}$ and $\tilde{\mathcal{M}}_{5,1}$ achieves imaging of moving wooden boards 1 and 2, and 2 and 3 respectively.

4.1.3 Practical case scenario

Here, we consider a practical scenario. This scenario involves five human targets who move behind a brick wall and overlap in both cross-range and range directions. The aim of the practical case experiments is to detect all five human subjects.

4.1.3.1 Geometry

We illustrate the initial simulation setup for this scenario in Figure 4.3. Between successive radar interrogations, targets 1–4 move by 2 mm, whereas target 5 moves by $2\sqrt{5}$ mm at an angle of 26.57° from the downrange direction. The brick wall has a thickness of 30 cm to resemble a typical brick wall [91]. We place the TRA on the outer surface of the brick wall, with no standoff distance. Targets 1–4 are placed close to the brick wall. Target 5 is located behind targets 1–4. Each human target is modelled as an ellipse made of fat tissue with a 2 mm thick circumferential layer of skin. Each ellipse has a major axis length of 30 cm and a minor axis length of 20 cm.

4.1.3.2 Setup of the window parameters and acquisition of results

We apply spatial and temporal windowing to the full-differential MDM, with $P = 1500$ time steps and $\mathcal{N}_{\text{sw}} = 9$. We perform radar imaging using the WF-MUSIC method. We investigate the effects of setting $\mathcal{N}_{l,m}^{\Theta\Sigma}(f)$, $\mathcal{N}_{l,m}^{\Theta 10\%}(f)$, and $\mathcal{N}_{l,m}^{\Theta\div}(f)$

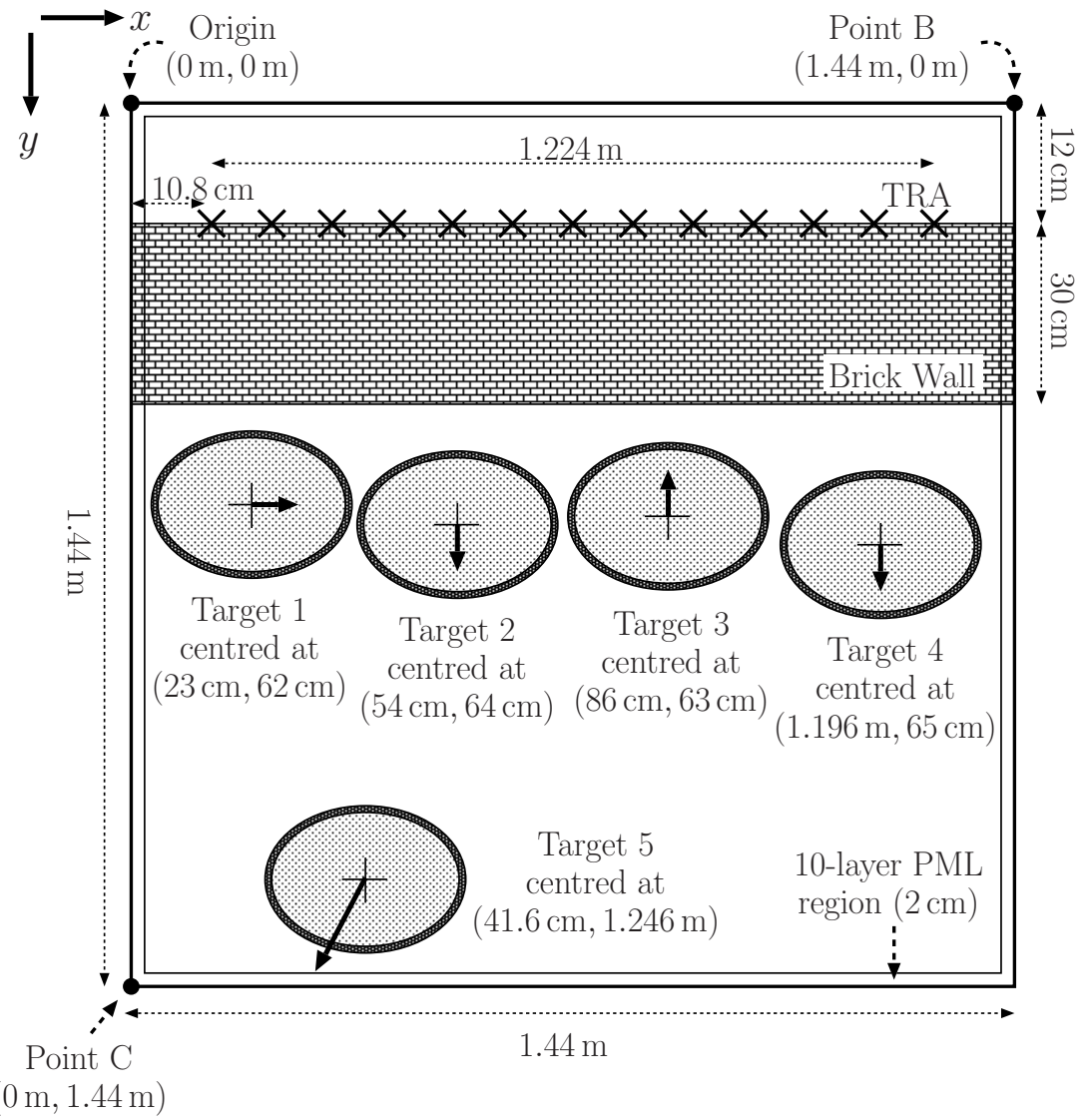

Figure 4.3: The initial geometry of our practical case scenario simulation. The solid black arrows indicate the direction and amount of displacement (not to scale) of each target between successive radar interrogations.

as the values of $\mathcal{N}^{\Theta}_{l,m}(f)$ together with the WF-MUSIC method. Furthermore, we apply to this scenario the spatiotemporally windowed UWB-MUSIC approach proposed in [4] by utilising $\boldsymbol{K}_{\mathbf{d}}[n]$ instead of $\boldsymbol{K}[n]$ in [4], keeping the rest of the simulation setting. For the UWB-MUSIC approach, we employ the same spatial and temporal window parameters, that is, $P = 1500$ time steps and $\mathcal{N}_{\text{sw}} = 9$. The values for P and $\mathcal{N}_{\text{sw}}$ are chosen empirically. We choose P so that it is smaller than the experiments in Section 4.1.1, as the targets in this scenario have smaller separation, but it is large enough to contain sufficient signal diversity. Given a TRA with 13 elements, we expect that $\mathcal{N}_{\text{sw}} = 9$ signal subspace vectors and 4 null subspace vectors should yield adequate spatial windowing.

We assume no knowledge on the location, size or electrical properties of the targets and walls. We assume that we have knowledge of the thickness of the wall. Hence, we perform imaging only on the space where targets can exist.

4.1.4 Radio parameters

All simulations in Section 4.1 employ the same radio setup, which is described in Section 4.1.4. Since all the experiments in this thesis consider propagation of UWB signals, we employ a time-domain solver for all our simulations. For all the experiments in this thesis, we use the $(\text{FD})^2\text{TD}$ method [30], as it is a time-domain method and can also simulate propagation in dispersive media such as human tissues without significant computation overhead [30]. The $(\text{FD})^2\text{TD}$ software used in this thesis is made in-house by our research group at the University of Manchester. Its validity been tested against commercial FDTD software, such as XFdtd by Remcon and has been found to agree well [92, p. 52].

A 2D, 720 cells × 720 cells $(\text{FD})^2\text{TD}$ space is used for each simulation in Section 4.1. The $(\text{FD})^2\text{TD}$ space is uniformly sampled with a spatial step of $\Delta h \triangleq \Delta x = \Delta y = 2\,\text{mm}$. The $(\text{FD})^2\text{TD}$ temporal step is set as $\Delta t = 3.849$ ps. The CFS-PML absorbing boundary conditions [31] are used with a 10-cell layer. The CFS-PML size was decided in consultation with members of our research group and the supervising team.

We transmit a first derivative of a Gaussian pulse, with a centre frequency of $f_{\text{c}} = 1.44$ GHz from $\mathcal{N} = 13$ equidistant TRA elements, with only one element illuminating the scene at a time. The excitation pulse covers a frequency range of interest of $f_{\min} < f < f_{\max}$ with $f_{\min} = 150\,\text{MHz}$ and $f_{\max} = 4\,\text{GHz}$. Frequencies $f_{\min}$, f_{c}, and $f_{\max}$ satisfy $\tilde{\hat{S}}(f_{\min}) = \tilde{\hat{S}}(f_{\max}) = 0.1 \cdot \tilde{\hat{S}}(f_{\text{c}}) = 0.1$, where $\tilde{\hat{S}}$ is

the normalised frequency spectrum of the excitation pulse. We illustrate the excitation pulse in time domain in Figure 4.4 and the spectrum it covers in Figure 4.5. In our experiments, we do not model transmitting or receiving antennas. Instead, we employ FDTD soft sources [93] (line sources) as the transmitting elements and FDTD observation points in place of receiving antennas, as this thesis is more focused on the development of the radar imaging algorithm. The use of FDTD soft sources (rather than hard sources) ensures that no extra scattering occurs due to the modelling of the excitation sources and signals pass through the soft sources without any disruption of the wave propagation. This allows the observation of only the original source signal and any signals scattered from the scenario's original geometry.

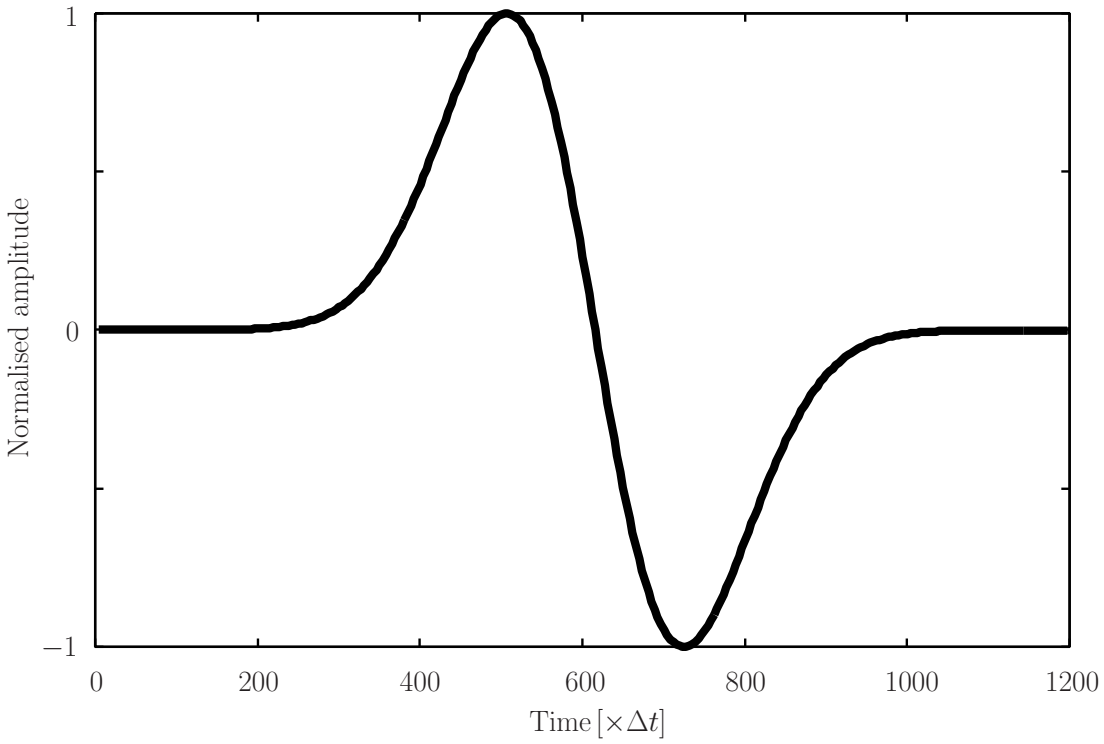

Figure 4.4: The normalised amplitude of the excitation pulse.

4.1.5 Constitutive parameters of the propagation media

For all our simulations in Section 4.1, we assume that all propagation media are linear, homogeneous, isotropic, and non-magnetic, i.e. it holds $\mu_{\mathrm{r}} = 1$ for all media. In our numerical experiments, all wooden objects (timber boards, wooden cylinder) are simulated as frequency-independent dielectric objects made of the

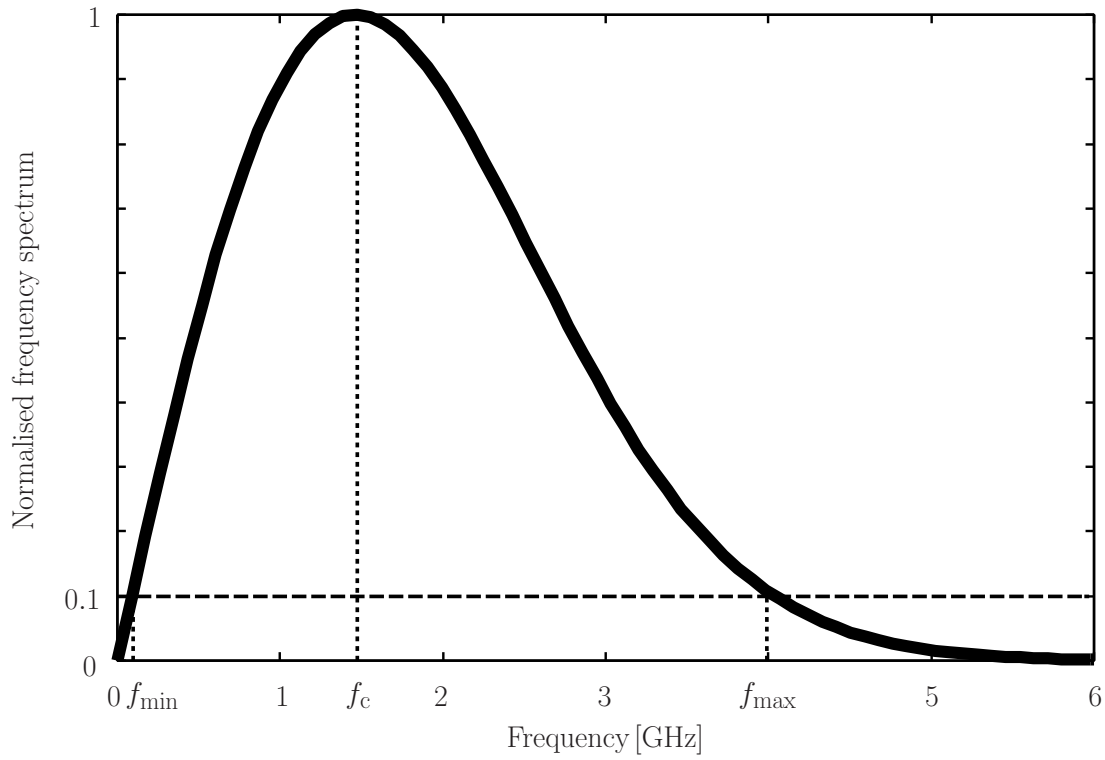

Figure 4.5: The normalised frequency spectrum of the excitation pulse.

same wood material. We set the relative permittivity of wood as ${\epsilon_r}^{\text{wood}} = 3$ and the conductivity of wood as $\sigma_s^{\text{wood}} = 0.003$ S/m [94]. The relative permittivity and conductivity of the brick material we model to simulate a brick wall are respectively ${\epsilon_r}^{\text{brick}} = 3.8$ and $\sigma_s^{\text{brick}} = 0.02$ S/m [4], which we also assume to be effectively frequency-independent. We use the one-pole Debye relaxation model for the skin and fat tissues. We list the Debye parameters for the human tissues [95] in Table 4.1.

Table 4.1: Debye parameters of human tissues

Propagation medium	σ_s [S/m]	ϵ_s	ϵ_∞	τ_D [ps]
Fat	0.037	5.531	3.998	0.236
Skin	0.541	47.930	29.851	0.436

4.2 Resolution enhancement of TR imaging in dispersive media

In this section, we detail the setup of the simulation experiments we perform with our approach on the for the resolution enhancement of TR imaging in dispersive media.

4.2.1 Canonical case scenario

We apply our proposed resolution enhancement method to a scenario which contains a single homogeneous dispersive propagation medium and a PEC scatterer of circular disc shape. The aim of the canonical case simulation is to assess the improvement in resolution of the TR refocusing without multipaths that may improve the resolution of the TR imaging [1, 96]. We assume knowledge of the dielectric characteristics of the background medium. However, we assume no knowledge of the target's characteristics, or the target's exact location.

4.2.1.1 Geometry

The geometry for the canonical case scenario for use with our dispersive method is illustrated in Figure 4.6. We simulate dispersive muscle tissue [95] as the propagation medium. The PEC scatterer has a diameter of 5 mm.

4.2.1.2 Radio environment setting

A 2D, 226 cells × 185 cells, TM_z polarised $(\mathrm{FD})^2\mathrm{TD}$ space is used for this simulation. The $(\mathrm{FD})^2\mathrm{TD}$ space is uniformly sampled with a spatial step of $\Delta h \triangleq \Delta x = \Delta y = 1\,\mathrm{mm}$. The temporal step Δt for the $(\mathrm{FD})^2\mathrm{TD}$ simulation is set to 1.9245 ps. For our simulations, we take $T_\mathrm{s} \equiv \Delta t$. The CFS-PML absorbing boundary conditions [31] are used with a 32-cell layer. The CFS-PML size was decided in consultation with members of our research group and the supervising team. The entire $(\mathrm{FD})^2\mathrm{TD}$ space is set up as homogeneous dispersive muscle tissue [95] as the propagation medium.

We place fifteen equidistant TRA elements parallel to the x-axis. The interrogating TRA element is at grid location $(x, y) = (92, 121)$ The interrogating TRA element is excited with a first derivative of a Gaussian pulse which has a centre frequency f_c of 3 GHz. The excitation pulse is shown in Figure

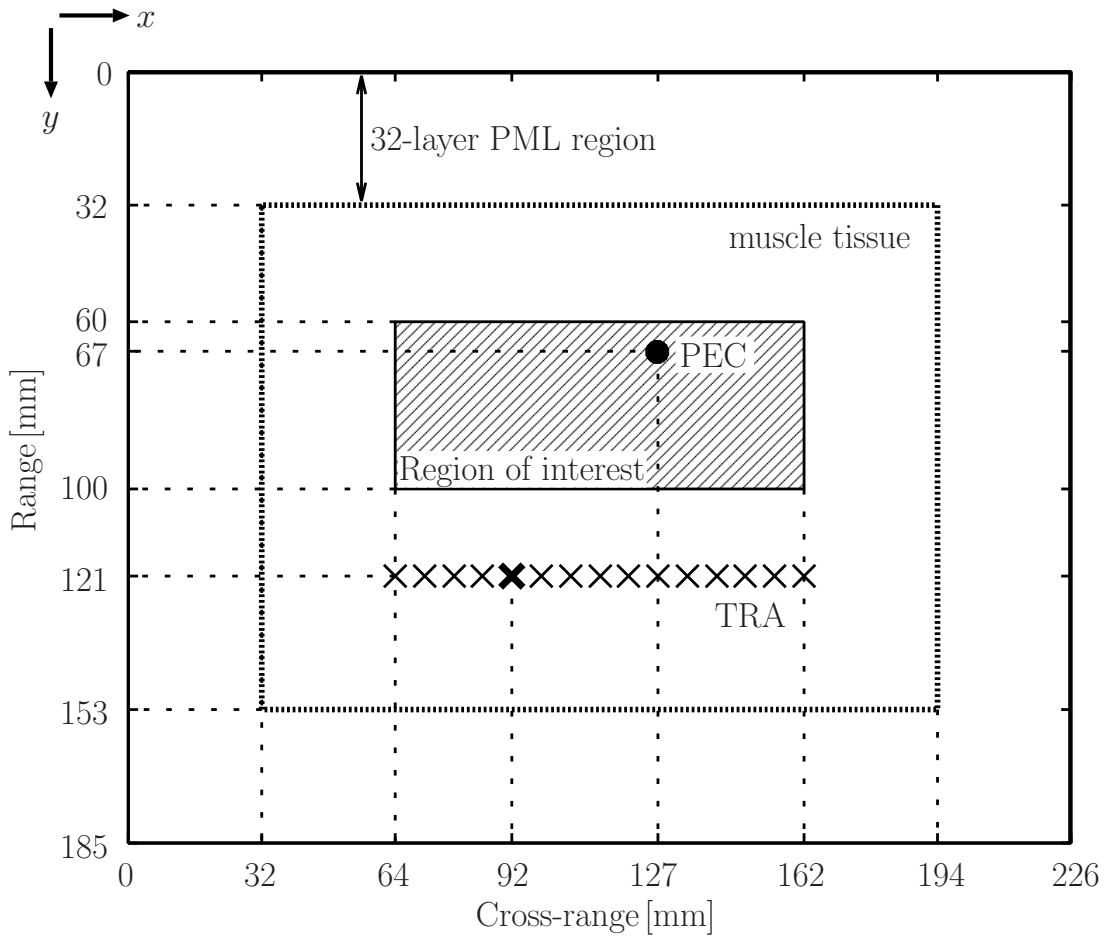

Figure 4.6: The geometry of the canonical case FDTD scenario for use with our TR resolution enhancement approach. The boldface '×' denotes the interrogating TRA element.

4.7. The excitation pulse covers a frequency range of $f_{\min} \leq f \leq f_{\max}$ with $f_{\min} = 700\,\text{MHz}$ and $f_{\max} = 6.2\,\text{GHz}$. Frequencies $f_{\min}, f_{\max}$ satisfy $\tilde{\hat{S}}(f_{\min}) = \tilde{\hat{S}}(f_{\max}) = e^{-1} \cdot \tilde{\hat{S}}(f_c) = e^{-1}$ where $\tilde{\hat{S}}(f)$ is the normalised frequency spectrum of the excitation signal [71,93]. The spectrum $S(f)$ used throughout the simulations of Section 4.2 is illustrated in Figure 4.8.

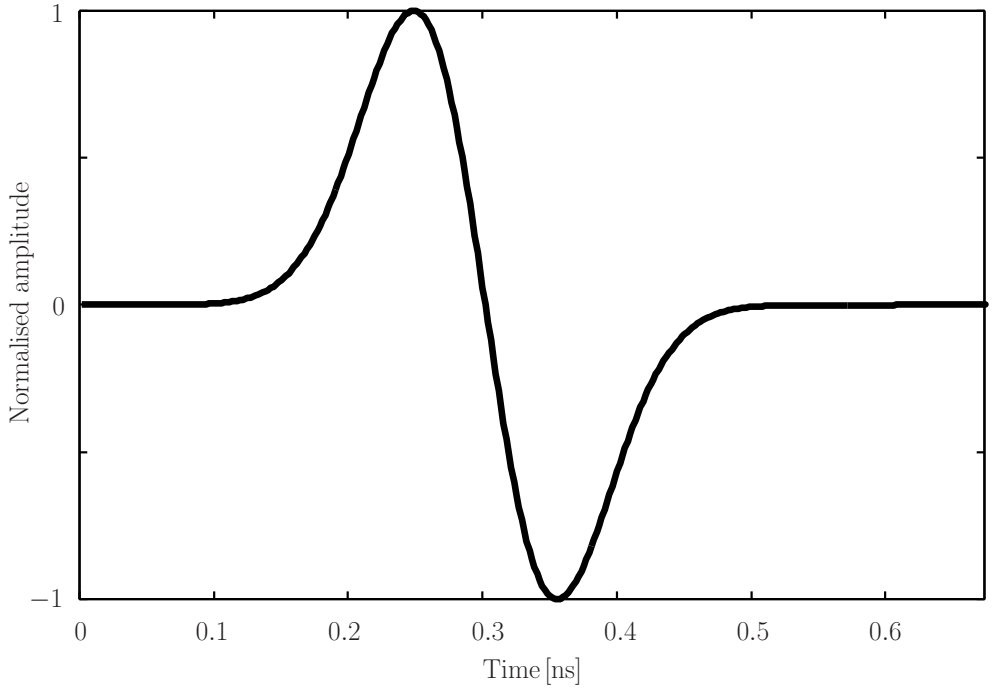

Figure 4.7: The normalised amplitude of the excitation pulse.

For the initial illumination of the scenario, we use a FDTD soft source [93] at the location of the interrogating TRA element. During the initial illumination of the scene and TR forward propagation, we observe E_z at each TRA element. The use of FDTD soft source during forward propagation ensures that signals pass through the soft source FDTD cell without any disruption of the wave propagation. Hence, the rest of the receiving elements of the TRA sense only the signals scattered from the scenario and there are no reflections originating at the FDTD cell containing the excitation source. We simulate a SNR of 70 dB by applying Additive White Gaussian Noise (AWGN) to $x[n]$ received at each TRA element. FDTD soft source excitation in the $(\text{FD})^2\text{TD}$ method is performed on the $\boldsymbol{D}$ field [93]. In our experiments, we use the recorded and time-reversed $\boldsymbol{E}$ field signals for the TR backpropagation, but we cannot directly excite the $\boldsymbol{E}$ field in

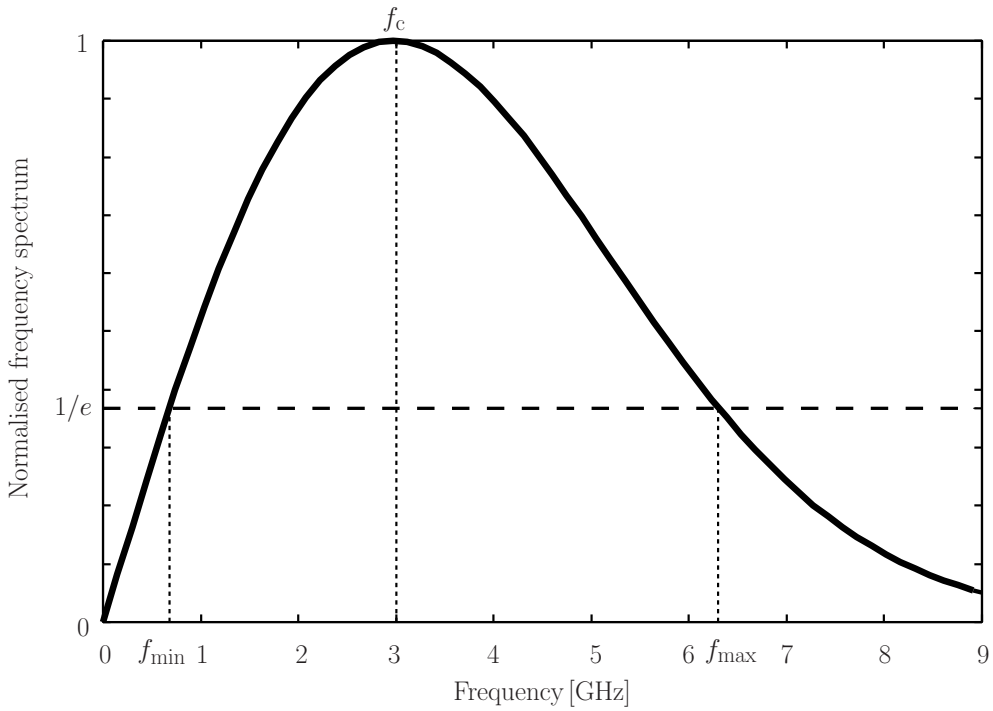

Figure 4.8: The normalised frequency spectrum of the excitation pulse.

the $(FD)^2TD$ algorithm using soft sources for the backpropagation stage. Therefore, in our experiments, FDTD hard sources assume the role of the transmitting TRA elements during the TR backpropagation process. Each hard source acts as a line PEC scatterer [93]. Hence, signals are scattered when they hit hard sources since they act as metal lines. For our experiments, we assume that any scattering caused by the TRA hard source elements during backpropagation does not affect the quality of the refocusing. Besides, such scattering is not part of the original path of the forward-propagating pulses. Hence, during backpropagation, waves which are scattered due to the presence of FDTD hard sources do not follow the same path the forward-propagating pulses travelled and, therefore, do not re-focus on the target scatterer. Thus, we expect that the TR refocusing is not affected. In our simulations, we do not take into account effects due to finite dipole size or mutual coupling between the TRA elements, as this thesis focuses more on the development of the resolution enhancement algorithm.

4.2.1.3 Setting of the parameters of the inverse filters

For both our approach and the approach in [1], we use the frequency-dependent muscle tissue as the dominant propagation medium for the inverse filters. For

the mother wavelet for the DTWT, we set $\omega_{\mathrm{M}} = 6$ for the reasons discussed in Section 3.2 and also to employ the same analysing wavelet as [1]. For the DTWT, we set $\Delta_a = 0.025$ following [1]. We set a_0 so that the equivalent Fourier period is $2T_{\mathrm{s}}$ [80]. We achieve this condition by setting $f_{\mathrm{e}} \triangleq 1/(2T_{\mathrm{s}})$ and $a_j \triangleq a_0$ into (3.32) as in

$$\begin{aligned} \frac{1}{2T_{\mathrm{s}}} &= \frac{\omega_{\mathrm{M}} + \sqrt{2 + {\omega_{\mathrm{M}}}^2}}{4\pi a_0} \\ \therefore \quad a_0 &= 2T_{\mathrm{s}} \frac{\omega_{\mathrm{M}} + \sqrt{2 + {\omega_{\mathrm{M}}}^2}}{4\pi} \\ &\approx 3.726 \times 10^{-12} \text{ s.} \end{aligned} \tag{4.1}$$

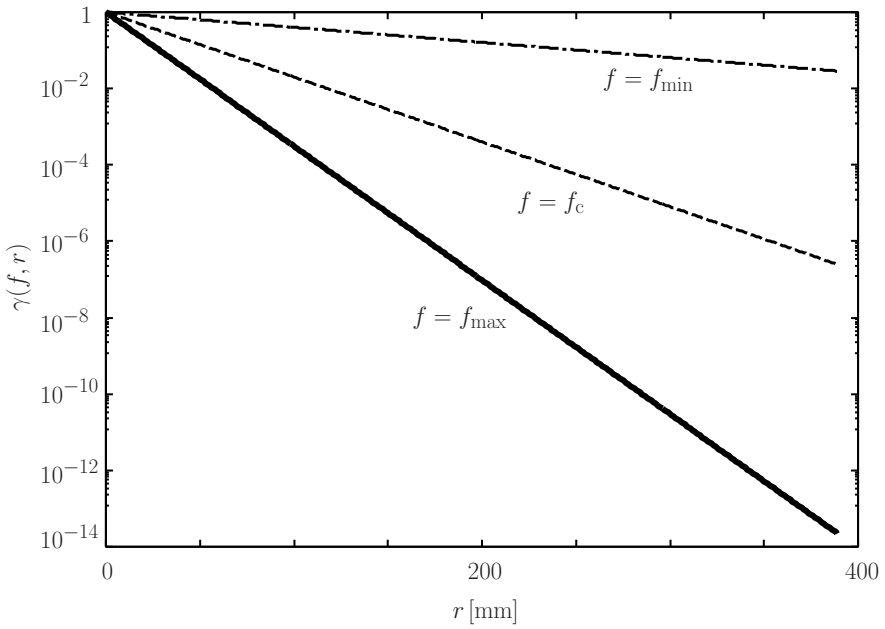

Figure 4.9: Theoretical calculation of $\gamma(f, r)$ in homogeneous muscle tissue.

We set the parameter s for the inverse filters empirically. We assign a value for s such that s^2 is not smaller than $\Gamma^2[f_{\mathrm{e}}, n]$ in (3.37), and hence $\gamma^2(f, t)$ for the interrogation pulse of interest at propagation distances of interest. We use (3.29) to plot in Figure 4.9 $\gamma(f_{\mathrm{min}}, r)$, $\gamma(f_{\mathrm{c}}, r)$, and $\gamma(f_{\mathrm{max}}, r)$ for propagation distance r inside the scenario's background medium (homogeneous and isotropic muscle tissue). We calculate the round-trip propagation distance from the interrogating TRA element at $(x, y) = (92, 121)$ to the farthest edge of the region of interest

at $(x, y) = (162, 60)$ (see Figure 4.6) as in $r = 2 \times \sqrt{(162-92)^2 + (60-121)^2} \approx 186\,\text{mm}$. The round-trip time for this distance in muscle tissue is $t = \frac{0.186\,\text{m}}{c^{\text{muscle}}}$, where c^{muscle} is the speed of light in the the muscle tissue. Hence, the frequency $f_{\max}$ propagating in the background medium undergoes attenuation of approximately $\gamma(f_{\max}, t = \frac{0.186\,\text{m}}{c^{\text{muscle}}}) \approx 10^{-8}$. We choose a value for s such that $s^2 \geq (10^{-8})^2$. We set $s = 10^{-7}$.

4.2.1.4 Acquisition of results

We perform the TR experiment using no filter (unfiltered, conventional TR approach), using our proposed approach, and using the method in [1]. For each case, we transmit the time-reversed perturbed electric fields from the TRA during the TR backpropagation. The use of the time-reversed perturbed fields constitutes the standard practice in TR radar imaging [9, 97]. The *perturbed* electric field is obtained by subtracting the forward scattered signal sensed from the scenario geometry when the target object is absent, from the forward scattered signal sensed using the same geometry but with the target present. These signals can be obtained either experimentally or they can be approximated numerically. In this work, we perform numerical simulations to obtain the perturbed electric field at each TRA element, which we assign as $x[n]$. (Some authors call the field signal obtained with a target present the *perturbed field*, whereas they call the difference of the returned fields with and without the target present the *scattered field* [98]. This thesis does not follow this nomenclature.)

To objectively decide the time of refocus, and therefore perform a fair comparison of the refocusing achieved by these approaches, we use the minimum entropy criterion on the backpropagated E_z field of the unfiltered TR experiment [9], since the values of E_z are available everywhere and for every time step during TR backpropagation. Both inverse filtering algorithms are independent of both the region of interest and the time of refocusing. We employ the inverse varimax norm of the backpropagated E_z field, $\Xi[E_z^n]$, as measure of entropy [12], with

$$\Xi[E_z^n] = \frac{\left[\sum_y \sum_x E_z^{n2}[x, y]\right]^2}{\sum_y \sum_x E_z^{n4}[x, y]}. \tag{4.2}$$

We compute $\Xi[E_z^n]$ inside the region of interest, away from the TRA elements, to

eliminate the effect the transmitting TRA elements have on the minimum entropy selection process during backpropagation. To the best of the author's knowledge, this is the first time that the minimum entropy criterion is integrated to TR imaging experiments for the investigation of dispersion compensation techniques.

We quantify the spatial resolution in the E_z field achieved by each method. We expect that our proposed approach presents the best resolution of the TR refocusing. We also compare the refocusing resolution achieved using our approach against the refocusing resolution obtained using the conventional TR approach on a scenario with identical geometry and radio environment to Section 4.2.1.1 but using a reference lossless medium [16], instead of the dispersive muscle tissue as the background. The constitutive parameters for the reference lossless medium are detailed in Section 4.2.3. For the case of the reference lossless background medium, we decide the time of refocus by applying the minimum entropy criterion on the backpropagated E_z field of the unfiltered TR experiment with the lossless medium, since the propagation times of electromagnetic waves are not the same in the different propagation media.

4.2.2 Practical case scenario

Brain tumours is one of the deadliest of all forms of cancer [99, 100]. Microwave imaging of the brain is challenging because of complex layered tissues inside the head [101], which attenuate electromagnetic waves propagating through them. We apply the TR imaging technique with our proposed TR resolution enhancement method to locate a brain tumour in a DHP. The purpose of this numerical simulation is to evaluate the improvement in refocusing resolution of the TR imaging, at the time of refocus, by using our resolution enhancement method on a practical case scenario which involves propagation through multiple dispersive human tissues.

The DHP was provided by the RIKEN research institution (in Saitama, Japan) under nondisclosure agreement between RIKEN and The University of Manchester. The usage was approved by the RIKEN ethical committee. The DHP has 1 mm resolution and contains 52 segmented tissues. Our research group fitted the one-pole Debye parameters of human tissues [102] using the measurement provided in [103] and [104]. The Debye media parameters for human tissues can be found in [95] and are presented in Section 4.2.3 for completeness.

4.2.2.1 Geometry of the 2D experiments

We carry out 2D experiments utilising a horizontal cross-section of the head of the DHP. Figure 4.10 illustrates the simulation setup. A 2D, 322 cells × 295 cells TM_z polarised $(\mathrm{FD})^2\mathrm{TD}$ space was used for this simulation, which includes a 32-cell CFS-PML layer. The CFS-PML size was decided in consultation with members of our research group and the supervising team. The $(\mathrm{FD})^2\mathrm{TD}$ spatial step is set to $\Delta h \triangleq \Delta x = \Delta y = 1\,\mathrm{mm}$. The temporal step Δt for the $(\mathrm{FD})^2\mathrm{TD}$ simulation is set to 1.9245 ps. For our simulations, we take $T_\mathrm{s} \equiv \Delta t$. The interrogating TRA element, which illuminates the scene before the TR forward propagation step, is at location $(x, y) = (177, 67)$ where (x, y) are the FDTD grid cell coordinates in the cross-range and range directions respectively. We simulate the cross-section surface of the tumour as a disc with a diameter of 7 mm centred at $(x, y) = (170, 112)$ on the white matter as in Figure 4.10.

4.2.2.2 Radio environment setting in the 2D experiments

We place 55 TRA elements (line sources) on the skin of the DHP as in Figure 4.10. The interrogating TRA element transmits a first derivative of a Gaussian pulse as in Section 4.2.1. We simulate AWGN on the received perturbation signals so that the SNR is 70 dB. We decide on the time of refocus using the minimum entropy criterion on the backpropagated E_z field of the unfiltered TR experiment with (4.2) as in Section 4.2.1. The rest of the radio environment settings are identical to Section 4.2.1.

4.2.2.3 Geometry of the 3D experiments

We carry out 3D experiments using the head of the DHP. Figure 4.11 illustrates the simulation setup. A 3D, 321 cells × 297 cells × 160 cells $(\mathrm{FD})^2\mathrm{TD}$ space was used for the 3D simulations. The CFS-PML absorbing boundary conditions are used with a 32-cell layer. The FDTD space is uniformly sampled with a spatial step of $\Delta h \triangleq \Delta x = \Delta y = \Delta z = 1\,\mathrm{mm}$. The temporal step Δt for the $(\mathrm{FD})^2\mathrm{TD}$ simulation is set to 1.9245 ps. For our simulations, we take $T_\mathrm{s} \equiv \Delta t$. We simulate the brain tumour as a sphere with a diameter of 7 mm centred at FDTD cell coordinates $(x, y, z) = (172, 117, 108)$ on the white mater (right hemisphere) as in Figure 4.11.

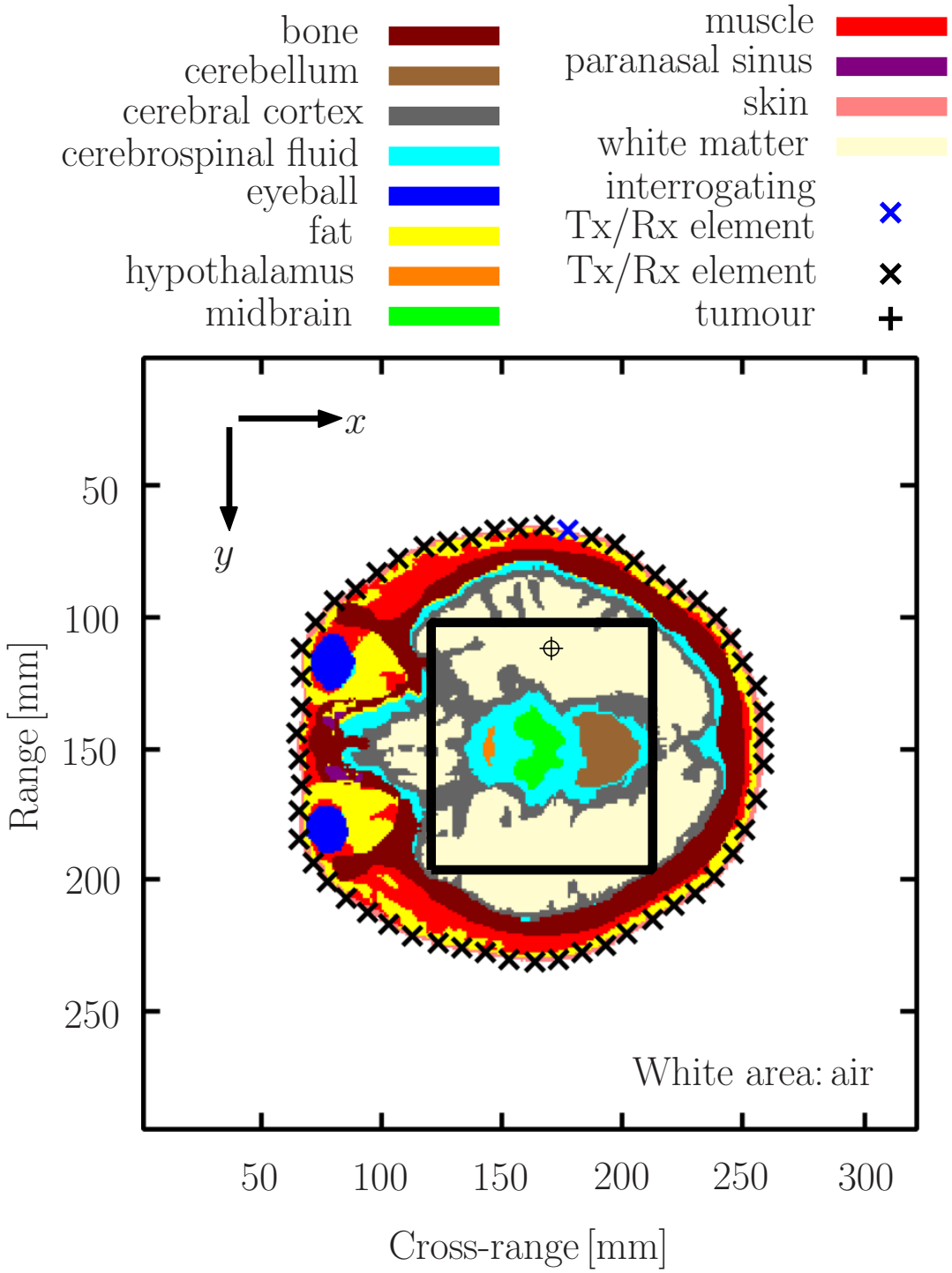

Figure 4.10: The geometry of the 2D practical case FDTD scenario. The black rectangle indicates the region of interest.

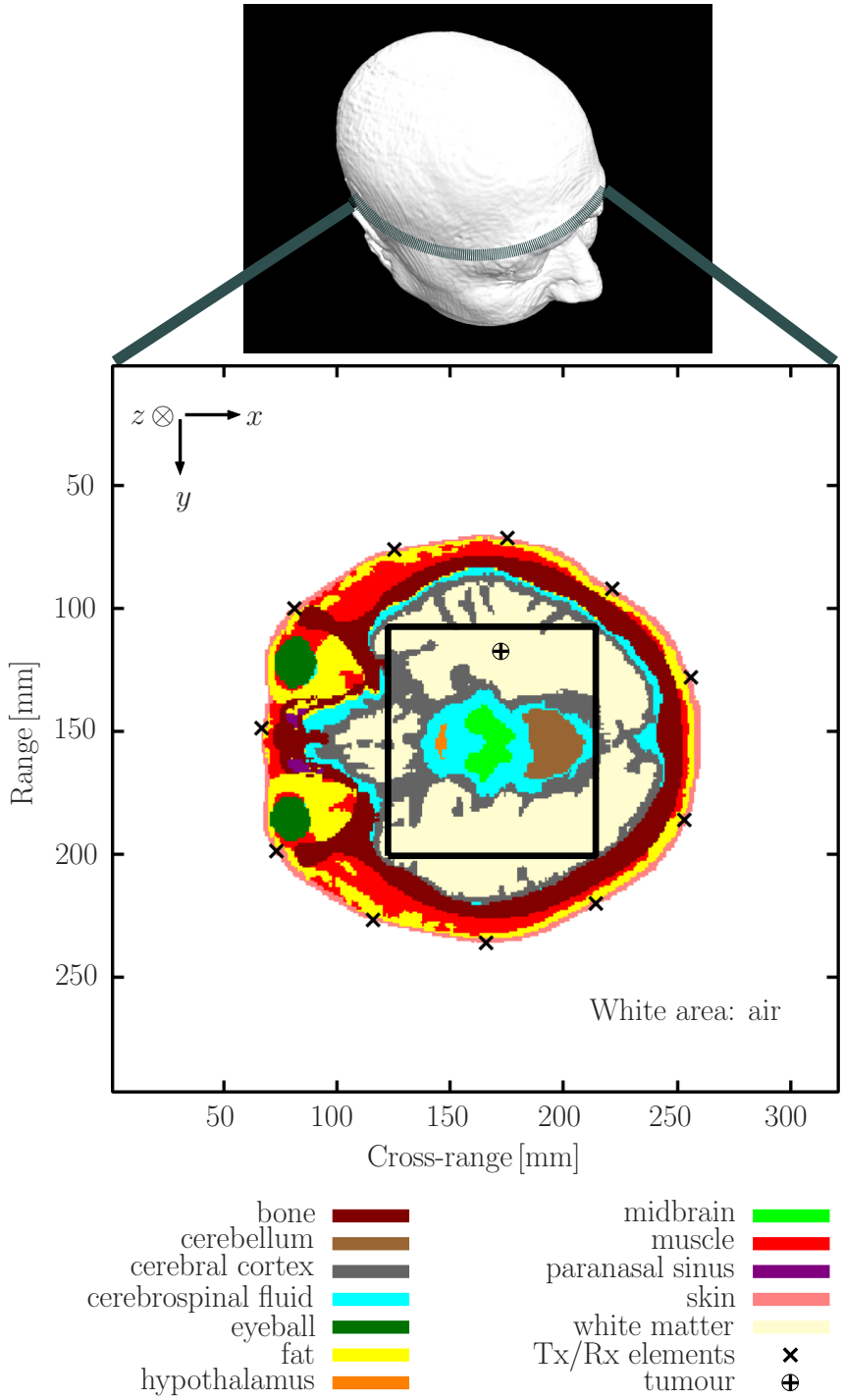

Figure 4.11: The geometry of the 3D practical case FDTD scenario. The black rectangle indicates the region of interest.

4.2.2.4 Radio environment setting in the 3D experiments

We place 11 TRA elements on the skin of the DHP as in Figure 4.11. The interrogating TRA element is located at grid cell coordinates $(x, y, z) = (175, 71, 108)$. It is excited with a first derivative of a Gaussian pulse as in Section 4.2.1. We simulate AWGN on the received perturbation signals so that the SNR is 45 dB. The rest of the radio environment settings are identical to Section 4.2.1.

4.2.2.5 Setting of the parameters of the inverse filters

First, we identify the medium which covers the biggest part of the propagation area inside the cross-section of the head of the healthy DHP. Figure 4.12 shows the

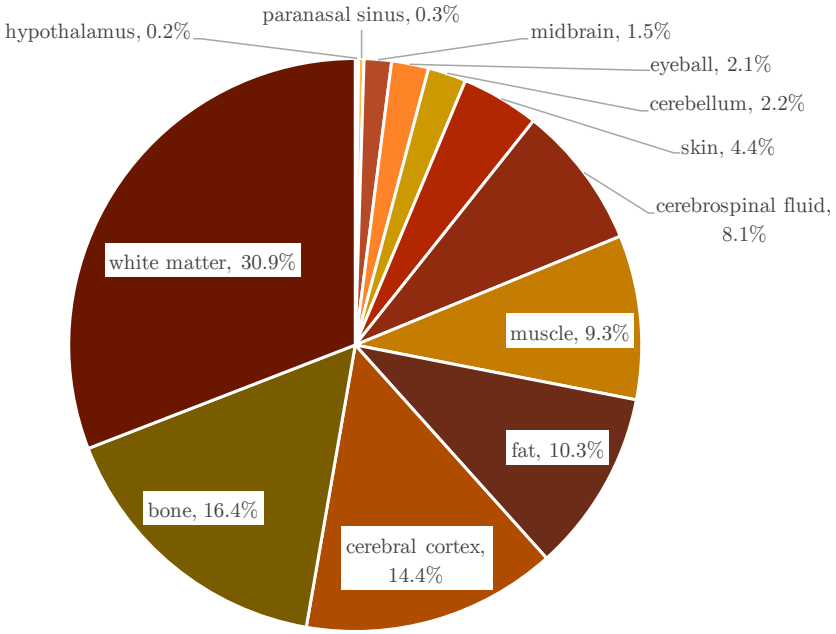

Figure 4.12: Percentage of area covered by each propagation medium in the horizontal cross-section of the head of the DHP used in this thesis.

percentage of area covered by each propagation medium inside the cross-section of the head of the healthy DHP shown in both Figure 4.10 and Figure 4.11. We hence take the healthy white matter as the dominant propagation medium for the inverse filters for both our approach and the approach in [1]. We assign $\omega_{\mathrm{M}} = 6$ and $\Delta_a = 0.025$ as in Section 4.2.1.3. We obtain the same a_0 as in Section 4.2.1.3, since the value of $T_{\mathrm{s}} \equiv \Delta t$ is identical to that in Section 4.2.1.2.

We set the parameter s in a similar manner to Section 4.2.1.3. We use (3.29) to plot in Figure 4.13 $\gamma(f_{\min}, r)$, $\gamma(f_{\mathrm{c}}, r)$, and $\gamma(f_{\max}, r)$ for propagation distance

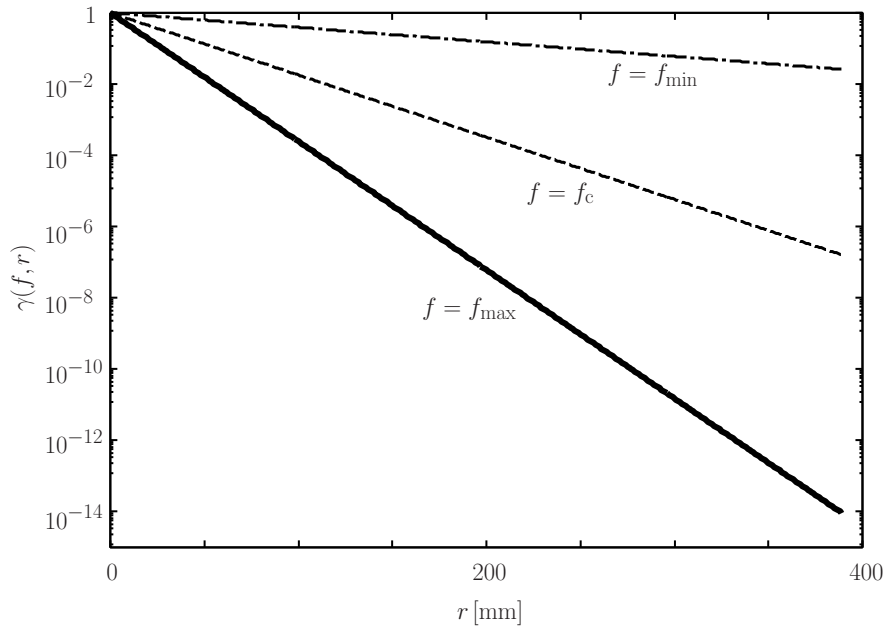

Figure 4.13: Theoretical calculation of $\gamma(f, r)$ in homogeneous white matter tissue.

r inside homogeneous and isotropic healthy white matter tissue. We consider the longest distance from the interrogating TRA element of the 2D experiments at $(x, y) = (177, 67)$ to the farthest receiving TRA element at $(x, y) = (103, 217)$ as in $r = \sqrt{(177-103)^2 + (67-217)^2} \approx 168\,\mathrm{mm}$. The round-trip time for this distance in white matter tissue is $t = \frac{0.168\,\mathrm{m}}{c^{\mathrm{wh.mat.}}}$, where $c^{\mathrm{wh.mat.}}$ is the speed of light in the the healthy white matter tissue. Therefore, the frequency $f_{\max}$ propagating in the healthy white matter undergoes attenuation with respect to propagation time of $\gamma(f_{\max}, \frac{0.168\,\mathrm{m}}{c^{\mathrm{wh.mat.}}}) \approx 10^{-7}$. We take into consideration that there are media present in this scenario which are more lossy than the chosen dominant medium at the frequency band of interest (e.g. muscle tissue, skin tissue). Therefore, we choose $s = 10^{-7}$ (rather than $s = 10^{-6}$), to account for possible further attenuation of the interrogation pulse of interest than calculated using merely the homogeneous white matter tissue as the dominant medium.

4.2.2.6 Acquisition of results

We perform the TR experiment using no compensation for the effects of dispersion (conventional TR approach), using our proposed resolution enhancement approach, and using the inverse filtering method in [1]. We use the minimum entropy criterion to objectively decide on the time of refocusing, as in Section 4.2.1.4. We

quantify the spatial resolution of the refocusing in the E_z field achieved by each method. The scattering strength in this scenario is weaker than that in the case of canonical test with the PEC scatterer. We expect that our approach outperforms the rest in terms of the resolution of the TR refocusing.

4.2.3 Constitutive parameters of the propagation media

Throughout Section 4.2, we assume non-magnetic propagation media. That is, we assume $\mu_{\mathrm{r}} = 1$ for all propagation media. We use the one-pole Debye relaxation model for all propagation media in all simulations in Section 4.2. In Table 4.2, we list the Debye media parameters which we use with the numerical simulations outlined in Section 4.2. The reference lossless propagation medium used in the

Table 4.2: Debye parameters of DHP media

Propagation medium	σ_{s} [S/m]	ϵ_{s}	ϵ_{∞}	τ_D [ps]
Bone	0.104	14.169	7.363	0.341
Cerebellum	0.826	58.155	35.195	0.683
Cerebral cortex	0.595	56.444	33.057	0.352
Cerebrospinal fluid	2.144	70.400	33.148	0.182
Eyeball	1.445	67.711	10.308	8.271
Fat	0.037	5.531	3.998	0.236
Hypothalamus	0.595	56.444	33.057	0.352
Midbrain	0.348	41.281	24.371	0.336
Muscle	0.747	56.932	28.001	0.187
Paranasal sinus	0.000	1.000	1.000	0.000
Skin	0.541	47.930	29.851	0.436
White matter	0.348	41.281	24.371	0.336

canonical experiments in Section 4.2.1.4 has $\sigma_{\mathrm{s}} = 0$ and $\epsilon_{\mathrm{s}} \triangleq {\epsilon_{\infty}}^{\mathrm{muscle}}$ [16], where ${\epsilon_{\infty}}^{\mathrm{muscle}}$ is the optical permittivity of muscle tissue. We set the relative permittivity ${\epsilon_{\mathrm{r}}}^{\mathrm{tumour}}$ of the brain tumour as [105] ${\epsilon_{\mathrm{r}}}^{\mathrm{tumour}}(f) = {\epsilon_{\mathrm{r}}}^{\mathrm{wh.\ matter}}(f) \times (1 + 30\%)$, where ${\epsilon_{\mathrm{r}}}^{\mathrm{wh.\ matter}}(f)$ is the complex relative permittivity of healthy white matter [95]. The permittivity and conductivity of the brain tumour are plotted in

Figure 4.14 and Figure 4.15 together with that of healthy white matter and muscle tissue for comparison.

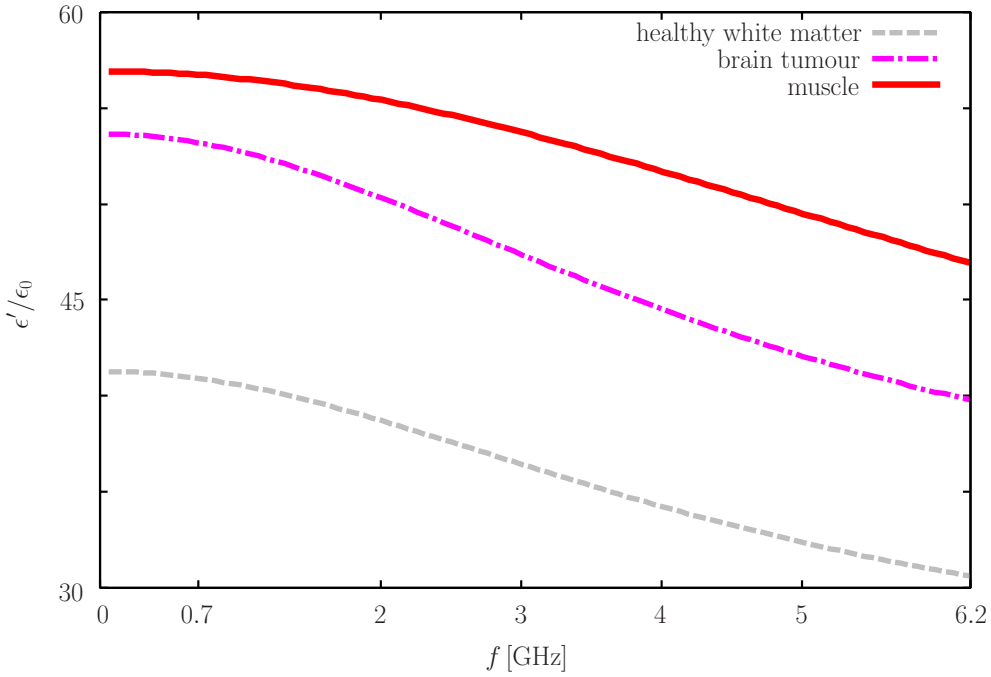

Figure 4.14: Equivalent relative permittivity of muscle tissue, healthy white matter tissue and brain tumour.

4.3 Summary

In this chapter, we detailed the setup of the simulations which aim to investigate the performance of the methods we proposed in Chapter 3. For each simulation experiment described in this section, we specified the simulated geometry and radio environment, the configuration of the parameters used by the signal processing techniques we apply on the experiments and the process by which we acquire results. Moreover, we specified the aims and our expectations of each experiment.

For our approach for the TWRI of multiple extended moving targets, we designed two canonical case experiments which aim to investigate the merit of temporal windowing and spatial windowing individually, when each windowing technique is used together with our radar imaging approach. We expect that the temporal windowing of the differential MDM enables the detection of targets effectively hidden behind other moving targets, which are otherwise undetected.

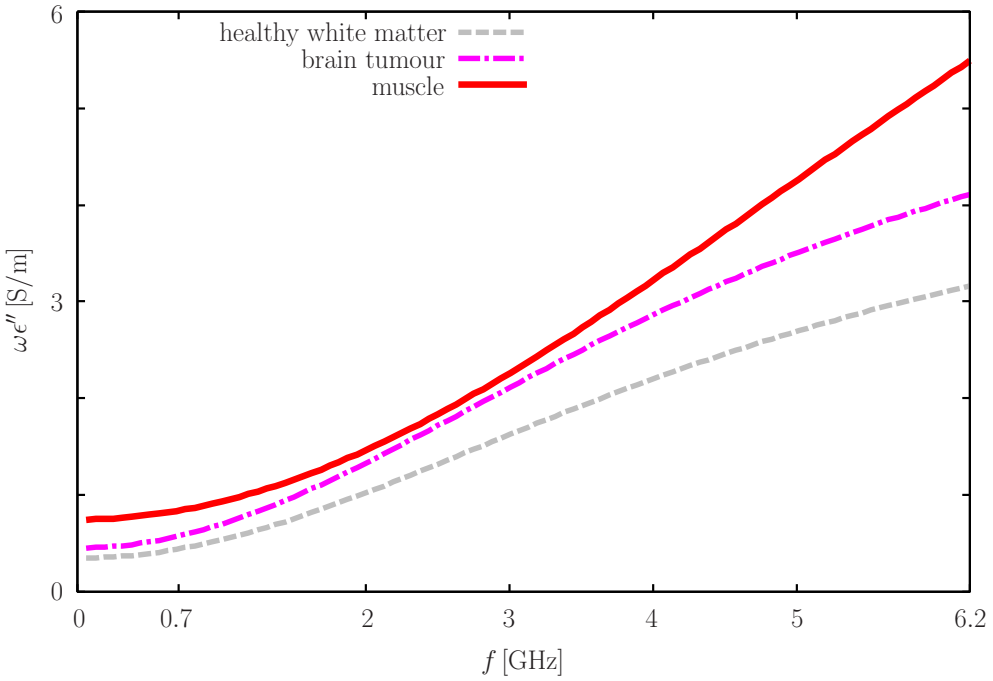

Figure 4.15: Equivalent conductivities of muscle tissue, healthy white matter tissue and brain tumour.

We also expect that the spatial windowing of the differential MDM enhances the detection of weaker targets which are roughly equidistant from the TRA in the presence of more dominant ones. Moreover, we consider a practical case scenario which involves five human-mimicking objects moving behind a brick wall. We expect that detection of all five extended moving targets is possible with our novel approach but not possible with the existing work.

For our proposed resolution enhancement approach for TR imaging applications, we designed a canonical test scenario which aims to investigate the merit of our approach in a simple, homogeneous, dispersive propagation environment in terms of improvement in the TR refocusing resolution. We also developed a practical case scenario which aims to demonstrate enhancement of the refocusing resolution of the UWB TR imaging of a brain tumour inside the head of a DHP using our proposed TR resolution enhancement algorithm. For both scenarios, we expect that our novel algorithm achieves a more precise refocusing than the prior work. Further, we integrate the minimum entropy criterion to dispersion compensation problems for the first time to the author's knowledge, to objectively determine the time of TR refocusing in our experiments.

In the next chapter, we perform the simulations of the scenarios considered

in this chapter and discuss the results.

Chapter 5

Results and Discussion

In this chapter, we perform the simulation experiments we detailed in Chapter 4. We present and examine the results obtained from each experiment.

5.1 Through-the-wall radar imaging of extended moving targets

In this section we present and discuss the results of the experiments we set up in Section 4.1.

5.1.1 Canonical test: Two targets overlapping in the downrange direction

In this section, we perform the experiments described in Section 4.1.1. Figure 5.1 illustrates $\tilde{\mathcal{M}}[\boldsymbol{x}]$ for the case where spatiotemporal windowing is not applied, i.e. when $\boldsymbol{K}_{\mathbf{d}1,1}[\boldsymbol{x}] \equiv \boldsymbol{K}_{\mathbf{d}}[\boldsymbol{x}]$ and $\tilde{\mathcal{M}}_{1,1}[\boldsymbol{x}] \equiv \tilde{\mathcal{M}}[\boldsymbol{x}]$. In this case, $\tilde{\mathcal{M}}[\boldsymbol{x}]$ has a peak value at the location of the middle TRA element at $x = 0.72\,\mathrm{m}$. Along the cross-range length of the wooden board, $\tilde{\mathcal{M}}[\boldsymbol{x}]$ has low numeric values. The radar image has values near zero away from the cross-range support of the wooden board. Clutter is observed between the ground truth locations of the wooden board and the wooden cylinder along the downrange line of the middle TRA element, $x = 0.72\,\mathrm{m}$. The wooden cylinder is not detected in the case without spatiotemporal windowing of $\boldsymbol{K}_{\mathbf{d}}$.

Figure 5.2 displays $\tilde{\mathcal{M}}[\boldsymbol{x}]$ for the case where temporal windowing is applied on $\boldsymbol{K}_{\mathbf{d}}$ with $P = 2000$. This produces $M = 2$ temporal windows and effectively $L = 1$

spatial window. Figure 5.3 and Figure 5.4 show $\tilde{\mathcal{M}}_{1,1}[\boldsymbol{x}]$ and $\tilde{\mathcal{M}}_{1,2}[\boldsymbol{x}]$ respectively for this case. Figure 5.5 is the cross-section of $\tilde{\mathcal{M}}[\boldsymbol{x}]$ at cross-range of 0.72 m for the cases where windowing is not applied and where temporal windowing is applied with $P = 2000$. This temporal windowing of the differential MDM allows both the moving wooden cylinder and the moving wooden board to be detected in $\tilde{\mathcal{M}}[\boldsymbol{x}]$. Specifically, the wooden board is detected with two local maxima in $\tilde{\mathcal{M}}_{1,1}[\boldsymbol{x}]$. The wooden cylinder is detected with one local maximum in $\tilde{\mathcal{M}}_{1,2}[\boldsymbol{x}]$. (3.16) combines these detections in these two temporal windows to yield the total radar image containing all detections originating from each individual window. Hence, $\tilde{\mathcal{M}}[\boldsymbol{x}]$ contains images of both targets in the case where temporal windowing is used. We note that we cannot extract information on the targets' size from $\tilde{\mathcal{M}}[\boldsymbol{x}]$.

Figure 5.6 presents the singular values at k_c (corresponding to f_c) for the scenario in Section 4.1.1 without windowing and with temporal windowing of $P = 2000$. Figure 5.6 also displays $\mathcal{N}_{l,m}^{\Theta\Sigma}[k_\mathrm{c}]$ for each case. The value of $\mathcal{N}_{1,1}^{\Theta\Sigma}[k_\mathrm{c}]$ for the case where no windowing is used is equal to $\mathcal{N}_{1,1}^{\Theta\Sigma}[k_\mathrm{c}]$ for $\tilde{\mathcal{M}}_{1,1}$ when windowing is used. From this together with the visual inspection of $\tilde{\mathcal{M}}[\boldsymbol{x}]$ (Figure 5.1) and $\tilde{\mathcal{M}}_{1,1}[\boldsymbol{x}]$ (Figure 5.3), we deduce that the signals caused by the movement of the wooden board dominate the signal subspace of $\boldsymbol{K}_\mathbf{d}$. Hence, the temporal windowing of the differential MDM effectively isolated the differential signals due to the displacement of the cylindrical target and the wooden board.

5.1.2 Canonical test: Three targets overlapping in the cross-range direction

In this section, we perform the experiments we set up in Section 4.1.2. Figure 5.7 displays $\tilde{\mathcal{M}}[\boldsymbol{x}]$ for the case where spatiotemporal windowing is not applied. Figure 5.8 illustrates $\tilde{\mathcal{M}}[\boldsymbol{x}]$ for the same scenario when we apply spatial windowing on $\boldsymbol{K}_\mathbf{d}$ with $\mathcal{N}_\mathrm{sw} = 9$. Figures 5.9–5.12 present cross-sections containing local maxima of the normalised radar image $\tilde{\mathcal{M}}[\boldsymbol{x}]$, along the range and cross-range directions, for the cases with and without spatial windowing.

In the case where spatiotemporal windowing is not applied, wooden board 2 is detected clearly in $\tilde{\mathcal{M}}[\boldsymbol{x}]$. Wooden boards 1 and 3 appear faint when spatiotemporal windowing is not used (Figures 5.7, 5.9, and 5.10). This is because wooden board 2 is closer to the centre of the TRA than the other two wooden

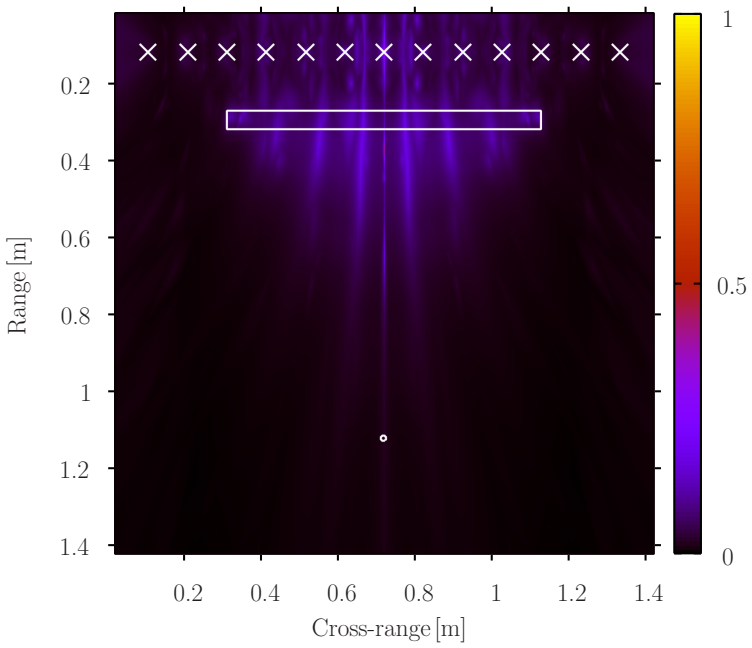

Figure 5.1: $\tilde{\mathcal{M}}[\boldsymbol{x}]$ for the scenario in Section 4.1.1 with no spatiotemporal windowing. The '×' marks represent the TRA elements. The ground truth location of the targets is represented by white shapes.

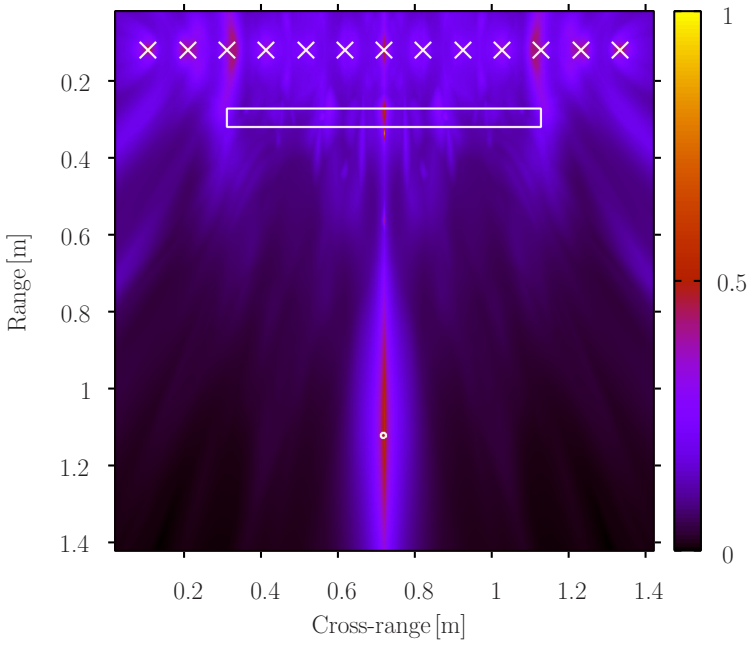

Figure 5.2: $\tilde{\mathcal{M}}[\boldsymbol{x}]$ for the scenario in Section 4.1.1 using temporal windowing with $P = 2000$. The '×' marks represent the TRA elements. The ground truth location of the targets is represented by white shapes.

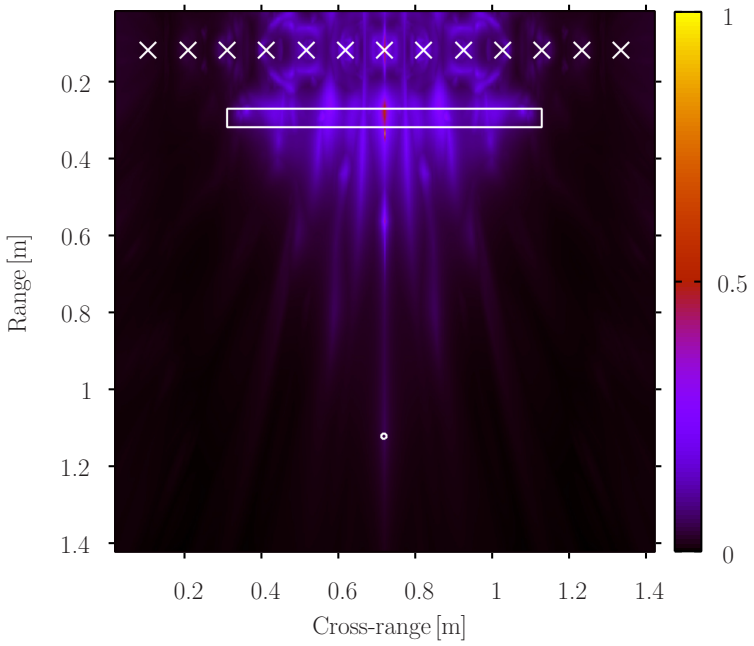

Figure 5.3: $\tilde{\mathcal{M}}_{1,1}$ for the scenario in Section 4.1.1 using temporal windowing with $P = 2000$. The '×' marks represent the TRA elements. The ground truth location of the targets is represented by white shapes.

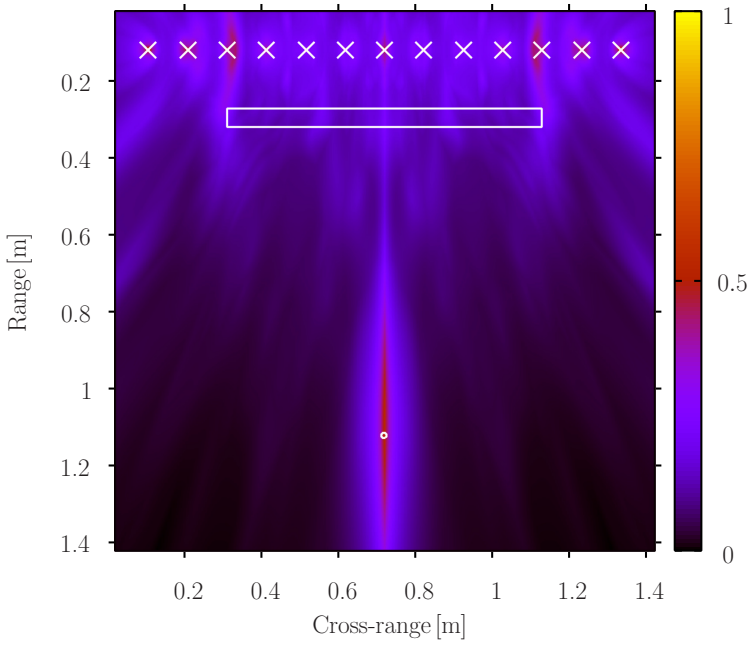

Figure 5.4: $\tilde{\mathcal{M}}_{1,2}$ for the scenario in Section 4.1.1 using temporal windowing with $P = 2000$. The '×' marks represent the TRA elements. The ground truth location of the targets is represented by white shapes.

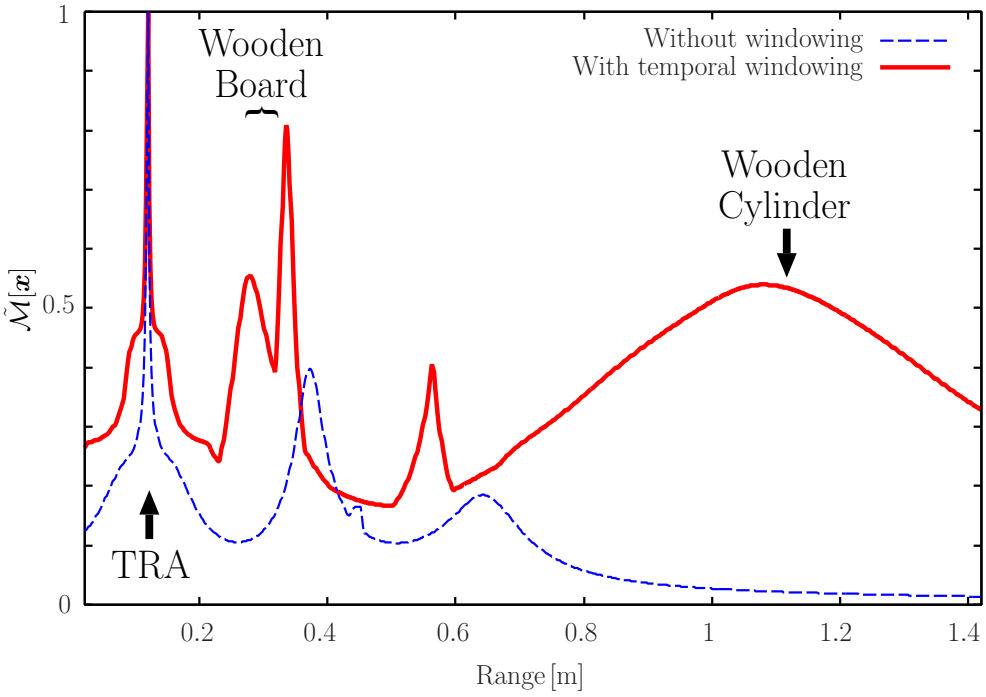

Figure 5.5: Comparison of cross-section of $\tilde{\mathcal{M}}[\boldsymbol{x}]$ for the scenario in Section 4.1.1 at cross-range of 0.72 m without spatiotemporal windowing and with temporal windowing of $P = 2000$.

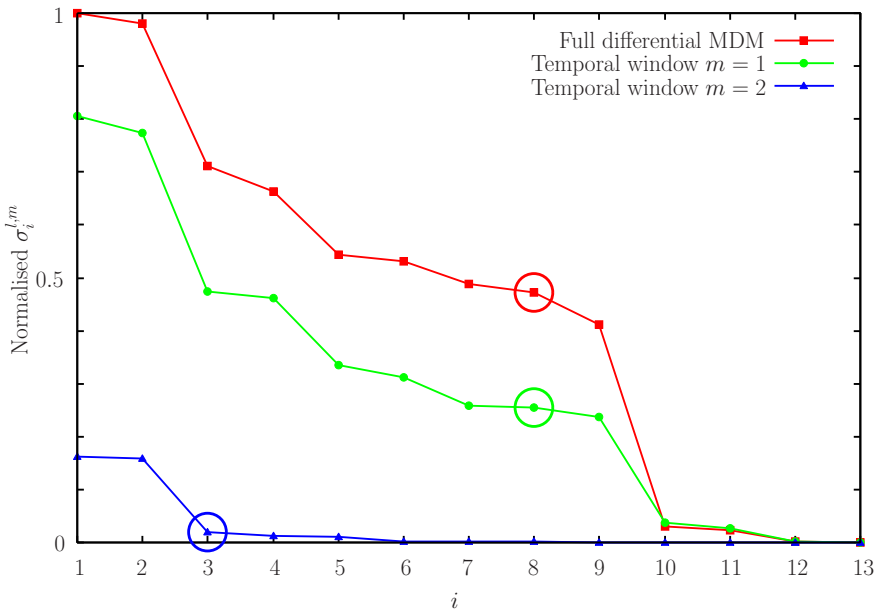

Figure 5.6: Normalised distribution of singular values at k_c for the scenario in Section 4.1.1 without windowing and with temporal windowing of $P = 2000$. The circled values correspond to $i = \mathcal{N}_{l,m}^{\Theta\Sigma}[k_c]$ for each case.

boards. When spatial windowing is used, wooden boards 1 and 3 appear stronger in $\tilde{\mathcal{M}}[\boldsymbol{x}]$, relative to the case where windowing is not applied (Figures 5.8, 5.9, and 5.10). This implies that the spatial windowing enhances the detection of weak targets which are roughly equidistant to the TRA. Thus, with spatial windowing we can identify targets visually in $\tilde{\mathcal{M}}[\boldsymbol{x}]$ which are hard to identify without the application of windowing. When spatiotemporal windowing is not applied, the peak of $\tilde{\mathcal{M}}[\boldsymbol{x}]$ is near the TRA. When spatiotemporal windowing is applied, the final radar image also has peaks ($\tilde{\mathcal{M}}[\boldsymbol{x}] \approx 1$) on wooden board 2 (Figures 5.8, 5.11, and 5.12).

For the case where windowing is applied, we obtain $L = 5$ spatial windows. As we do not use temporal windowing with this scenario, we effectively have $M = 1$ temporal window. Figures 5.13–5.17 present $\tilde{\mathcal{M}}_{1,1}[\boldsymbol{x}]$–$\tilde{\mathcal{M}}_{5,1}[\boldsymbol{x}]$ respectively. $\tilde{\mathcal{M}}_{1,1}[\boldsymbol{x}]$ detects wooden board 1. The peak of $\tilde{\mathcal{M}}_{1,1}[\boldsymbol{x}]$ is near the TRA. We observe artefacts between the targets and the first $\mathcal{N}_{\text{sw}}$ TRA elements. $\tilde{\mathcal{M}}_{5,1}[\boldsymbol{x}]$ detects wooden board 3. Due to the symmetry of the scenario's geometry, $\tilde{\mathcal{M}}_{1,1}[\boldsymbol{x}]$ is symmetric to $\tilde{\mathcal{M}}_{5,1}[\boldsymbol{x}]$ with respect to $x = 0.72\,\text{m}$. That is, $\tilde{\mathcal{M}}_{1,1}[(x, y)] = \tilde{\mathcal{M}}_{5,1}[(1.44\,\text{m} - x, y)]$. Similarly, $\tilde{\mathcal{M}}_{2,1}[\boldsymbol{x}]$ is symmetric to $\tilde{\mathcal{M}}_{4,1}[\boldsymbol{x}]$. Also with this scenario, the targets' shape and size cannot be determined from $\tilde{\mathcal{M}}[\boldsymbol{x}]$. Figure 5.18 illustrates the singular values at k_{c} (corresponding to f_{c}) for the scenario in Section 4.1.2 without windowing and with spatial windowing of $\mathcal{N}_{\text{sw}} = 9$. Due to the symmetric geometry of this scenario, the distribution of singular values of $\boldsymbol{K}_{\mathbf{d}l,1}[k_{\text{c}}]$ is the same as the distribution of singular values of $\boldsymbol{K}_{\mathbf{d}(5-l+1),1}[k_{\text{c}}]$.

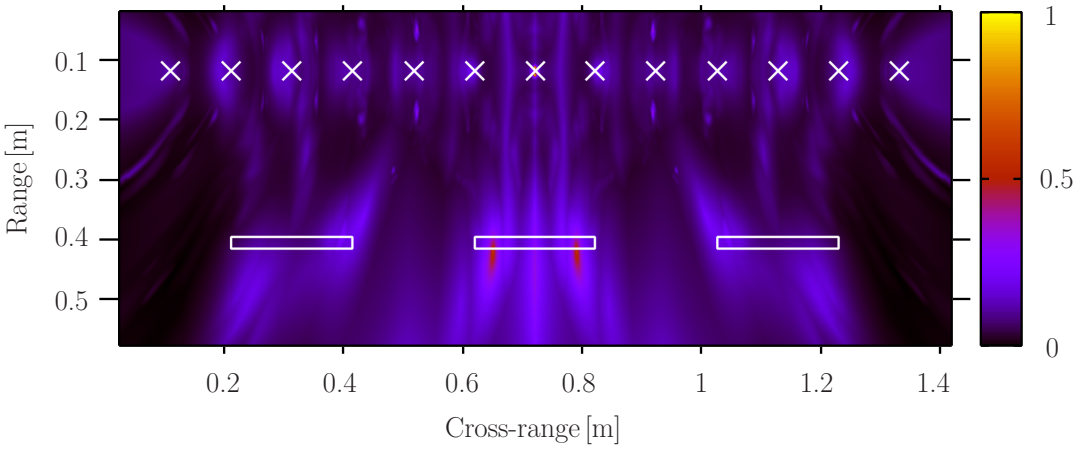

Figure 5.7: $\tilde{\mathcal{M}}[\boldsymbol{x}]$ for the scenario in Section 4.1.2 with no spatiotemporal windowing. The '×' marks represent the TRA elements. The ground truth location of the targets is represented by white shapes.

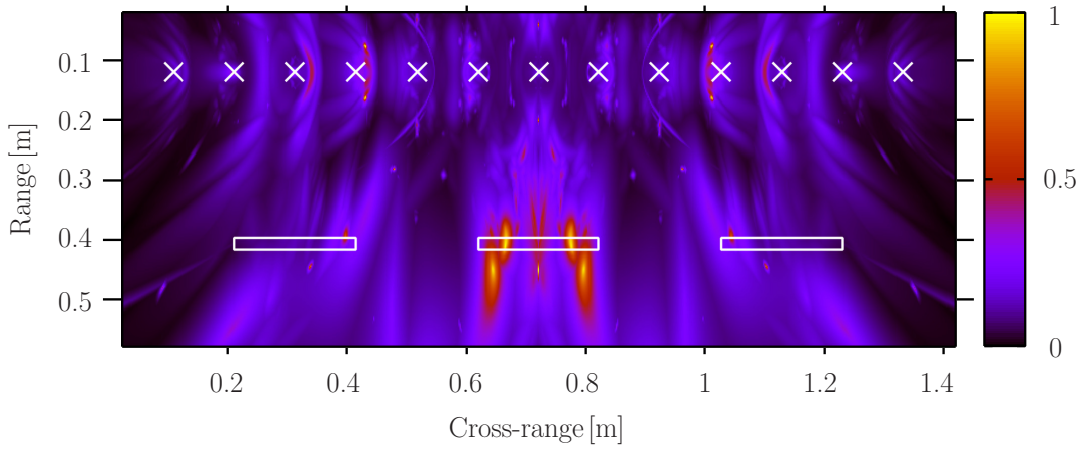

Figure 5.8: $\tilde{\mathcal{M}}[\boldsymbol{x}]$ for the scenario in Section 4.1.2 with $\mathcal{N}_{\text{sw}} = 9$. The '×' marks represent the TRA elements. The ground truth location of the targets is represented by white shapes.

5.1.3 Practical case scenario

In this section, we perform the experiments we detailed in Section 4.1.3. Figure 5.19 shows $\tilde{\mathcal{M}}[\boldsymbol{x}]$ for the scenario in Section 4.1.3 with no spatiotemporal windowing applied. The maximum value of $\tilde{\mathcal{M}}[\boldsymbol{x}]$ is located on the inner edge of the brick wall, i.e. near $y = 42\,\text{cm}$. Targets 2, 3, and 4 are clearly detected. Target 1 is detected with a poor contrast between the detections corresponding to the target and free space. Target 5 is not detected. We observe strong clutter between target 2 and the wall, target 3 and the wall, and between target 4 and the wall. Also, $\tilde{\mathcal{M}}[\boldsymbol{x}]$ has strong clutter behind target 4, i.e. in the area between $(x, y) = (1.2\,\text{m}, 1\,\text{m})$ to $(1.44\,\text{m}, 1.3\,\text{m})$.

Figure 5.20 shows $\tilde{\mathcal{M}}[\boldsymbol{x}]$ for the case where spatiotemporal windowing is applied with $\mathcal{N}_{\text{sw}} = 9$, $P = 1500$, and $\mathcal{N}^{\Theta}_{l,m}[k] \triangleq \mathcal{N}^{\Theta\Sigma}_{l,m}[k]$. Our approach detects all five moving targets. $\tilde{\mathcal{M}}[\boldsymbol{x}]$ for this case contains strong values near the inner edge of the brick wall. We observe strong clutter in the area between target 5 and targets 1 and 2. Figure 5.21 and Figure 5.22 show $\tilde{\mathcal{M}}_{1,1}[\boldsymbol{x}]$ and $\tilde{\mathcal{M}}_{1,4}[\boldsymbol{x}]$ respectively. Figure 5.23 and Figure 5.24 illustrate $\tilde{\mathcal{M}}_{3,3}[\boldsymbol{x}]$ and $\tilde{\mathcal{M}}_{3,5}[\boldsymbol{x}]$ respectively. Figure 5.25 displays $\tilde{\mathcal{M}}_{4,2}[\boldsymbol{x}]$. Figures 5.26, 5.27, 5.28, and 5.29 show $\tilde{\mathcal{M}}_{5,1}[\boldsymbol{x}]$, $\tilde{\mathcal{M}}_{5,2}[\boldsymbol{x}]$, $\tilde{\mathcal{M}}_{5,3}[\boldsymbol{x}]$, and $\tilde{\mathcal{M}}_{5,5}[\boldsymbol{x}]$ respectively. Target 1 is detected in $\tilde{\mathcal{M}}_{1,1}[\boldsymbol{x}]$. Target 2 is detected in $\tilde{\mathcal{M}}_{1,4}[\boldsymbol{x}]$, $\tilde{\mathcal{M}}_{3,3}[\boldsymbol{x}]$, and $\tilde{\mathcal{M}}_{4,2}[\boldsymbol{x}]$. Target 3 is detected in $\tilde{\mathcal{M}}_{4,2}[\boldsymbol{x}]$, $\tilde{\mathcal{M}}_{5,1}[\boldsymbol{x}]$, and $\tilde{\mathcal{M}}_{5,3}[\boldsymbol{x}]$. Target 4 is detected in $\tilde{\mathcal{M}}_{3,5}[\boldsymbol{x}]$, $\tilde{\mathcal{M}}_{5,2}[\boldsymbol{x}]$, and

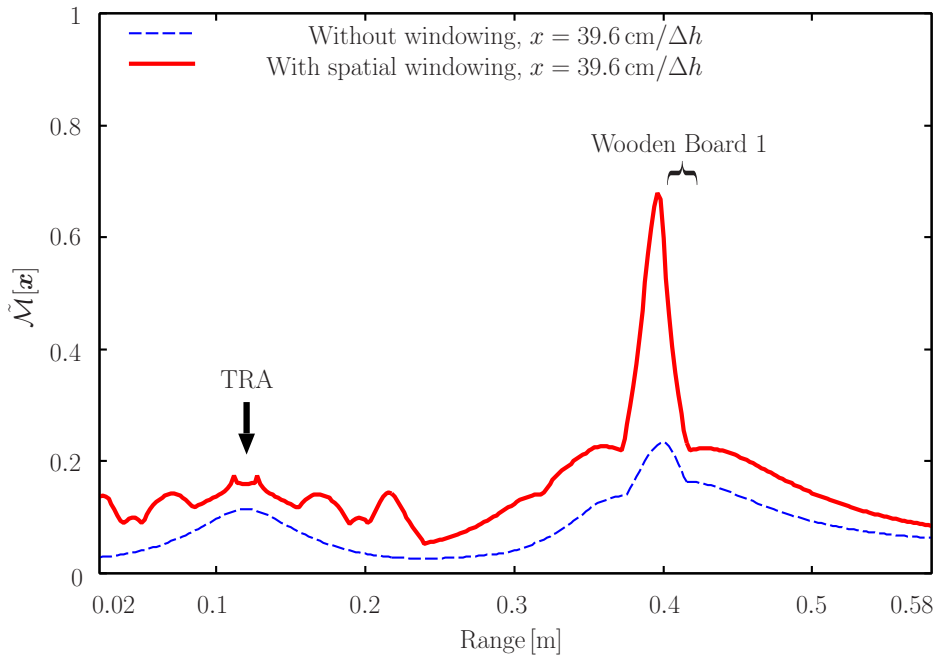

Figure 5.9: Comparison of cross-section of $\tilde{\mathcal{M}}[\boldsymbol{x}]$ for wooden board 1 in Section 4.1.2 at constant cross-range without spatiotemporal windowing and with spatial windowing of $\mathcal{N}_{\mathrm{sw}} = 9$.

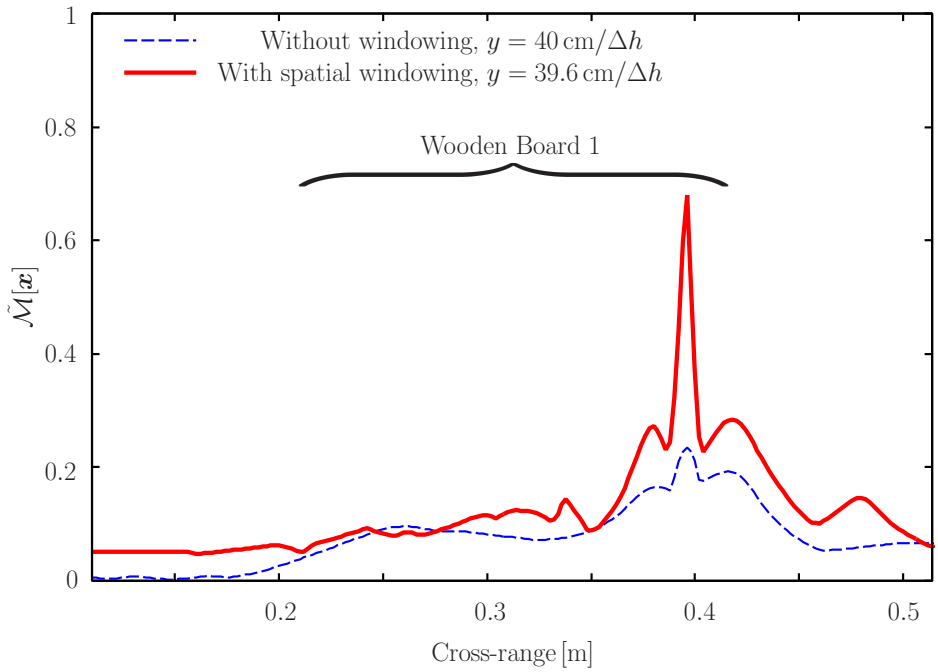

Figure 5.10: Comparison of cross-section of $\tilde{\mathcal{M}}[\boldsymbol{x}]$ for wooden board 1 in Section 4.1.2 at constant range without spatiotemporal windowing and with spatial windowing of $\mathcal{N}_{\mathrm{sw}} = 9$.

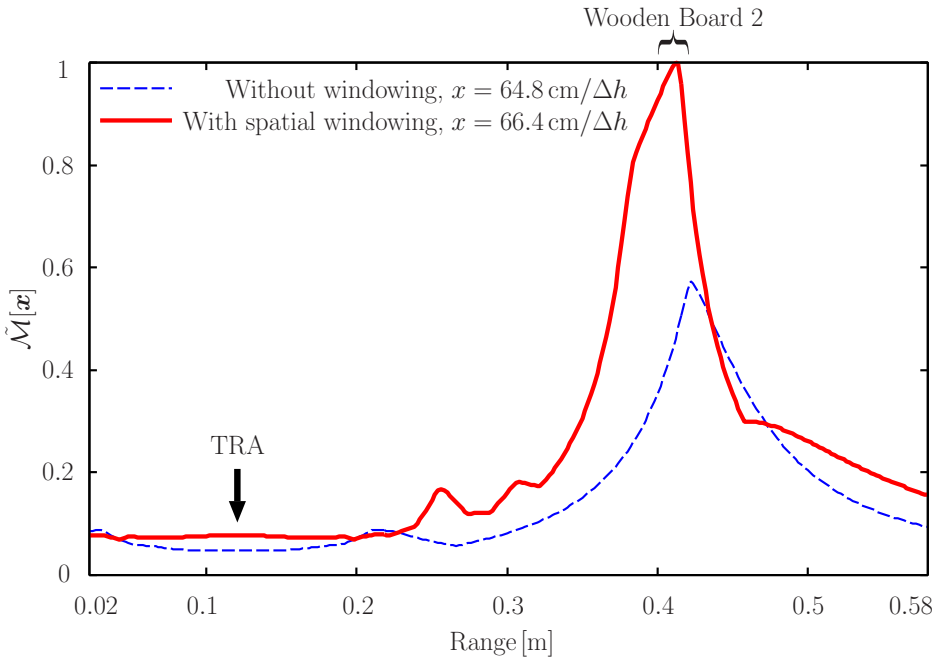

Figure 5.11: Comparison of cross-section of $\tilde{\mathcal{M}}[\boldsymbol{x}]$ for wooden board 2 in Section 4.1.2 at constant cross-range without spatiotemporal windowing and with spatial windowing of $\mathcal{N}_{\mathrm{sw}} = 9$.

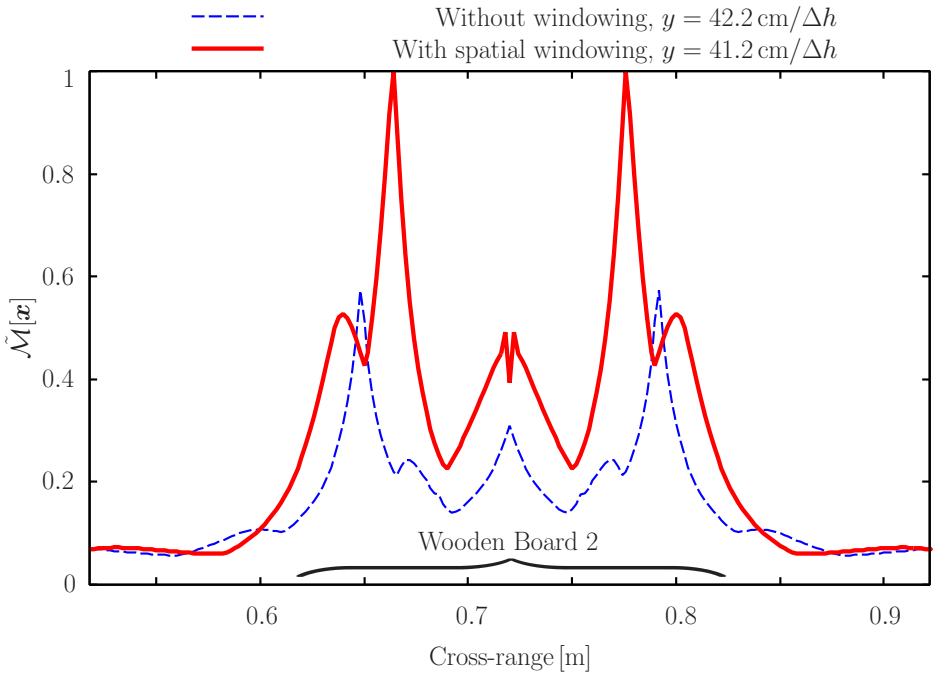

Figure 5.12: Comparison of cross-section of $\tilde{\mathcal{M}}[\boldsymbol{x}]$ for wooden board 2 in Section 4.1.2 at constant range without spatiotemporal windowing and with spatial windowing of $\mathcal{N}_{\mathrm{sw}} = 9$.

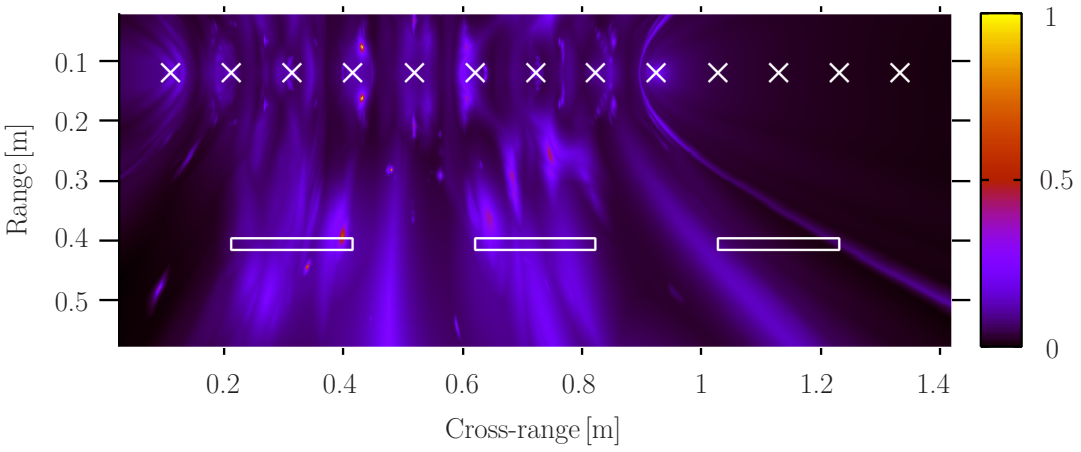

Figure 5.13: $\tilde{\mathcal{M}}_{1,1}[\boldsymbol{x}]$ for the scenario in Section 4.1.2 with $\mathcal{N}_{\text{sw}} = 9$. The '×' marks represent the TRA elements. The ground truth location of the targets is represented by white shapes.

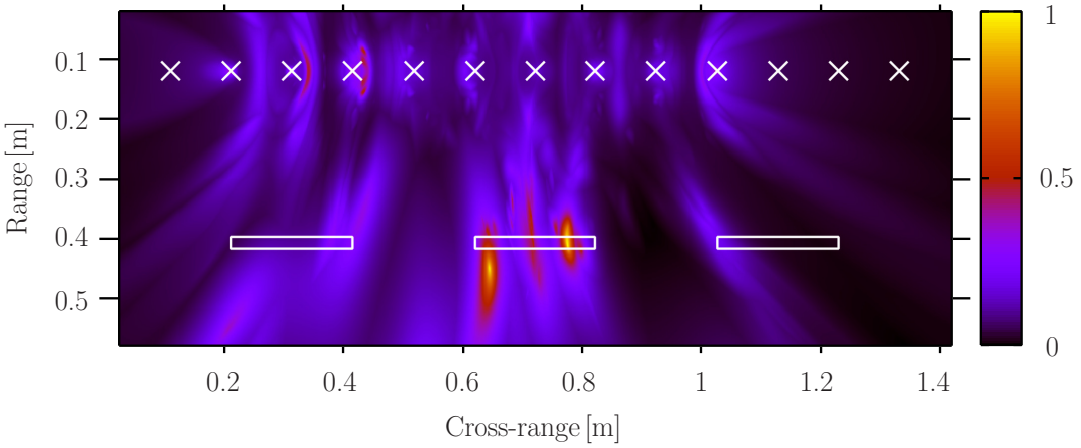

Figure 5.14: $\tilde{\mathcal{M}}_{2,1}[\boldsymbol{x}]$ for the scenario in Section 4.1.2 with $\mathcal{N}_{\text{sw}} = 9$. The '×' marks represent the TRA elements. The ground truth location of the targets is represented by white shapes.

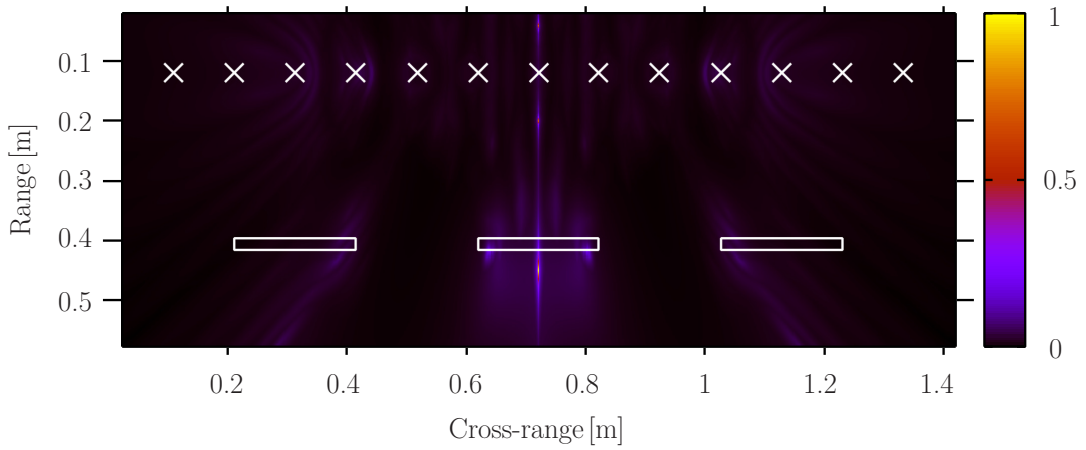

Figure 5.15: $\tilde{\mathcal{M}}_{3,1}[\boldsymbol{x}]$ for the scenario in Section 4.1.2 with $\mathcal{N}_{\text{sw}} = 9$. The '×' marks represent the TRA elements. The ground truth location of the targets is represented by white shapes.

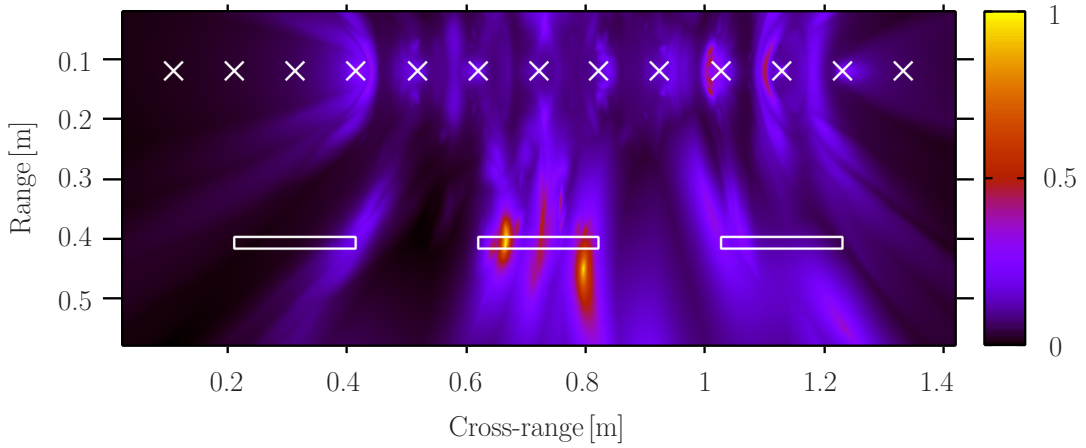

Figure 5.16: $\tilde{\mathcal{M}}_{4,1}[\boldsymbol{x}]$ for the scenario in Section 4.1.2 with $\mathcal{N}_{\text{sw}} = 9$. The '×' marks represent the TRA elements. The ground truth location of the targets is represented by white shapes.

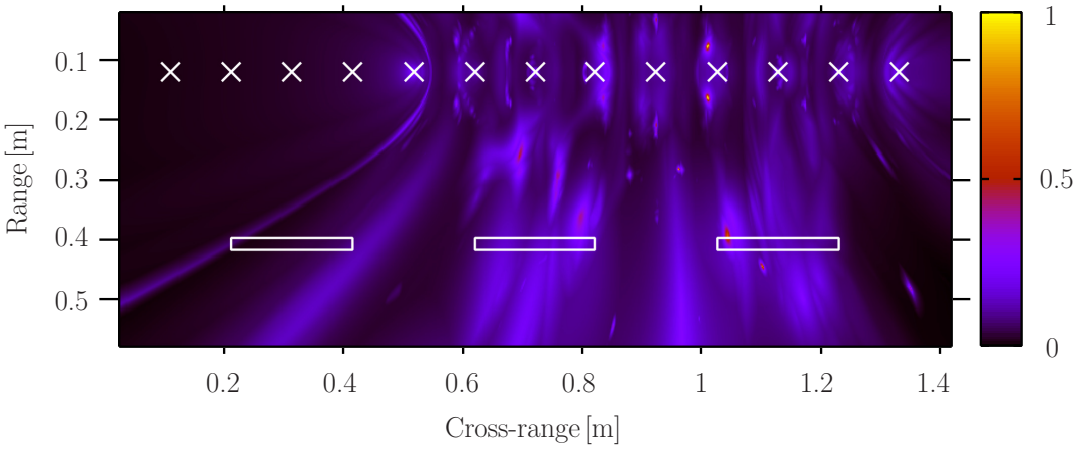

Figure 5.17: $\tilde{\mathcal{M}}_{5,1}[\boldsymbol{x}]$ for the scenario in Section 4.1.2 with $\mathcal{N}_{\text{sw}} = 9$. The '×' marks represent the TRA elements. The ground truth location of the targets is represented by white shapes.

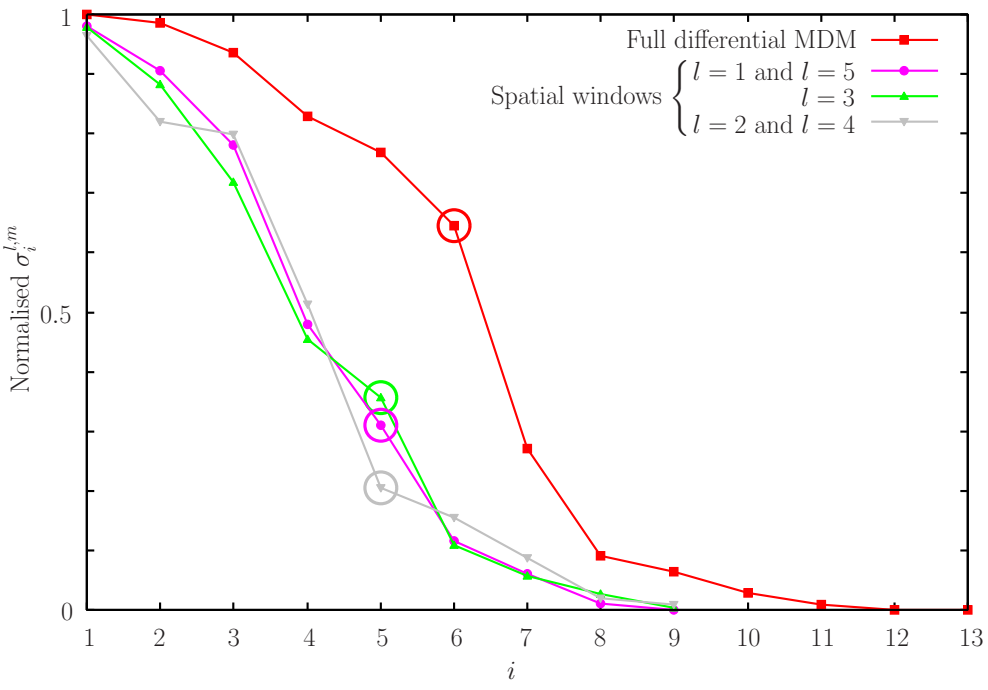

Figure 5.18: Normalised distribution of singular values at k_{c} for the scenario in Section 4.1.2 without windowing and with spatial windowing of $\mathcal{N}_{\text{sw}} = 9$. The circled values correspond to $i = \mathcal{N}_{l,m}^{\Theta\Sigma}[k_{\text{c}}]$ for each case.

$\tilde{\mathcal{M}}_{5,5}[\boldsymbol{x}]$. Target 5 is detected in $\tilde{\mathcal{M}}_{4,2}[\boldsymbol{x}]$. As each target is detected in at least one spatiotemporal window, $\tilde{\mathcal{M}}[\boldsymbol{x}]$ contains detections of all targets. We further note that our approach does not illustrate the approximate support of all of the targets.

When we first performed the simulation experiments in Section 4.1, we made a different empirical choice for the setting of $\mathcal{N}_{l,m}^{\Theta}[k]$. Instead of applying (3.11) to obtain $\mathcal{N}_{l,m}^{\Theta}[k] \triangleq \mathcal{N}_{l,m}^{\Theta\Sigma}[k]$, our simulation experiments used $\mathcal{N}_{l,m}^{\Theta\Sigma'}[k]$. Our simulation experiments calculated $\mathcal{N}_{l,m}^{\Theta\Sigma'}[k]$ as the minimum value which satisfies

$$\sigma_{(\mathcal{N}_{\mathrm{sw}})}^{l,m} + \sum_{i=1}^{\mathcal{N}_{l,m}^{\Theta\Sigma'}[k]} \sigma_i^{l,m} \geq 0.9 \cdot \sum_{p=1}^{\mathcal{N}_{\mathrm{sw}}} \sigma_p^{l,m}. \tag{5.1}$$

Figure 5.30 shows $\tilde{\mathcal{M}}[\boldsymbol{x}]$ for the case where spatiotemporal windowing is applied with $\mathcal{N}_{\mathrm{sw}} = 9$, $P = 1500$, and $\mathcal{N}_{l,m}^{\Theta}[k] \triangleq \mathcal{N}_{l,m}^{\Theta\Sigma'}[k]$. When we applied this threshold for deciding the dimension of the signal subspace with the two canonical scenarios, we did not obtain any significantly different results (any individual spatiotemporal windows or the final radar image) than the ones we obtained using $\mathcal{N}_{l,m}^{\Theta\Sigma}[k]$. The $\tilde{\mathcal{M}}[\boldsymbol{x}]$ we obtained using $\mathcal{N}_{l,m}^{\Theta\Sigma'}[k]$ for the practical scenario when no spatiotemporal windowing was not used, was also not significantly different than Figure 5.19. The $\tilde{\mathcal{M}}[\boldsymbol{x}]$ obtained using $\mathcal{N}_{l,m}^{\Theta\Sigma'}[k]$ when spatiotemporal windowing was used, was significantly different than the one obtained with $\mathcal{N}_{l,m}^{\Theta\Sigma}[k]$, featuring a different trade-off between the strengths of scattering centres shown and clutter in $\tilde{\mathcal{M}}[\boldsymbol{x}]$. Specifically, Figure 5.30 shows $\tilde{\mathcal{M}}[\boldsymbol{x}]$ obtained using $\mathcal{N}_{l,m}^{\Theta}[k] \triangleq \mathcal{N}_{l,m}^{\Theta\Sigma'}[k]$, $\mathcal{N}_{\mathrm{sw}} = 9$, and $P = 1500$. Target 5 is detected with a stronger numeric value in $\tilde{\mathcal{M}}[\boldsymbol{x}]$ using $\mathcal{N}_{l,m}^{\Theta\Sigma'}[k]$ than when $\mathcal{N}_{l,m}^{\Theta\Sigma}[k]$ is used. Also, the radar image obtained with $\mathcal{N}_{l,m}^{\Theta\Sigma'}[k]$ has more clutter than with $\mathcal{N}_{l,m}^{\Theta\Sigma}[k]$ in the area bound with $y > 0.8\,\mathrm{m}$ and $0.6\,\mathrm{m} < x < 0.8\,\mathrm{m}$. However, the radar image with $\mathcal{N}_{l,m}^{\Theta\Sigma'}[k]$ is less affected by artefacts as compared to imaging with $\mathcal{N}_{l,m}^{\Theta\Sigma}[k]$.

Figure 5.31 shows $\tilde{\mathcal{M}}[\boldsymbol{x}]$ for the case where spatiotemporal windowing is applied with $\mathcal{N}_{\mathrm{sw}} = 9$, $P = 1500$, and $\mathcal{N}_{l,m}^{\Theta}[k] \triangleq \mathcal{N}_{l,m}^{\Theta 10\%}[k]$. This approach has reduced the strong clutter near the inner edge of the brick wall relative to our approach. However, this approach fails to detect target 4. Moreover, the radar image in Figure 5.31 is affected by artefacts. Figure 5.32 illustrates $\tilde{\mathcal{M}}[\boldsymbol{x}]$ for the case where spatiotemporal windowing is applied with $\mathcal{N}_{\mathrm{sw}} = 9$, $P = 1500$, and $\mathcal{N}_{l,m}^{\Theta}[k] \triangleq \mathcal{N}_{l,m}^{\Theta\div}[k]$. $\tilde{\mathcal{M}}[\boldsymbol{x}]$ in Figure 5.32 is also affected by artefacts. Radar

imaging using the WF-MUSIC method with $\mathcal{N}_{l,m}^{\Theta}[k] \triangleq \mathcal{N}_{l,m}^{\Theta\div}[k]$ detects only target 3.

Figure 5.33 displays the final radar image for the case where the spatiotemporally windowed UWB-MUSIC method of [4] is used with $\boldsymbol{K}_{\mathbf{d}}[\boldsymbol{x}]$ in place of $\boldsymbol{K}[\boldsymbol{x}]$ with $\mathcal{N}_{\text{sw}} = 9$ and $P = 1500$. The method in [4] did not detect any of the targets in the final radar image. The method in [4] sums the non-normalised contribution of each spatiotemporal window to produce the final radar image functional. Therefore, contributions to the final radar image originating at the same location in individual spatiotemporal windows get stronger by the summation operation. Meanwhile, the detection of other targets at other locations effectively becomes weakened. Consequently, a target may be detected in a spatiotemporal window with spatial index l_0 and temporal index m_0, but not be detected in the final radar image functional. Also, with the method in [4], human target 5 is not detected in any imaging functional corresponding to any individual window. One reason for this lies on the UWB-MUSIC method itself. The UWB-MUSIC method sums each frequency's contribution to the imaging functional corresponding to each spatiotemporal window. However, frequencies above f_{c} effectively cannot penetrate targets 1–4. This is because the skin depth in the skin tissue at f_{c} is equal to the thickness of the skin tissue layer (2 mm). Hence, frequencies above f_{c} do not produce any strong contribution near target 5. Instead, they produce strong contributions near targets 1–4 on the side where the TRA is. Therefore, by summing the contributions of each frequency in Ω, any contributions from target 5 are hidden by the stronger contributions near the surface of targets 1–4.

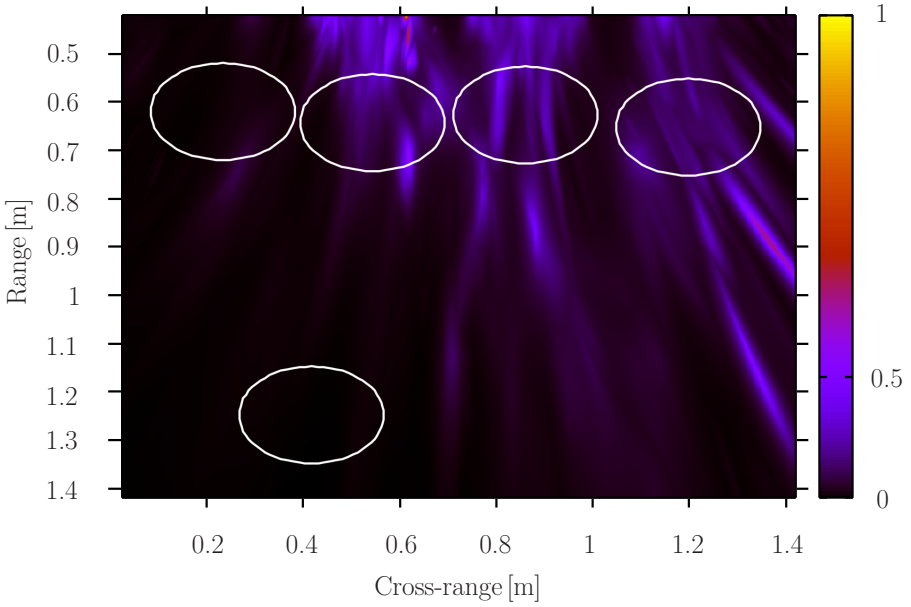

Figure 5.19: $\tilde{\mathcal{M}}[\boldsymbol{x}]$ for the scenario in Section 4.1.3 with no spatiotemporal windowing and $\mathcal{N}_{l,m}^{\Theta}[k] \triangleq \mathcal{N}_{l,m}^{\Theta\Sigma}[k]$. The ground truth location of the targets is represented by white shapes.

Figure 5.20: $\tilde{\mathcal{M}}(\boldsymbol{x})$ for the scenario in Section 4.1.3 with $\mathcal{N}_{\text{sw}} = 9$, $P = 1500$, and $\mathcal{N}_{l,m}^{\Theta}[k] \triangleq \mathcal{N}_{l,m}^{\Theta\Sigma}[k]$. The ground truth location of the targets is represented by white shapes.

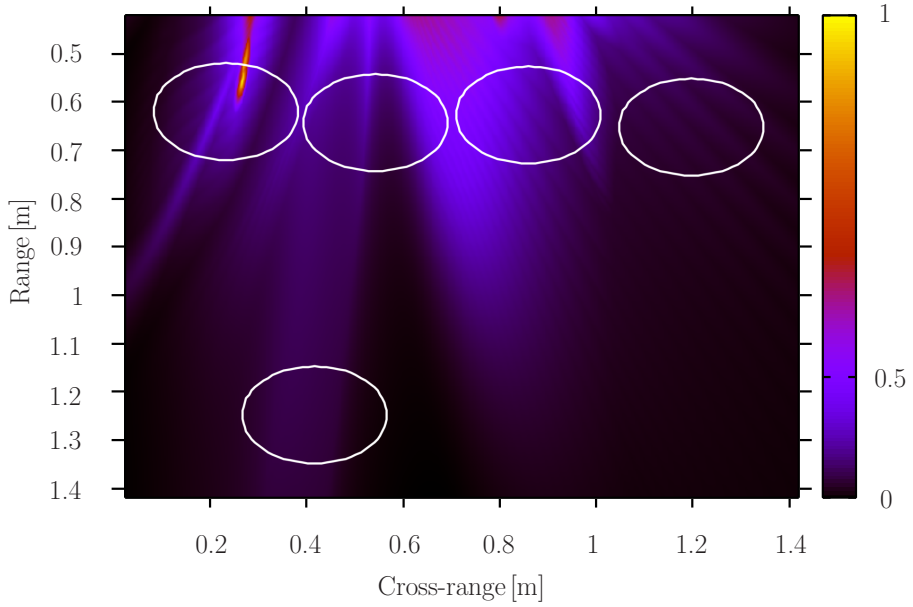

Figure 5.21: $\tilde{\mathcal{M}}_{1,1}[\boldsymbol{x}]$ for the scenario in Section 4.1.3 with $\mathcal{N}_{\text{sw}} = 9$, $P = 1500$, and $\mathcal{N}^{\Theta}_{l,m}[k] \triangleq \mathcal{N}^{\Theta\Sigma}_{l,m}[k]$. The ground truth location of the targets is represented by white shapes.

Figure 5.22: $\tilde{\mathcal{M}}_{1,4}[\boldsymbol{x}]$ for the scenario in Section 4.1.3 with $\mathcal{N}_{\text{sw}} = 9$, $P = 1500$, and $\mathcal{N}^{\Theta}_{l,m}[k] \triangleq \mathcal{N}^{\Theta\Sigma}_{l,m}[k]$. The ground truth location of the targets is represented by white shapes.

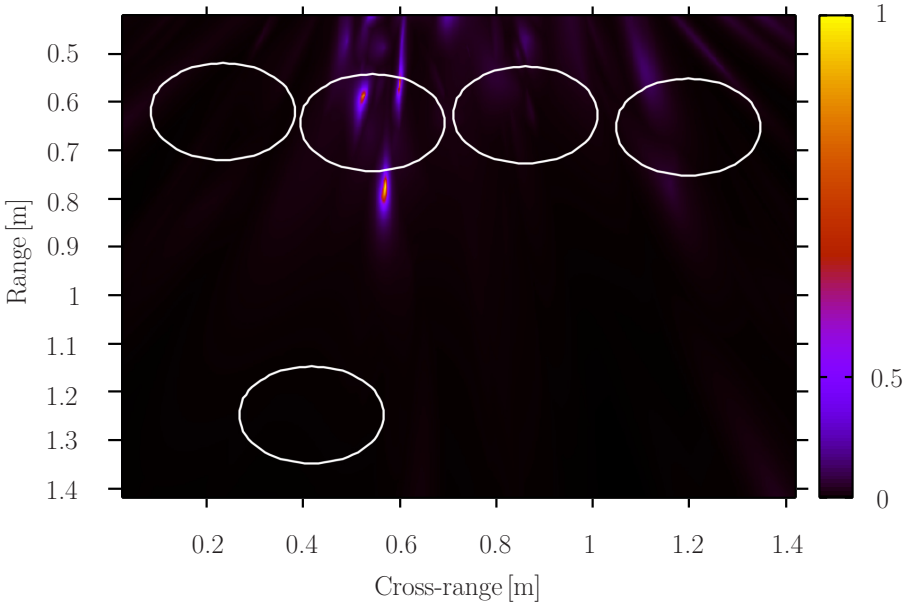

Figure 5.23: $\tilde{\mathcal{M}}_{3,3}[\boldsymbol{x}]$ for the scenario in Section 4.1.3 with $\mathcal{N}_{\text{sw}} = 9$, $P = 1500$, and $\mathcal{N}^{\Theta}_{l,m}[k] \triangleq \mathcal{N}^{\Theta\Sigma}_{l,m}[k]$. The ground truth location of the targets is represented by white shapes.

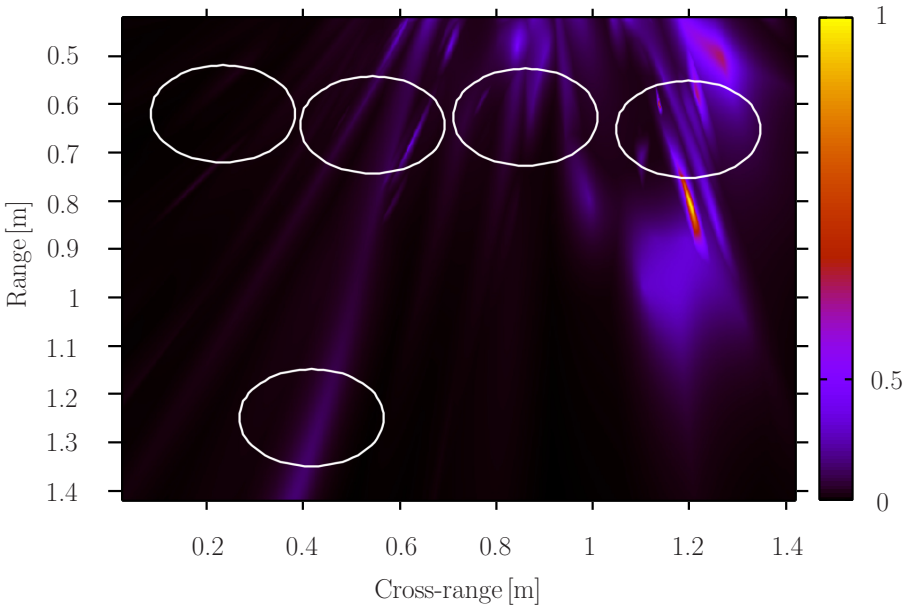

Figure 5.24: $\tilde{\mathcal{M}}_{3,5}[\boldsymbol{x}]$ for the scenario in Section 4.1.3 with $\mathcal{N}_{\text{sw}} = 9$, $P = 1500$, and $\mathcal{N}^{\Theta}_{l,m}[k] \triangleq \mathcal{N}^{\Theta\Sigma}_{l,m}[k]$. The ground truth location of the targets is represented by white shapes.

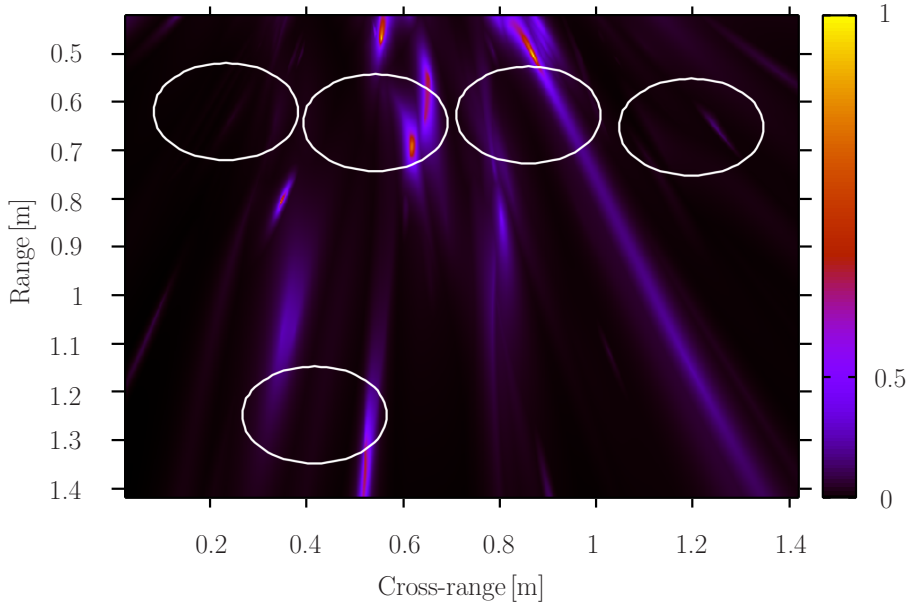

Figure 5.25: $\tilde{\mathcal{M}}_{4,2}[\boldsymbol{x}]$ for the scenario in Section 4.1.3 with $\mathcal{N}_{\text{sw}} = 9$, $P = 1500$, and $\mathcal{N}^{\Theta}_{l,m}[k] \triangleq \mathcal{N}^{\Theta\Sigma}_{l,m}[k]$. The ground truth location of the targets is represented by white shapes.

Figure 5.26: $\tilde{\mathcal{M}}_{5,1}[\boldsymbol{x}]$ for the scenario in Section 4.1.3 with $\mathcal{N}_{\text{sw}} = 9$, $P = 1500$, and $\mathcal{N}^{\Theta}_{l,m}[k] \triangleq \mathcal{N}^{\Theta\Sigma}_{l,m}[k]$. The ground truth location of the targets is represented by white shapes.

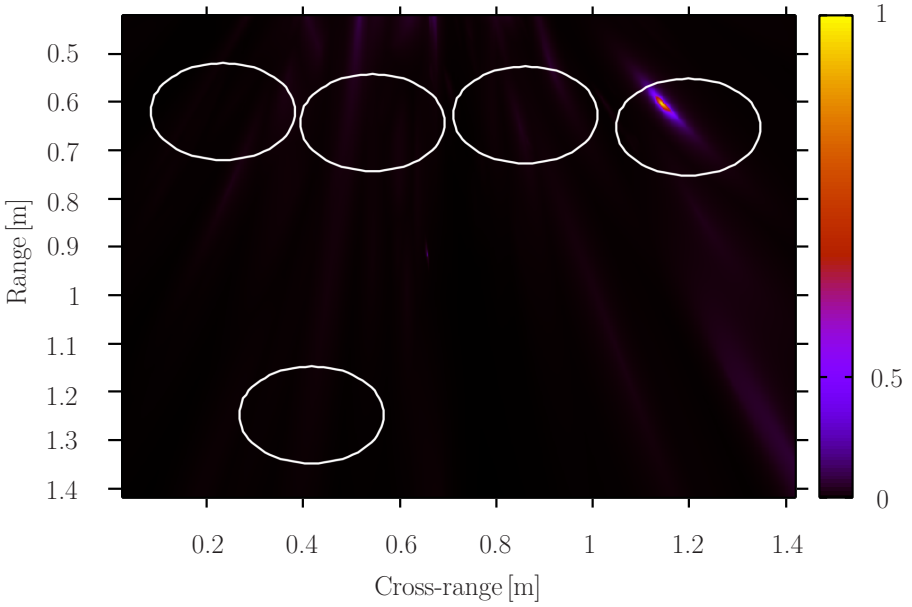

Figure 5.27: $\tilde{\mathcal{M}}_{5,2}[\boldsymbol{x}]$ for the scenario in Section 4.1.3 with $\mathcal{N}_{\text{sw}} = 9$, $P = 1500$, and $\mathcal{N}^{\Theta}_{l,m}[k] \triangleq \mathcal{N}^{\Theta\Sigma}_{l,m}[k]$. The ground truth location of the targets is represented by white shapes.

Figure 5.28: $\tilde{\mathcal{M}}_{5,3}[\boldsymbol{x}]$ for the scenario in Section 4.1.3 with $\mathcal{N}_{\text{sw}} = 9$, $P = 1500$, and $\mathcal{N}^{\Theta}_{l,m}[k] \triangleq \mathcal{N}^{\Theta\Sigma}_{l,m}[k]$. The ground truth location of the targets is represented by white shapes.

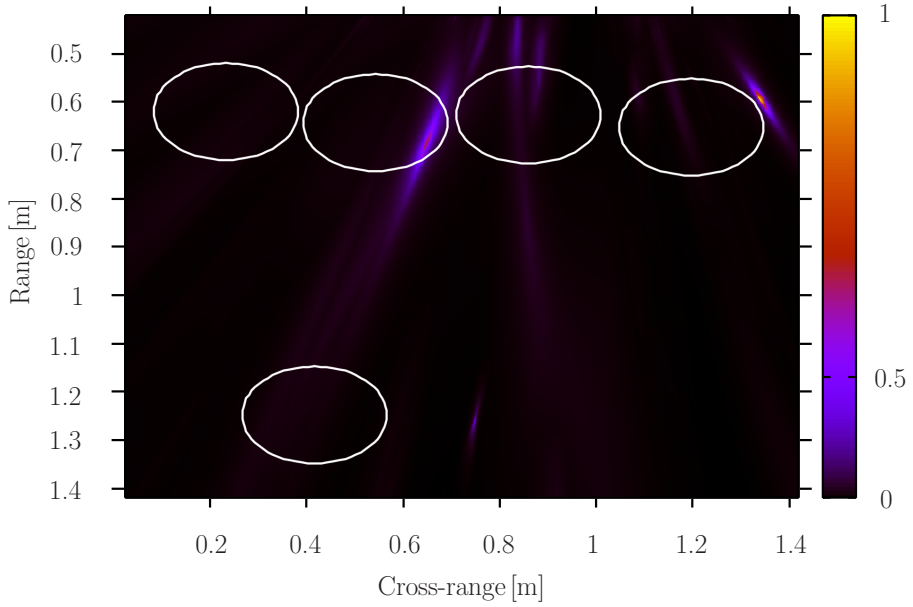

Figure 5.29: $\tilde{\mathcal{M}}_{5,5}[\boldsymbol{x}]$ for the scenario in Section 4.1.3 with $\mathcal{N}_{\text{sw}} = 9$, $P = 1500$, and $\mathcal{N}^{\Theta}_{l,m}[k] \triangleq \mathcal{N}^{\Theta\Sigma}_{l,m}[k]$. The ground truth location of the targets is represented by white shapes.

Figure 5.30: $\tilde{\mathcal{M}}(\boldsymbol{x})$ for the scenario in Section 4.1.3 with $\mathcal{N}_{\text{sw}} = 9$, $P = 1500$, and $\mathcal{N}^{\Theta}_{l,m}[k] \triangleq \mathcal{N}^{\Theta\Sigma'}_{l,m}[k]$. The ground truth location of the targets is represented by white shapes.

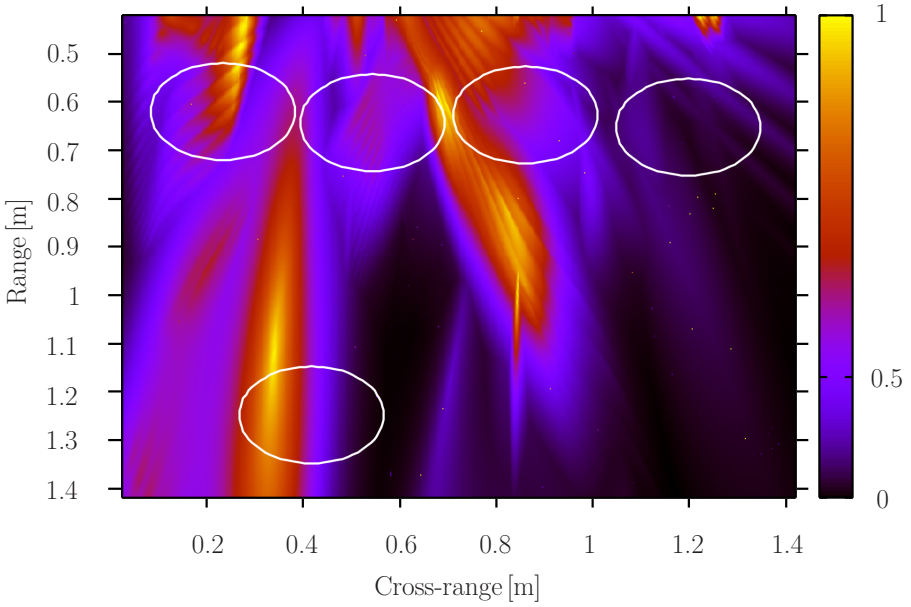

Figure 5.31: $\tilde{\mathcal{M}}(\boldsymbol{x})$ for the scenario in Section 4.1.3 with $\mathcal{N}_{\text{sw}} = 9$, $P = 1500$, and $\mathcal{N}_{l,m}^{\Theta}[k] \triangleq \mathcal{N}_{l,m}^{\Theta 10\%}[k]$. The ground truth location of the targets is represented by white shapes.

Figure 5.32: $\tilde{\mathcal{M}}(\boldsymbol{x})$ for the scenario in Section 4.1.3 with $\mathcal{N}_{\text{sw}} = 9$, $P = 1500$, and $\mathcal{N}_{l,m}^{\Theta}[k] \triangleq \mathcal{N}_{l,m}^{\Theta \div}[k]$. The ground truth location of the targets is represented by white shapes.

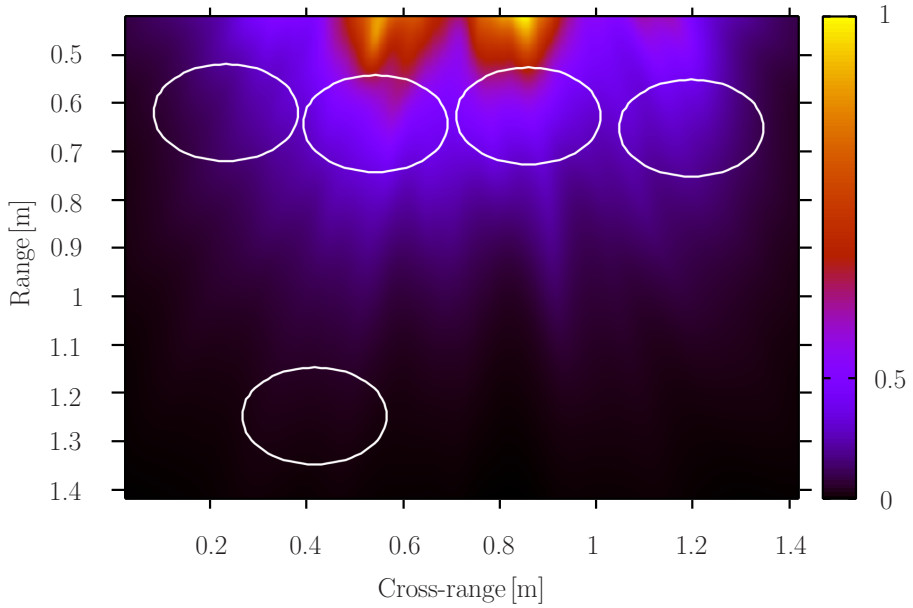

Figure 5.33: $\tilde{\mathcal{M}}(\boldsymbol{x})$ for the scenario in Section 4.1.3 using the spatiotemporally windowed UWB-MUSIC method with $\mathcal{N}_{\text{sw}} = 9$, $P = 1500$, and $\mathcal{N}^{\Theta}_{l,m}[k] \triangleq \mathcal{N}^{\Theta\div}[k]$. The ground truth location of the targets is represented by white shapes.

5.2 Resolution enhancement of TR imaging in dispersive media

In this section we perform the experiments detailed in Section 4.2. We obtain results and examine them.

5.2.1 Canonical case scenario

We perform the canonical case experiments using the muscle tissue as the background medium. First, we need to decide the time of refocusing, so that we can compare the enhancement of spatial resolution achieved with each compensation approach at that instant. Both our compensation algorithm and the compensation method in [1] are independent of the instant we decide as the time of refocusing. We record the time step when the maximum magnitude of the perturbed E_z field is reached on a selected point near a side of the target that is close to the TRA during TR forward propagation without compensation for the effects of dispersion. We select the point at $(x, y) = (127, 70)$ as the observation point. The maximum magnitude value at this point is recorded at time step 1015 of the forward propagation simulation, which corresponds to time step $(N - 1015 + 1) = 2486$ of the TR backpropagation simulation. During TR backpropagation, we record $\Xi(E_z^n)$ inside the region of interest. We identify as the time of refocusing the time step where a local minimum exists in $\Xi(E_z^n)$ near $n = 2486$. In Figure 5.34, we graph the normalised $\Xi(E_z^n)$ against n during TR backpropagation. We identify two local minima near $n = 2486$. One occurs at $n = 2286$ whereas the other minimum is at $n = 2638$. On $n = 2286$, the $|E_z|$ distribution is maximised at $(x, y) = (125, 99)$, which is far from the target. Hence, we identify the time of refocusing as $n = 2638$ for the case where the muscle tissue is used as the background.

We also perform the canonical case simulation where the lossless propagation medium is used. We decide the time of refocusing using the same process. We observe the magnitude values of the perturbed E_z field at the same point, i.e. at $(x, y) = (127, 70)$. The maximum value of $|E_z^n(127, 70)|$ is recorded at time step 762 of the forward propagation simulation, which corresponds to time step $(N - 762 + 1) = 2739$ of the TR backpropagation simulation. We plot in Figure 5.35 the normalised $\Xi(E_z^n)$ against n during TR backpropagation for the case where the lossless propagation medium is used. In this case, a local minimum

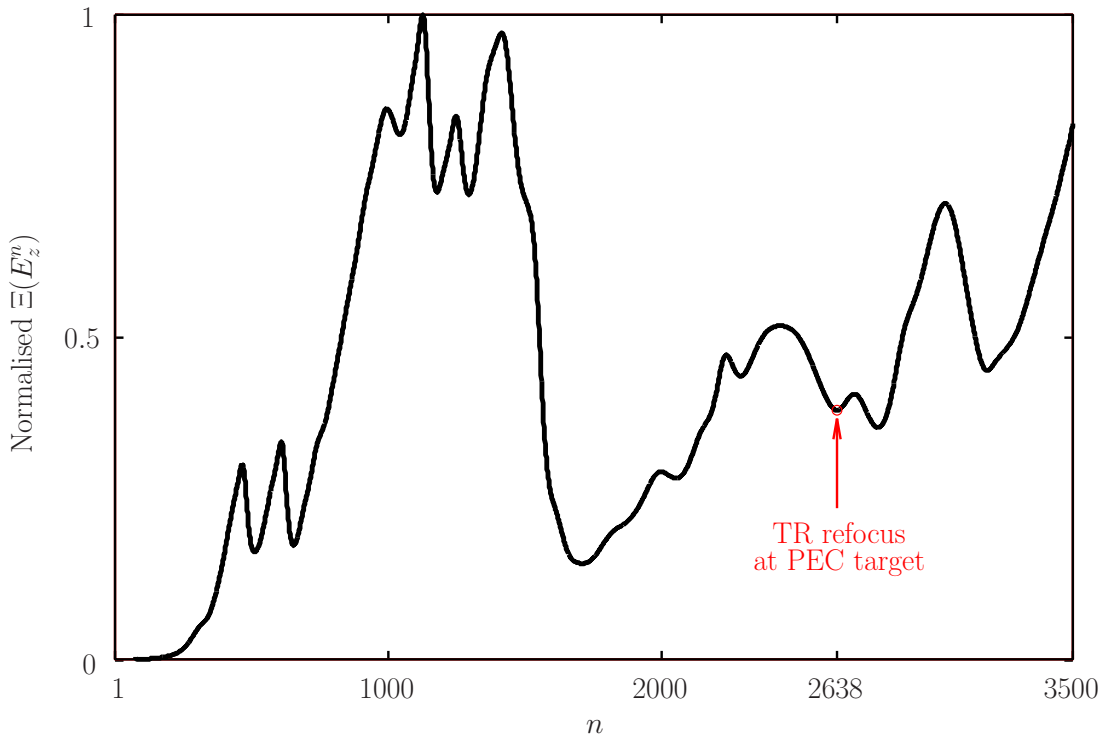

Figure 5.34: Normalised $\Xi(E_z^n)$ of the backpropagated E_z for the canonical scenario using muscle as the background medium.

exists in $\Xi(E_z^n)$ at $n = 2739$, hence we decide this instant as the time of refocusing for the case where the lossless medium is used as the background.

Figures 5.36, 5.37, and 5.38 show the normalised $|E_z|$ distribution at the time of refocusing with conventional TR imaging which does not have compensation for the effects of dispersion, our resolution enhancement approach, and the approach proposed by [1], respectively. Figure 5.39 shows the normalised $|E_z|$ distribution at the time of refocusing with conventional TR imaging for the case where the lossless propagation medium is used. As a result of using the method in [1], the peak of the $|E_z|$ signal is located near the TRA in Figure 5.38, away from the PEC scatterer. Hence, the method in [1] breaks the TR refocusing process. At the same time, the method in [1] produces a weak local maximum of $|E_z|$ near the PEC target. The magnitude of this local maximum is 11 times smaller than the peak value of $|E_z|$ inside the region of interest at the time of refocusing. We consider this weak local maximum as the point of refocusing yielded by the method in [1] when we compare the performance of the method in [1] to our approach and the conventional TR approach.

In Table 5.1, we present the locations of the TR focal points at the time of

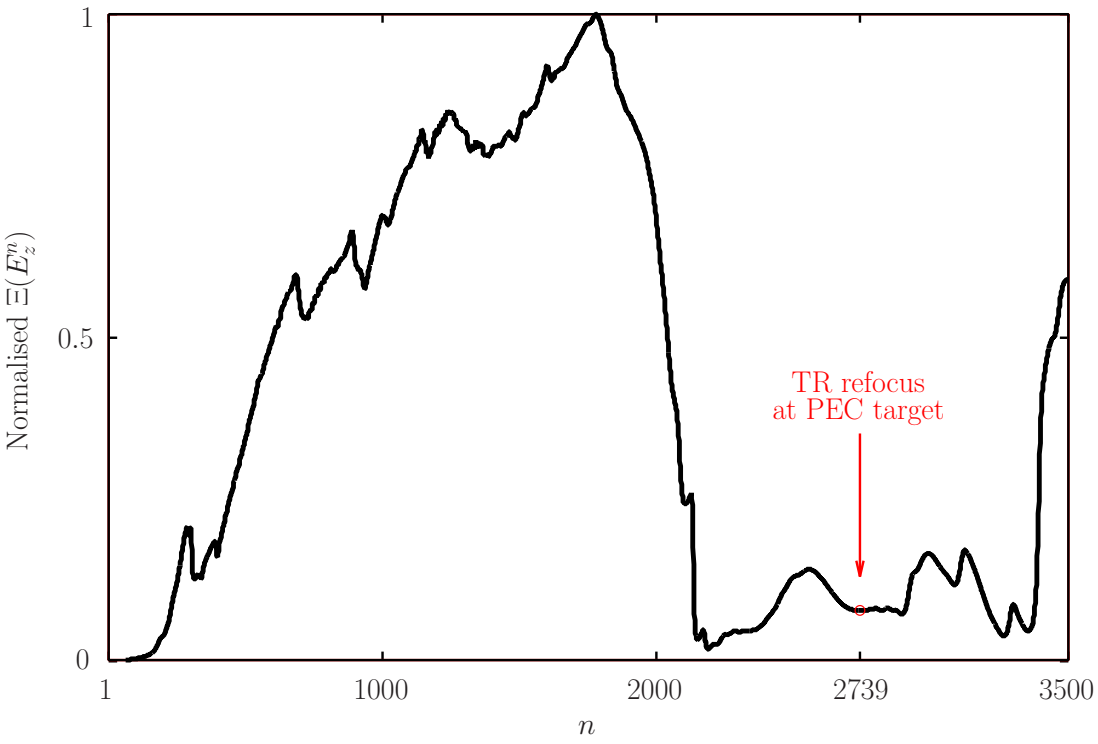

Figure 5.35: Normalised $\Xi(E_z^n)$ of the backpropagated E_z for the canonical scenario using the lossless background medium.

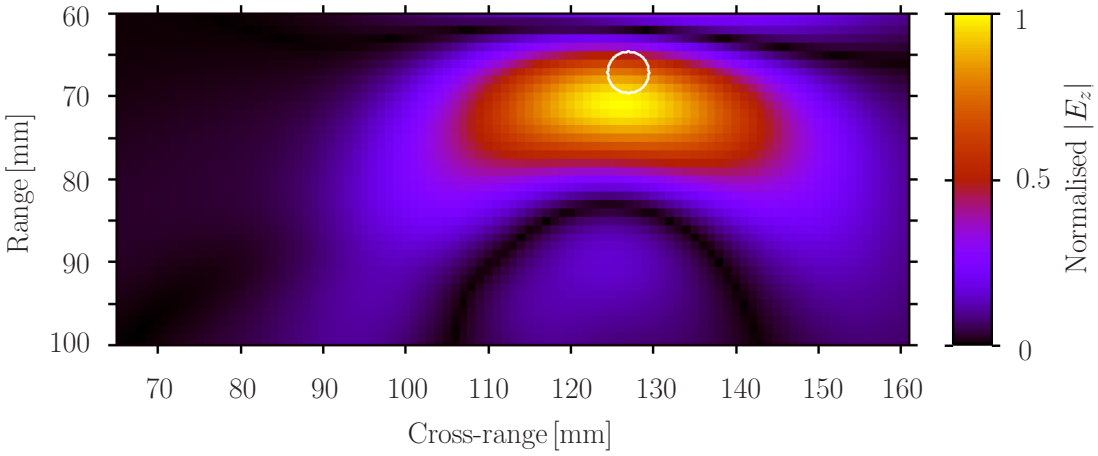

Figure 5.36: Normalised $|E_z|$ distribution inside the region of interest at the time of refocusing without applying any compensation method on the canonical scenario. The white circle represents the PEC scatterer.

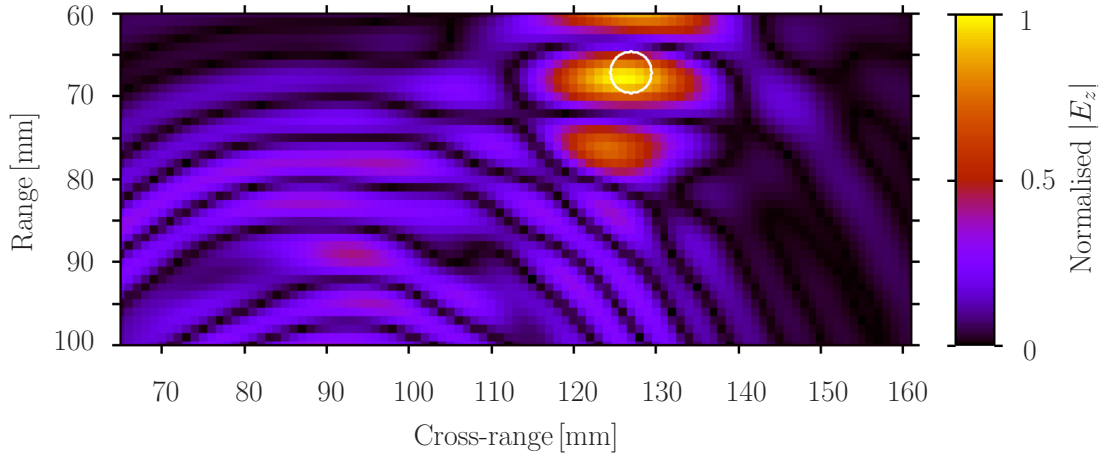

Figure 5.37: Normalised $|E_z|$ distribution inside the region of interest at the time of refocusing using our resolution enhancement approach on the canonical scenario. The white circle represents the PEC scatterer.

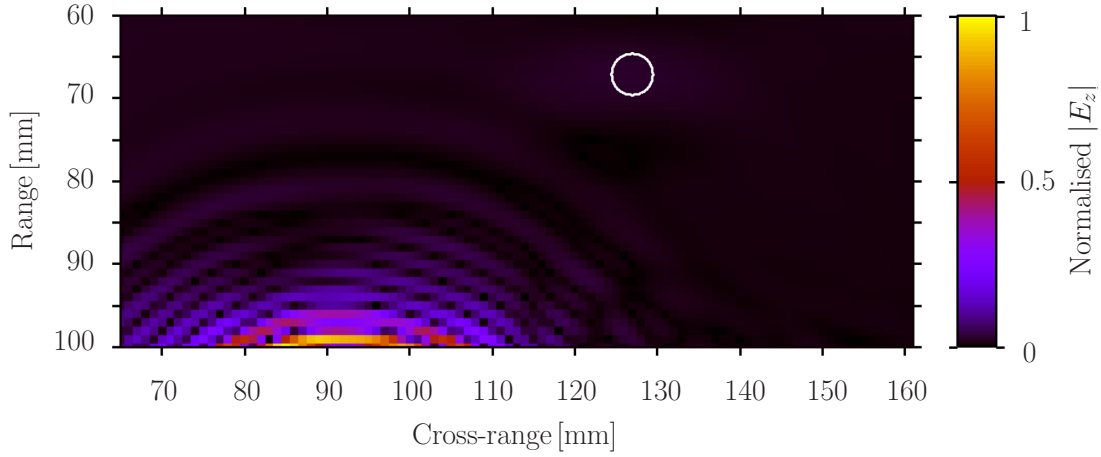

Figure 5.38: Normalised $|E_z|$ distribution inside the region of interest at the time of refocusing using the compensation method from [1] on the canonical scenario. The white circle represents the PEC scatterer.

Table 5.1: Location of refocusing centre

Method	**Background medium**	x **of focus**	y **of focus**
Conventional TR	muscle tissue	126	71
The method in [1]	muscle tissue	126	67
Our approach	muscle tissue	126	68
Conventional TR	lossless medium	126	70

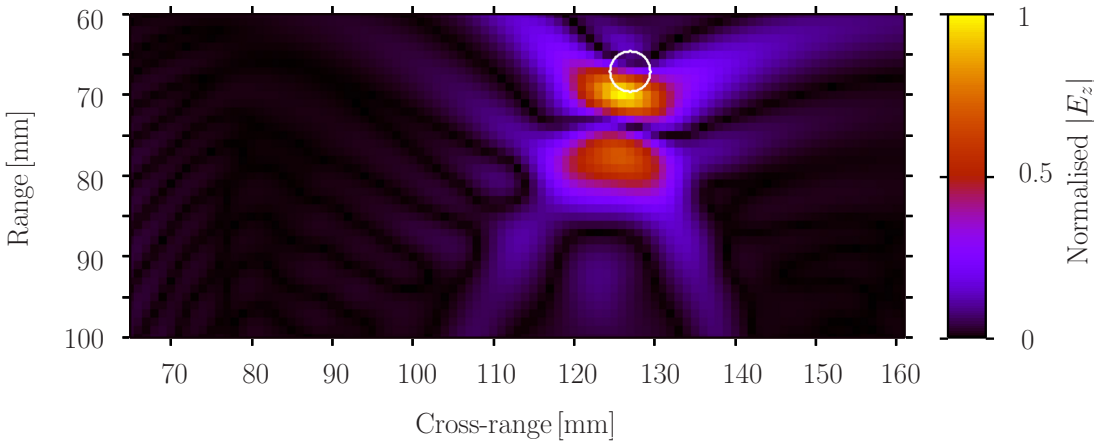

Figure 5.39: Normalised $|E_z|$ distribution inside the region of interest at the time of refocusing without applying any compensation method on the canonical scenario with the reference lossless medium instead of muscle. The white circle represents the PEC scatterer.

refocusing with the conventional TR approach (i.e. without compensation for the effects of dispersion), with applying the approach in [1], and with our resolution enhancement. We observe that both resolution enhancement methods produce a focal point which has a small offset in localisation in the range direction compared to the conventional TR refocusing. The minimum entropy criterion selects an instant when the $|E_z(x, y)|$ distribution is tightly focused, but it does not guarantee the maximum power at the focus [12]. Hence, errors in the localisation of the TR refocusing are expected [12]. For this reason, this thesis is not concerned with the small fluctuations in the accuracy of the TR refocusing in our experiments at the predetermined time of refocusing, other than merely reporting the location of the TR refocusing for each experiment. This thesis rather focuses on the improvement of the precision of the TR refocusing.

Figure 5.40 displays the normalised perturbed $|E_z|$ signals received by the interrogating TRA element with no dispersion compensation in muscle tissue and in the lossless propagation medium, and with our compensation approach. In Figure 5.40 we can see that our approach modifies the shape of the $|E_z|$ waveform relative to the non-compensated case. This modification of shape also shifts the peak of the signal slightly. We observe that our method has minimised the high frequency noise, but the signal contains significant ringing in time steps after $n = 2000$, which indicates amplification of noise in the frequency spectrum of interest. However, this ringing remains smaller in magnitude relative to the echo

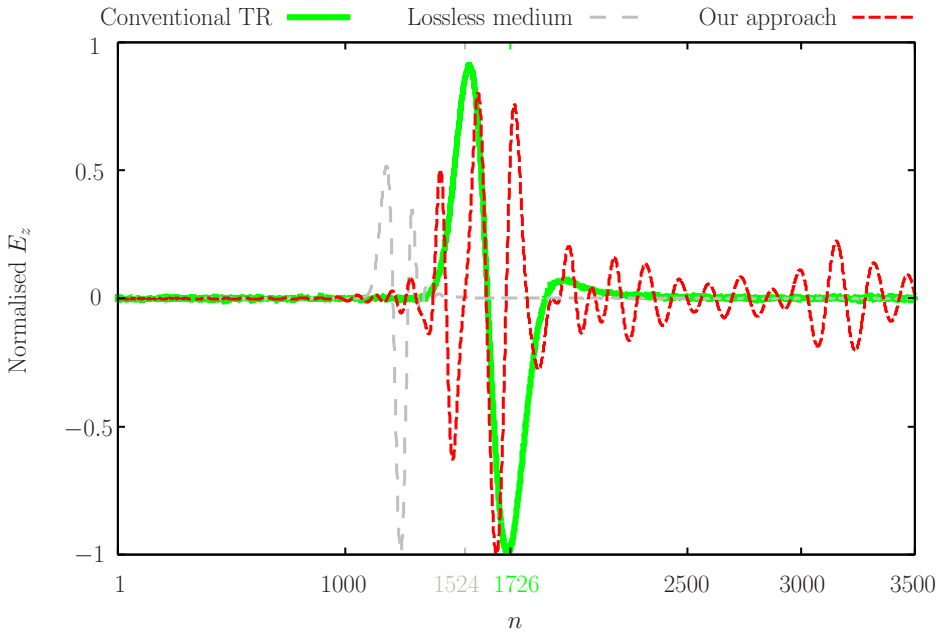

Figure 5.40: Normalised perturbed E_z signals received by the interrogating element of the TRA using no resolution enhancement and with our resolution enhancement approach.

from the scatterer.

Figure 5.41 shows the perturbed $|E_z|$ signals received by the interrogating TRA element with each method, and all the displayed signals are normalised by the peak magnitude of the lossless medium case. We note that our method generates a peak in $|E_z|$ which is 30.75 times greater than the lossless case. The investigation of the reasons for this difference in magnitudes is left as part of future work.

Figure 5.42 illustrates the resulting perturbed $|E_z|$ signals yielded by the compensation method in [1]. The signal in Figure 5.42 is dominated by high frequency noise. This is another indication that the method in [1] is unreliable and it further breaks the TR refocusing process by amplifying the high-frequency noise.

Figure 5.43 and Figure 5.44 provide cross-sections of the $|E_z|$ distribution along the cross-range and range directions respectively. Symbols R_{TR}, R_{P}, and R_{A} represent the resolution of the spatial focusing at the time of refocusing, using no resolution enhancement method (R_{TR}), using the proposed resolution enhancement approach (R_{P}), and using the method proposed by [1] (R_{A}), respectively. The symbol R_{ref} represents the resolution of the spatial focusing at the time of refocusing, using no resolution enhancement method with the reference

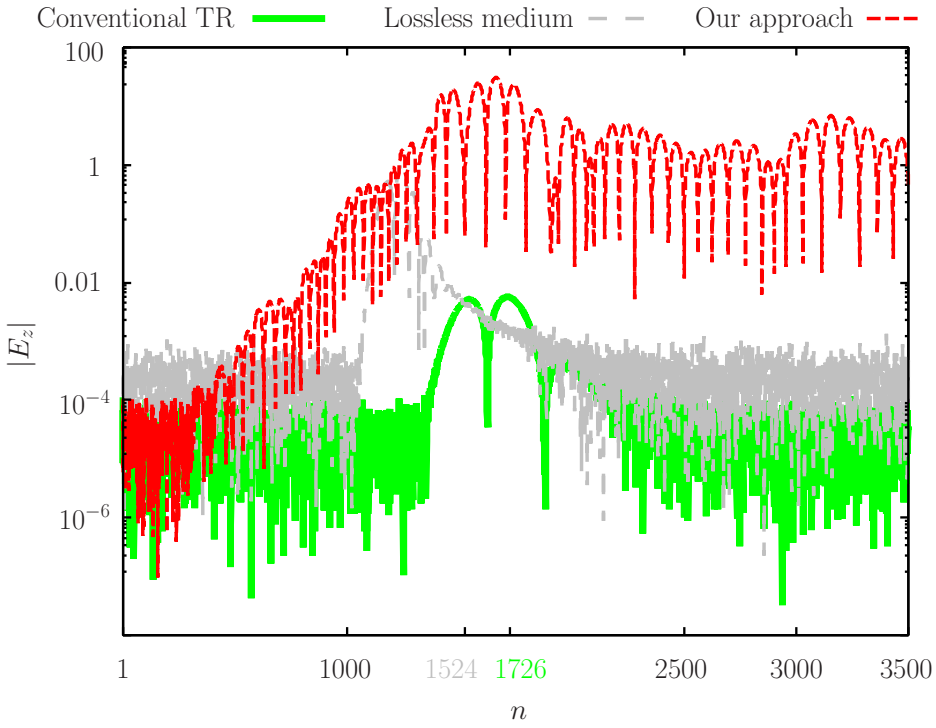

Figure 5.41: The perturbed $|E_z|$ signals received by the interrogating TRA element with no compensation used in muscle and in the lossless medium, and after compensation with our compensation approach (in muscle). All signals are normalised relative to the lossless medium case.

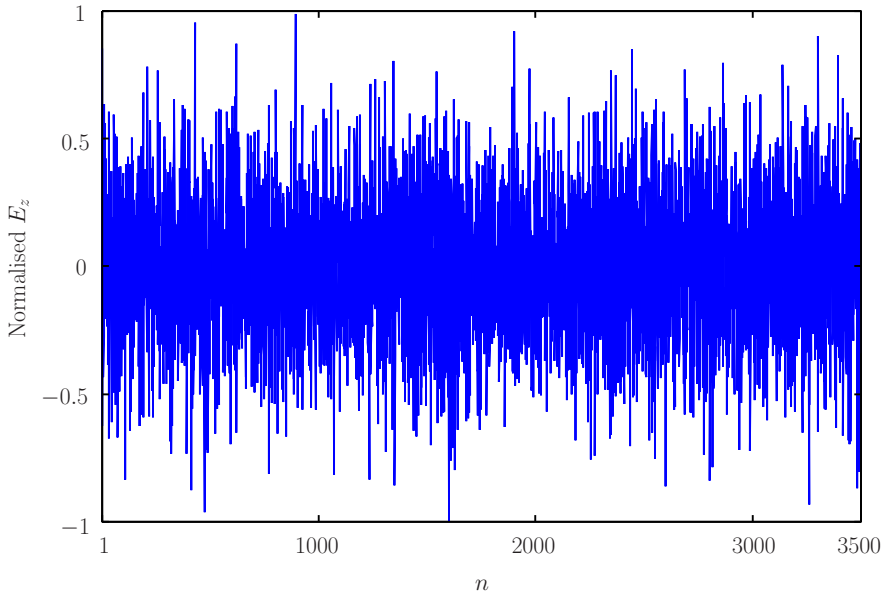

Figure 5.42: Normalised perturbed E_z signal received by the interrogating TRA element after compensation with the method in [1].

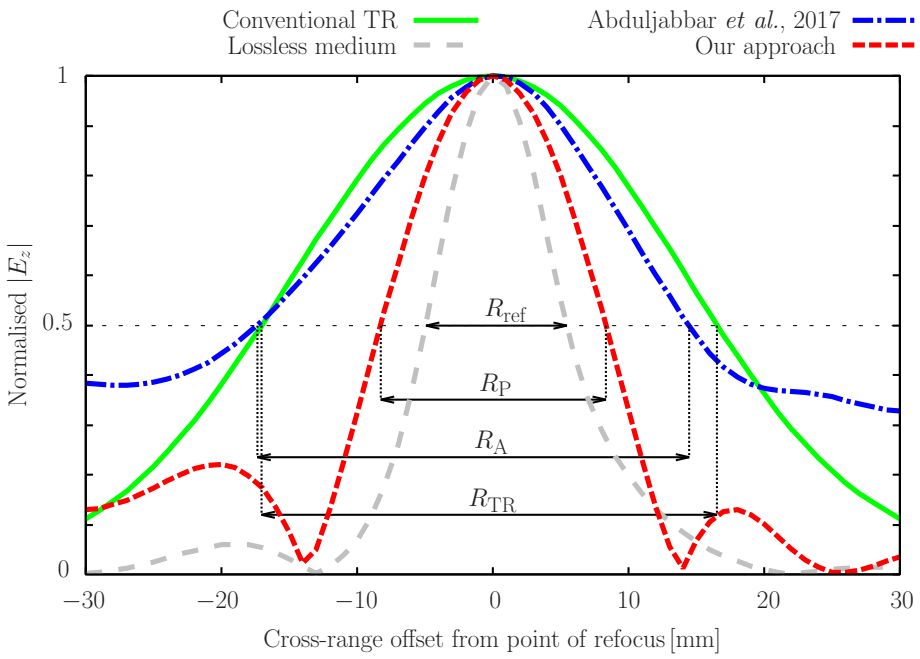

Figure 5.43: Cross-sections of the normalised $|E_z|$ distribution in the canonical case scenario along the cross-range axis of refocusing after applying our approach, the work in [1], and without applying any compensation method in muscle and in the reference lossless medium.

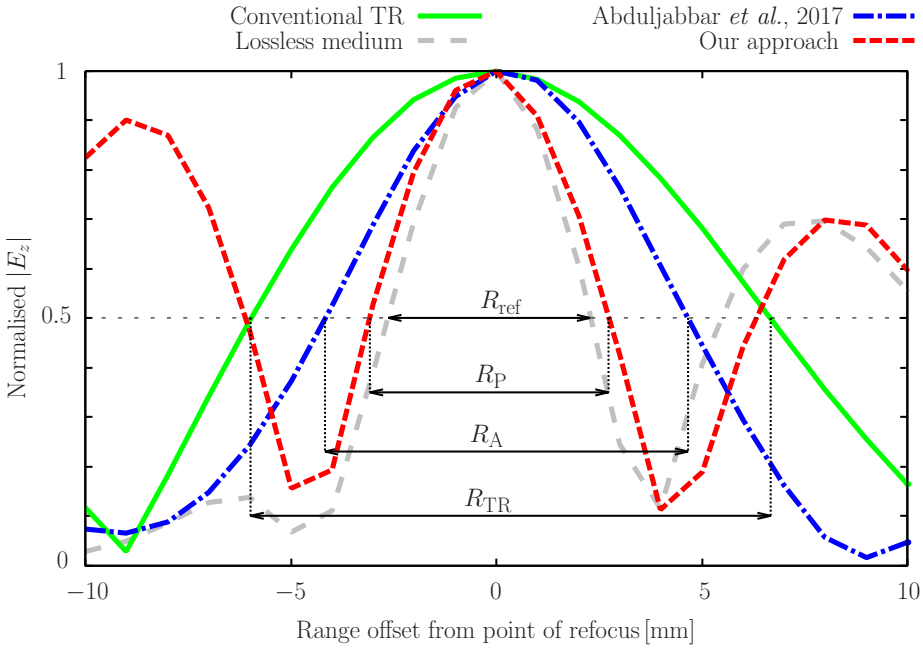

Figure 5.44: Cross-sections of the normalised $|E_z|$ distribution in the canonical case scenario along the range axis of refocusing after applying our approach, the work in [1], and without applying any compensation method in muscle and in the reference lossless medium.

lossless propagation medium described in Section 4.2.3. We measure the range and cross-range resolutions of R_{TR}, R_{P}, and R_{A} as the minimum distance between two half-maxima in $|E_z|$ nearest the point of refocusing, along the range and cross-range directions, respectively, as in [1]. Table 5.2 summarises these measurements.

Table 5.2: Resolution of spatial refocusing achieved with each method

Method	**Medium**		**Resolution**	
			Cross-range [mm]	**Range** [mm]
Conventional TR	muscle	R_{TR}	33.60	12.64
Compensation method in [1]	muscle	R_{A}	31.81	8.84
Our compensation approach	muscle	R_{P}	16.58	5.82
Conventional TR	lossless	R_{ref}	10.42	4.93

Our method results in $R_{\mathrm{TR}}/R_{\mathrm{P}} = 2.03$ times better cross-range resolution than the conventional TR approach in muscle tissue and $R_{\mathrm{P}}/R_{\mathrm{ref}} = 1.59$ times cruder cross-range resolution than with the conventional TR approach in the reference lossless medium. The method in [1] yields a cross-range resolution improvement of $R_{\mathrm{TR}}/R_{\mathrm{A}} = 1.06$ compared to the unfiltered approach. Hence, our method provides $R_{\mathrm{A}}/R_{\mathrm{P}} = 1.92$ times finer cross-range resolution of the spatial focusing at the time of refocusing than the method in [1].

Along the range direction, our method results in $R_{\mathrm{TR}}/R_{\mathrm{P}} = 2.17$ improvement than the conventional TR case. In the reference lossless medium, the refocusing resolution is better than with our approach in muscle tissue by a factor of $R_{\mathrm{P}}/R_{\mathrm{ref}} = 1.18$. The method in [1] provides a focal resolution improvement along the range direction of 1.43 compared to the unfiltered approach. Our algorithm yields a $R_{\mathrm{A}}/R_{\mathrm{P}} = 1.52$ times finer range resolution of the spatial focusing than the method proposed by [1].

5.2.2 Practical case scenario

We perform the practical case experiments. We first decide the time of TR refocusing.

5.2.2.1 2D practical case experiments

We record the time step when the maximum magnitude of the perturbed E_z is reached at the centre of the brain tumour, i.e. at $(x, y) = (170, 112)$, during TR forward propagation, without any resolution enhancement. The maximum magnitude value at this point is recorded at time step 600 of the forward propagation simulation, which corresponds to time step $(N - 600 + 1) = 3901$ of the TR backpropagation simulation. During TR backpropagation, we record $\Xi(E_z^n)$ inside the region of interest. We identify as the time of refocusing the time step $n = 3938$ where $\Xi(E_z^n)$ has a local minimum which is closest to $n = 3901$. Figure 5.45 illustrates the normalised $\Xi(E_z^n)$ values against n during TR backpropagation.

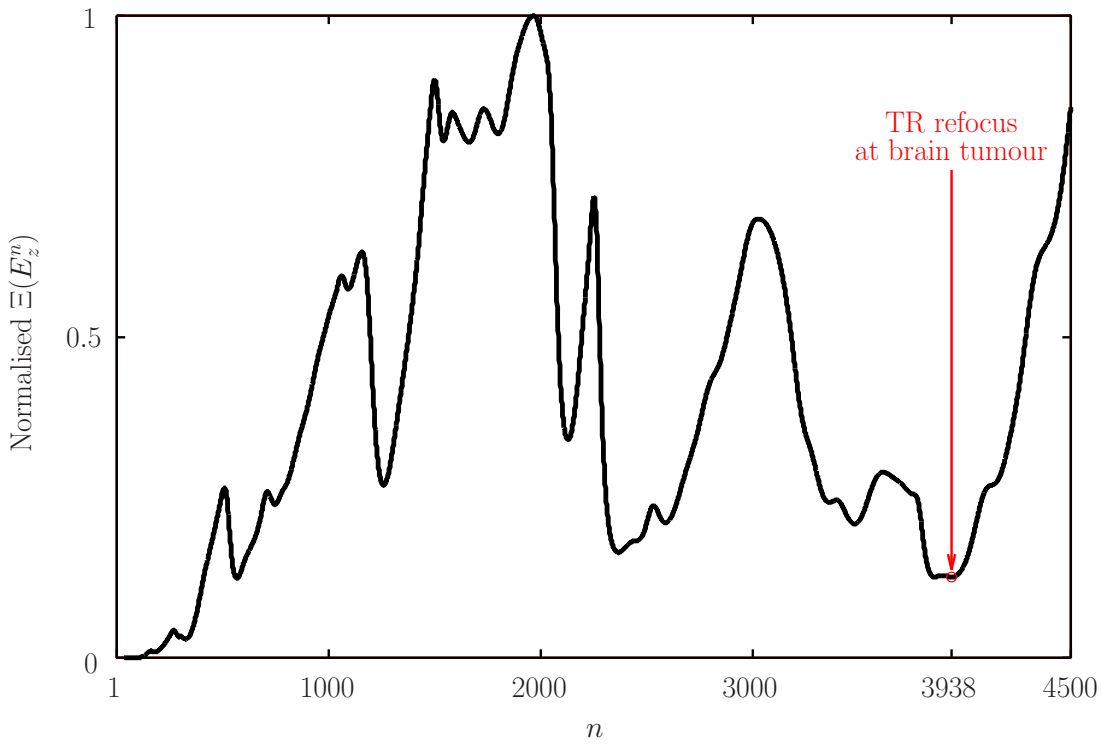

Figure 5.45: Normalised $\Xi(E_z^n)$ of the backpropagated E_z for the 2D practical experiment.

The normalised $|E_z|$ distribution at the time of refocusing with conventional TR imaging without resolution enhancement, one with our resolution enhancement approach, and one with the approach in [1] are presented in Figures 5.46, 5.47, and 5.48 respectively. Table 5.3 lists the locations of the TR focal points at the time of refocusing with no resolution enhancement and with our resolution enhancement approach.

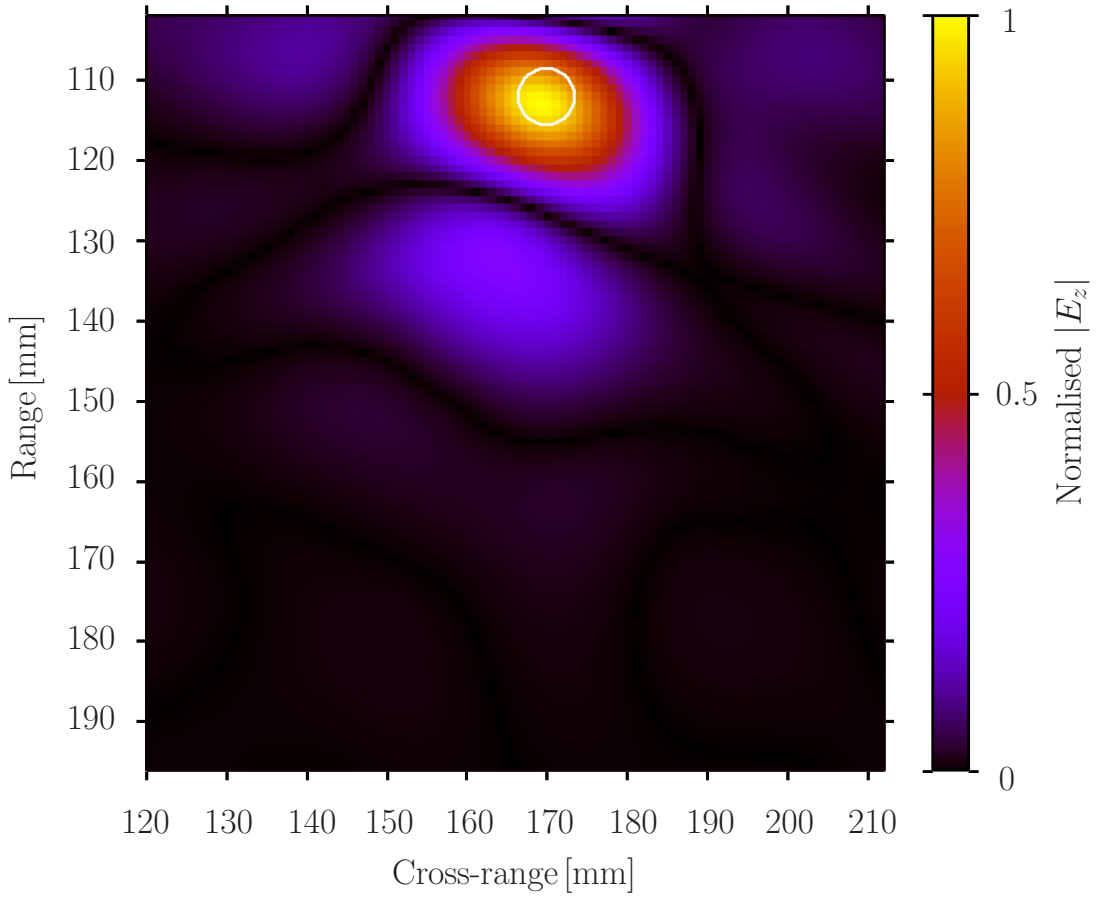

Figure 5.46: Normalised $|E_z|$ distribution inside the region of interest at the time of refocusing without applying any compensation method on the 2D practical experiment. The white circle represents the brain tumour.

Table 5.3: Location of refocusing centre

Method	x **of focus**	y **of focus**
Conventional TR	169	113
Our approach	169	114

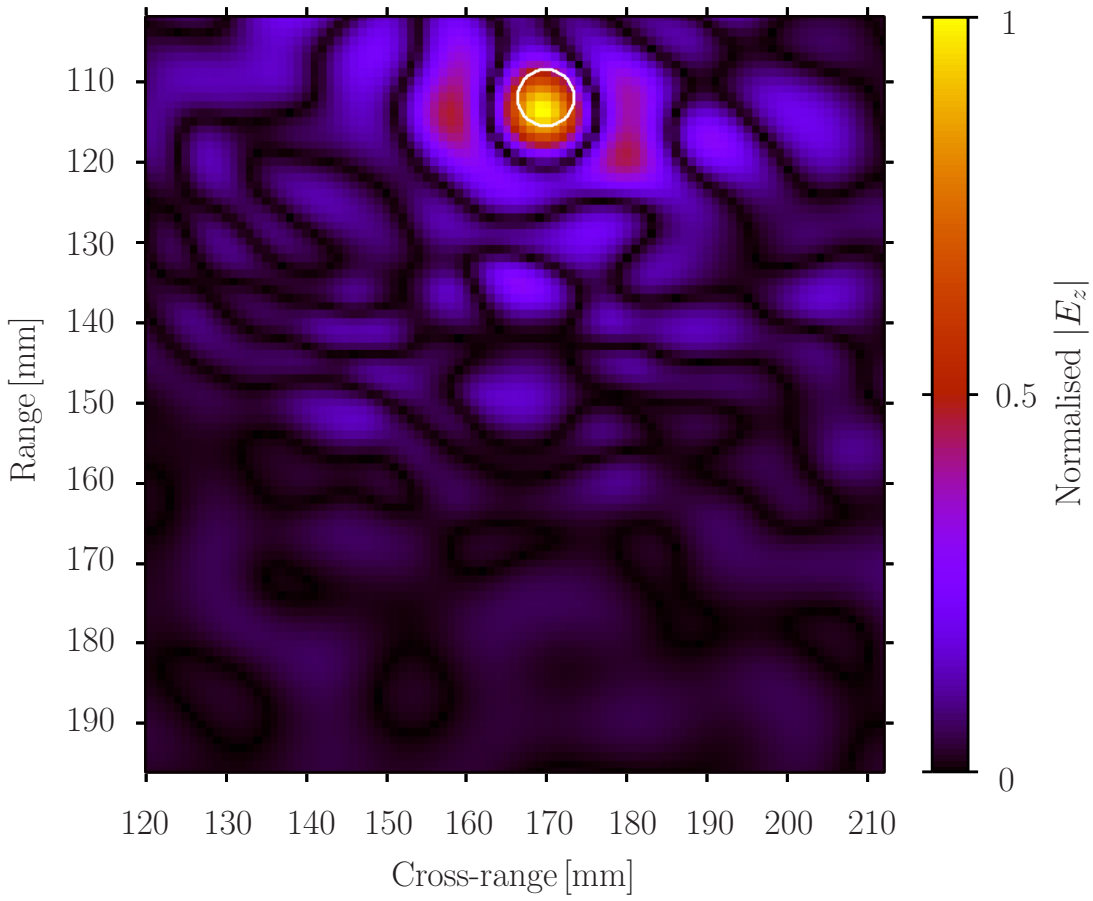

Figure 5.47: Normalised $|E_z|$ distribution inside the region of interest at the time of refocusing using our compensation approach on the 2D practical experiment. The white circle represents the brain tumour.

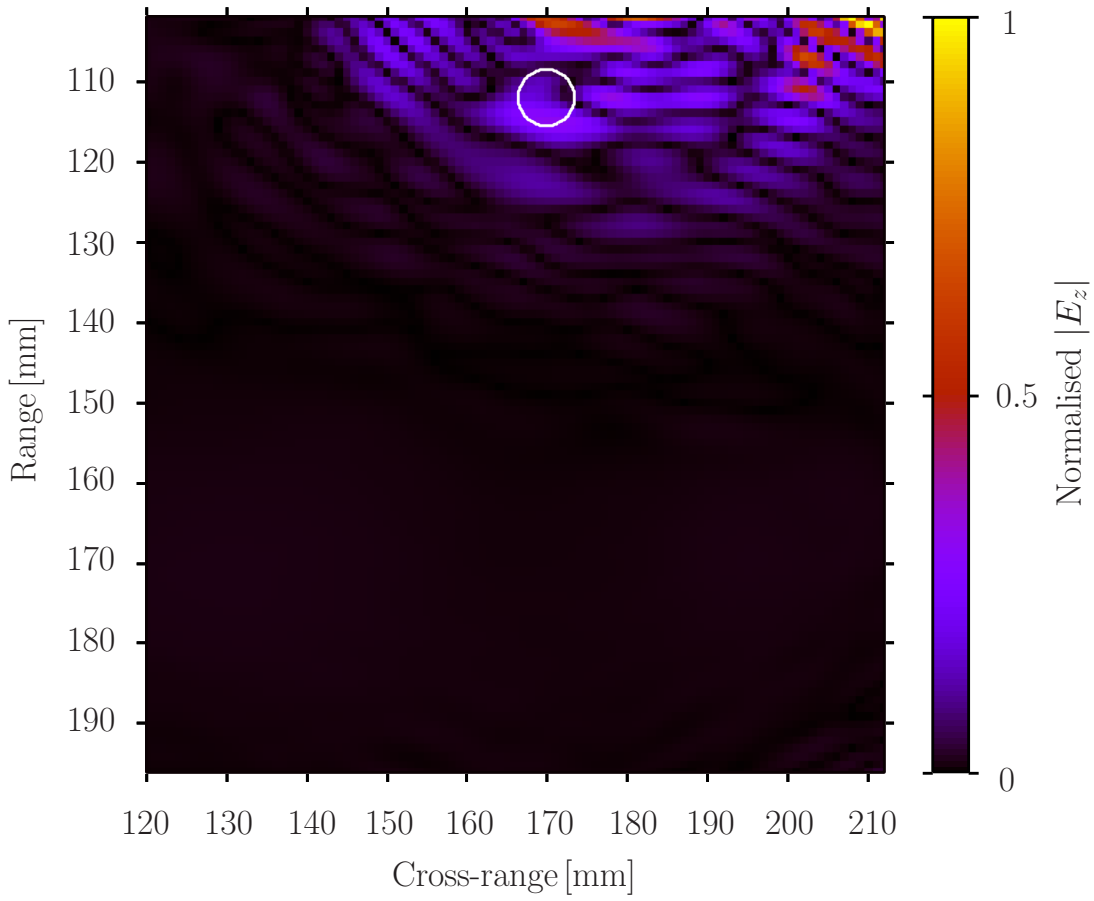

Figure 5.48: Normalised $|E_z|$ distribution inside the region of interest at the time of refocusing using the compensation method from [1] on the 2D practical experiment. The white circle represents the brain tumour.

The method in [1] failed to achieve refocusing. Instead, the TR imaging process using the method in [1] resulted in artefacts in Figure 5.48 which were higher in intensity near the TRA elements. The algorithm in [1] uses (3.35) to calculate f associated with each a_j. Thus, the method in [1] associated the non-rejected scales to a frequency range from $3.43 \cdot 10^{17}$ Hz to $2.31 \cdot 10^{19}$ Hz. This frequency range does not belong to the frequency spectrum of interest of $x(t)$. Moreover, the calculation of $\alpha(f)$ by the method in [1] is proportional to f (because [1] evaluates ϵ' and ϵ'' only at $f = f_c$). Therefore the value of $\alpha(f)$ with [1] becomes 10 orders of magnitude larger than the true value of $\alpha(f)$. Thus [1] carries out unreliable computation of $\Gamma[a_j, n]$ and of $H_s[a_j, n]$. Our proposed method associated the frequency $f_{\min}$ with scale index $j = 342$ and $f_{\max}$ with $j = 217$ and performed inverse filtering for $217 \leq j \leq 342$. Our proposed approach compensated for the losses caused by the dispersive human tissues and thus yielded more precise spatial focusing than the non-compensated TR method.

Figure 5.49 and Figure 5.50 present the cross-section of the $|E_z|$ distribution along the cross-range and range directions respectively. Along the range di-

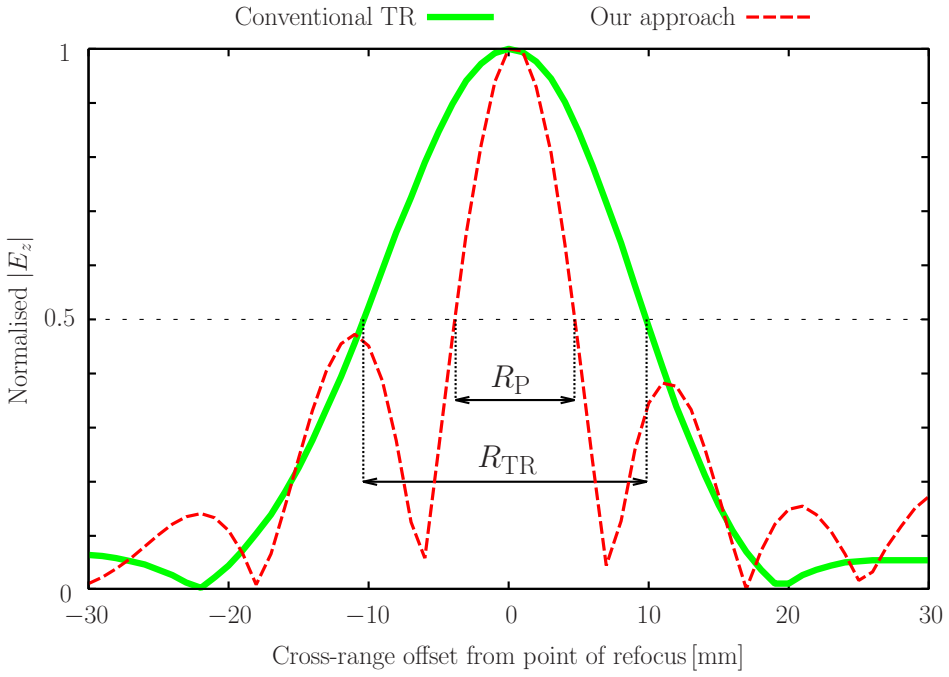

Figure 5.49: Cross-sections of the normalised $|E_z|$ distribution in the 2D practical case experiments along the cross-range axis of refocusing after applying our approach, and without applying any compensation method.

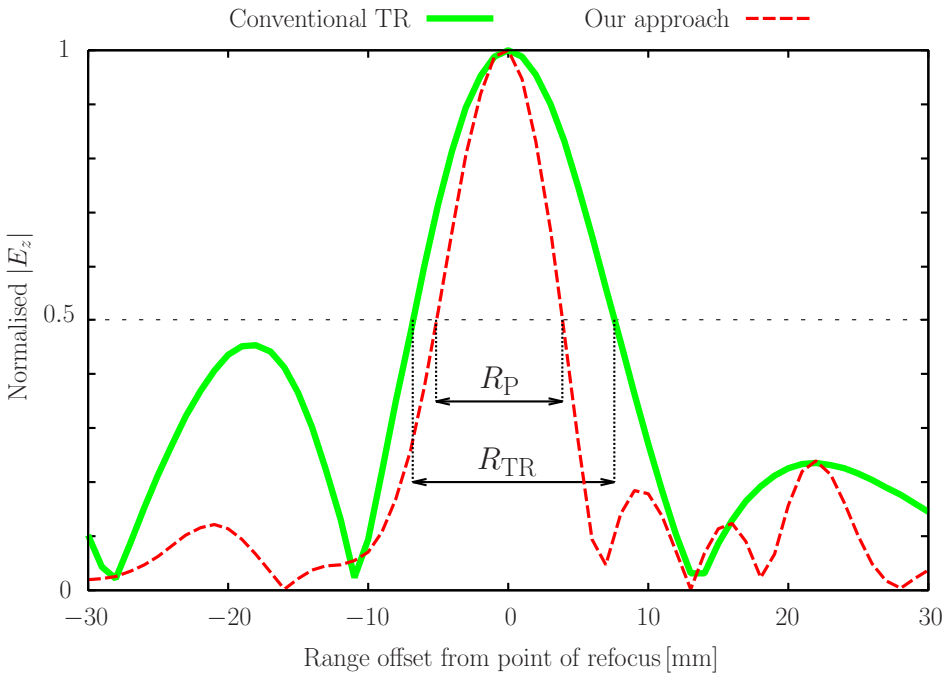

Figure 5.50: Cross-sections of the normalised $|E_z|$ distribution in the 2D practical case experiments along the range axis of refocusing after applying our approach, and without applying any compensation method.

rection, our method outperforms the conventional TR method in precision by a factor of $R_{\mathrm{TR}}/R_{\mathrm{P}} = 1.61$. Along the cross-range direction, our method provides $R_{\mathrm{TR}}/R_{\mathrm{P}} = 2.36$ times better resolution than the unfiltered TR approach. Along the cross-range direction, it is $R_{\mathrm{P}} = 8.53\,\mathrm{mm}$ and $R_{\mathrm{TR}} = 20.16\,\mathrm{mm}$. Hence, the cross-range precision of the proposed method is a factor of 1.22 coarser than the ground-truth tumour's size, whereas the precision of the conventional TR approach is 2.88 times coarser than the tumour's size. Since there is no focus from the approach in [1], we did not compare our results with the ones in [1].

5.2.2.2 3D practical case experiments

During TR backpropagation, we record $\Xi(E_z^n)$ inside the region of interest. We identify as the time of refocusing the time step $n = 2509$ where $\Xi(E_z^n)$ has a local minimum. Figure 5.51 illustrates the normalised $\Xi(E_z^n)$ values with respect to n during TR backpropagation.

The normalised $|E_z|$ distribution at the time of refocusing with conventional TR imaging without resolution enhancement, one with our resolution enhancement approach, and one with the approach in [1] are presented in Figures 5.52,

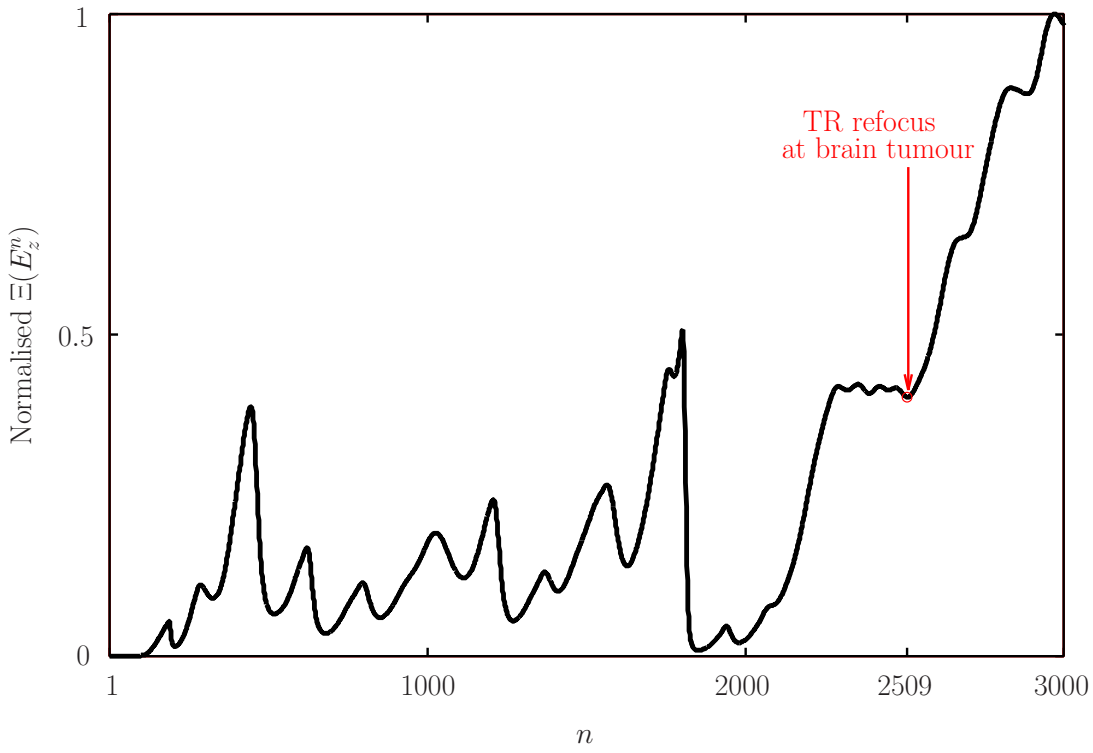

Figure 5.51: Normalised $\Xi(E_z^n)$ of the backpropagated E_z for the 3D practical experiment.

5.53, and 5.54 respectively. Table 5.4 lists the locations of the TR focal points at the time of refocusing with no resolution enhancement and with our resolution enhancement approach.

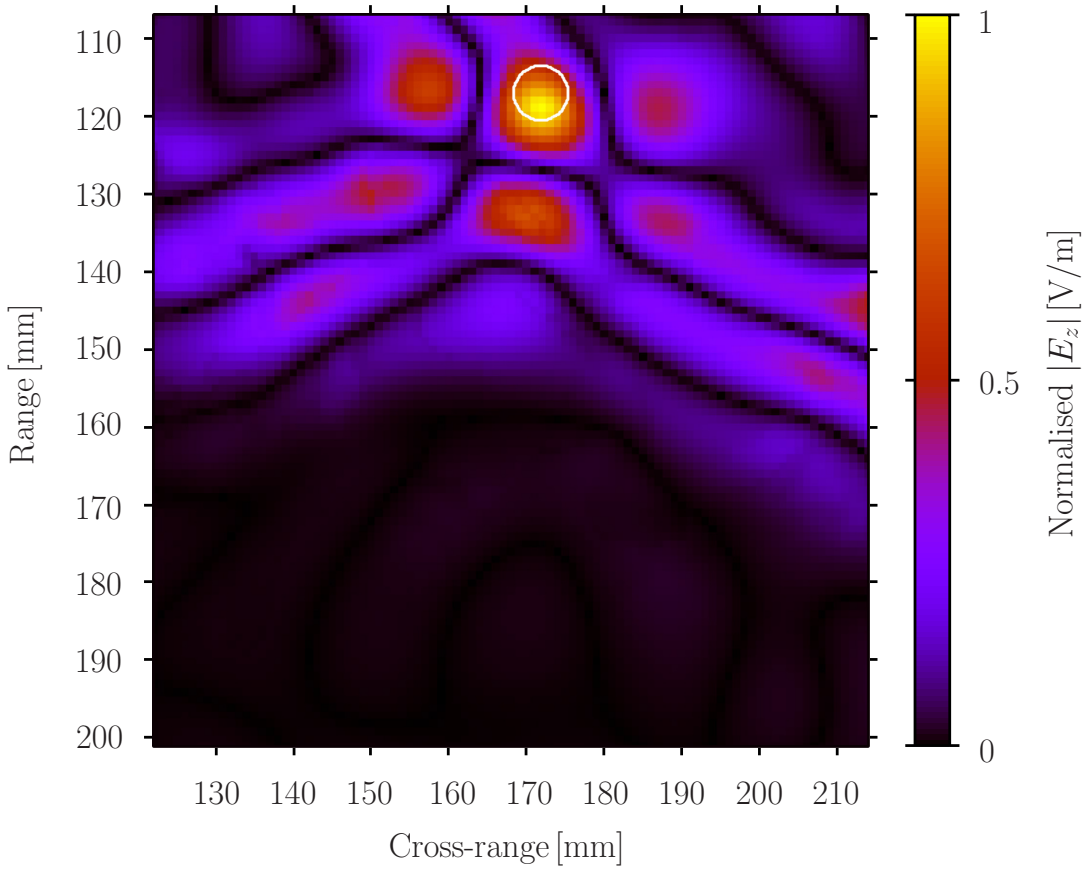

Figure 5.52: Normalised $|E_z|$ distribution inside the region of interest at the time of refocusing without applying any compensation method on the 3D practical experiment. The white circle represents the brain tumour.

Figure 5.55 and Figure 5.56 present the cross-section of the $|E_z|$ distribution along the cross-range and range directions respectively. Along the range direction, the proposed approach outperforms the conventional TR method by a factor of $R_{\mathrm{TR}}/R_{\mathrm{P}} = 1.56$. Along the cross-range direction, our method has a $R_{\mathrm{TR}}/R_{\mathrm{P}} = 1.3$ times better resolution than the unfiltered TR method. The focusing with the unfiltered TR method in the 3D experiment is more precise compared to the 2D unfiltered TR method experiment, since the existence of more multipaths in the 3D geometry improves the resolution of the TR imaging.

Along the range direction, it is $R_{\mathrm{P}} = 7.03$ mm and $R_{\mathrm{TR}} = 10.98$ mm. Hence,

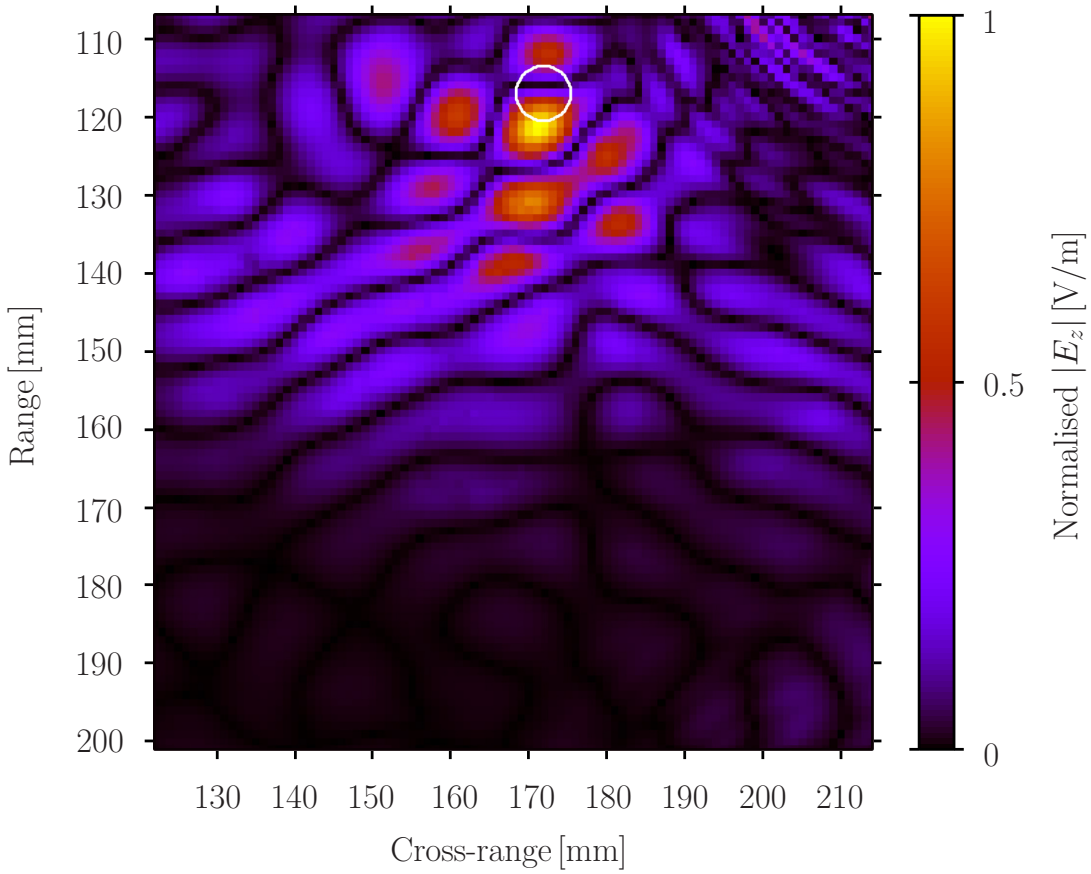

Figure 5.53: Normalised $|E_z|$ distribution inside the region of interest at the time of refocusing using our compensation approach on the 3D practical experiment. The white circle represents the brain tumour.

Table 5.4: Location of refocusing centre

Method	x **of focus**	y **of focus**
Conventional TR	172	119
Our approach	171	121

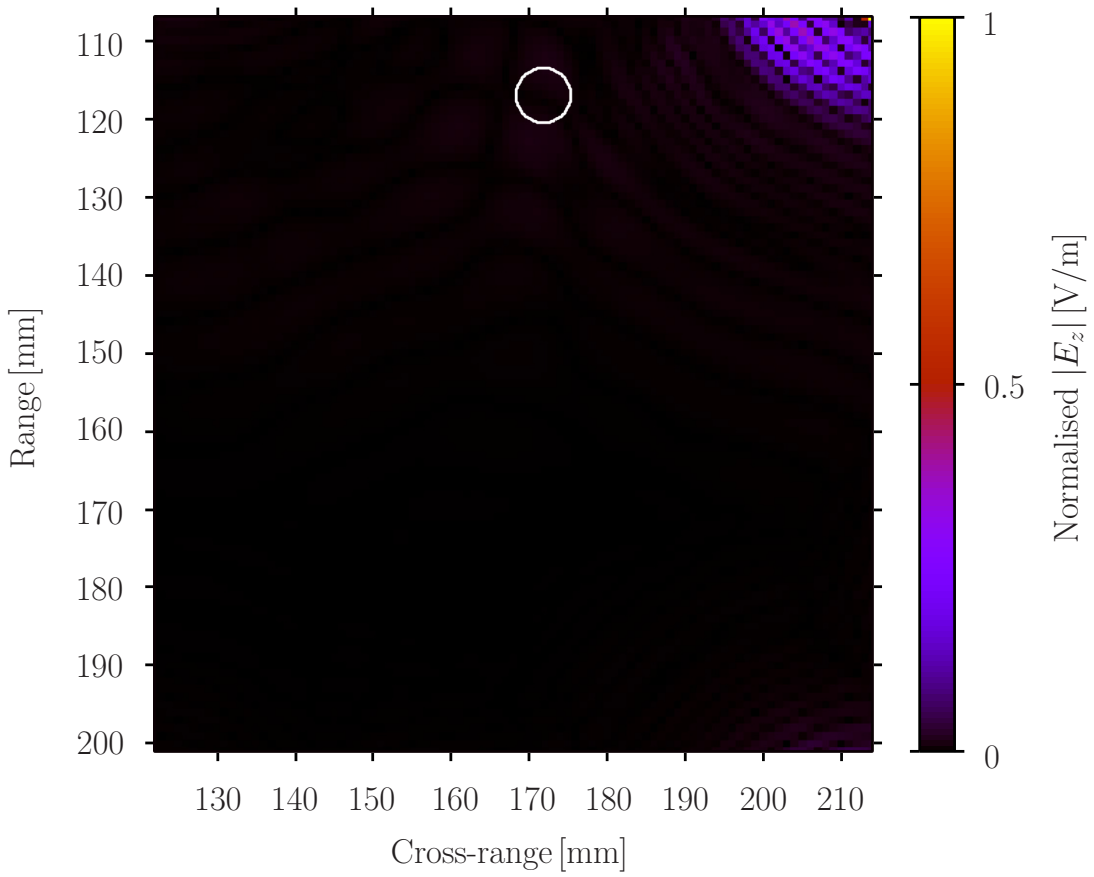

Figure 5.54: Normalised $|E_z|$ distribution inside the region of interest at the time of refocusing using the compensation method from [1] on the 3D practical experiment. The white circle represents the brain tumour.

the range precision of the proposed method is approximately equal to the ground-truth tumour's size, whereas the precision of the conventional TR approach is 1.57 times coarser than the tumour's size. Since there is no focus from the approach in [1], we did not compare the proposed approach against the results with the method in [1]. Specifically, the method in [1] resulted in artefacts in Figure 5.54 as in Section 5.2.2.1.

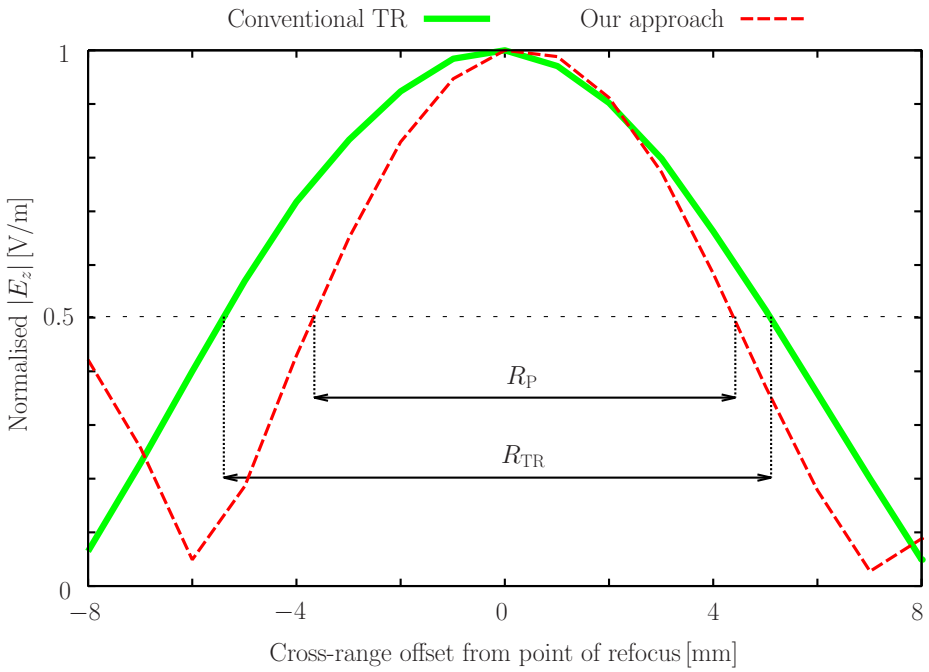

Figure 5.55: Cross-sections of the normalised $|E_z|$ distribution in the 3D practical case experiments along the cross-range axis of refocusing after applying our approach, and without applying any compensation method.

5.3 Summary

In this chapter, we performed the experiments which we laid out in Chapter 4. We presented and examined the results obtained from each experiment.

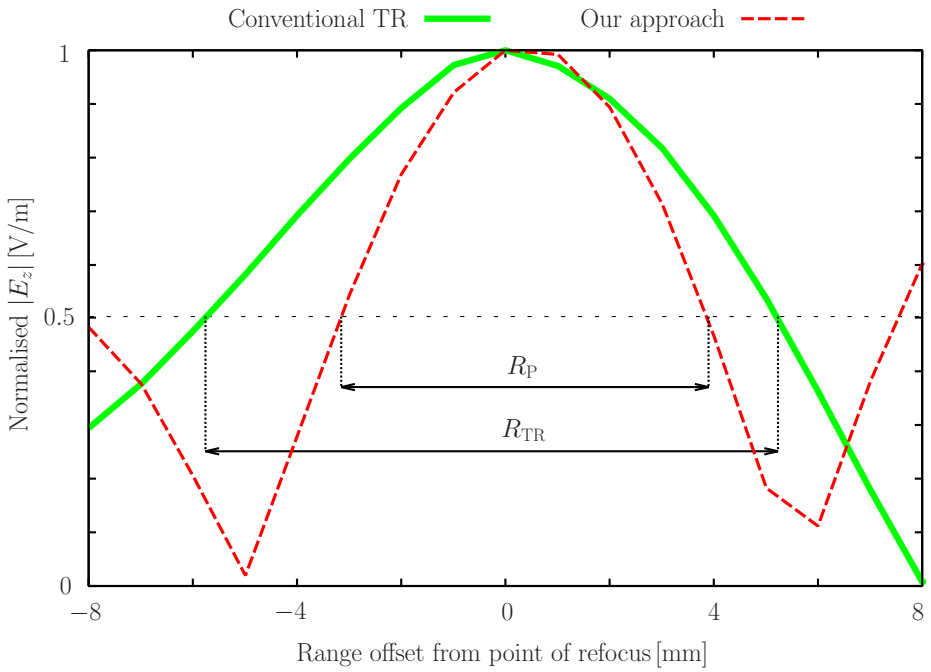

Figure 5.56: Cross-sections of the normalised $|E_z|$ distribution in the 3D practical case experiments along the range axis of refocusing after applying our approach, and without applying any compensation method.

5.3.1 Through-the-wall radar imaging of extended moving targets

We performed the canonical and practical case experiments regarding our approach for the TWRI of multiple extended moving targets. The temporal windowing of $\boldsymbol{K}_{\mathbf{d}}$ allowed the detection of moving targets which were otherwise shadowed by more dominant ones located closer to the TRA. The spatial windowing of $\boldsymbol{K}_{\mathbf{d}}$ enhanced the detection of weak targets which are roughly equidistant to the TRA in the case of multiple moving targets overlapping in the cross-range direction. The combination of spatial and temporal windowing of $\boldsymbol{K}_{\mathbf{d}}$ together with the WF-MUSIC method allowed the detection of all five extended moving targets in the practical case scenario. With the UWB-MUSIC method in [4], the detection of merely two targets was possible in the practical case scenario. The use of $\mathcal{N}^{\Theta}_{l,m}[k] \triangleq \mathcal{N}^{\Theta\Sigma}_{l,m}[k]$ rather than the conventional approaches for the determination of $\mathcal{N}^{\Theta}_{l,m}[k]$, was significant for the detection of all targets. Our approach cannot find out the approximate size of all of the targets. Consequently, it is not possible identify which part of the target is detected in $\tilde{\mathcal{M}}[\boldsymbol{x}]$. Also, our approach

cannot be used for applications where the determination of the targets' size is a requirement, such as microwave tomography applications. Further, multiple detections may correspond to one extended moving target. Our approach has the additional limitation that it may produce artefacts in the final radar image, which may affect the detection of moving targets. Also, our approach cannot determine the direction or amount of displacement of an extended moving target.

5.3.2 Resolution enhancement of TR imaging in dispersive media

We performed the experiments regarding our method for the resolution enhancement of TR imaging in dispersive media. In the canonical scenario, our approach outperformed the prior work in terms of refocusing resolution and provided resolution enhancement by a factor of 2.03 along the cross-range direction and 2.17 along the range direction relative to the conventional TR approach. Relative to the resolution of the TR refocusing in a reference lossless medium, the resolution with our approach was cruder by a factor of 1.59 in the cross-range direction and 1.18 in the range direction. In the 2D practical scenario experiments, our work located the brain tumour with 2.36 times better resolution than the conventional TR approach along the cross-range direction and 1.61 times better resolution along the range direction, while the prior work in [1] failed to locate the tumour. In the 3D practical case scenario experiments, our work located the brain tumour with 1.3 times better resolution than the conventional TR approach along the cross-range direction and 1.56 times better resolution along the range direction.

Chapter 6

Conclusions and future work

6.1 Conclusions

This thesis proposed two novel radar signal processing algorithms. One is a TR-MUSIC-based technique for the UWB TWRI of multiple extended moving targets. The other achieves the resolution enhancement of UWB TR imaging of stationary targets in dispersive environments.

6.1.1 Through-the-wall radar imaging of extended moving targets

Our method for the UWB TWRI of multiple extended moving targets performs the spatial and temporal windowing of the differential MDM. We introduced the FQ-MUSIC imaging functional to achieve radar imaging using the data contained in each spatiotemporal window. With the FQ-MUSIC imaging functional, we proposed a novel process to determine the signal subspace of each sub-differential MDM. We introduced the WF-MUSIC imaging functional to combine the radar images obtained from each sub-differential MDM and form a final radar image.

In our simulated experiments using our proposed method to TWRI of multiple extended moving targets, temporal and spatial diversity through the use of spatiotemporal windowing improved the overall imaging. The temporal windowing of each sub-differential MDM (or of the full differential MDM in the case where spatial windowing is not used) revealed targets in the final radar image otherwise obscured due to target shadowing. The spatial windowing of the full differential MDM enhanced the detection of weak targets which are roughly equidistant to

the TRA in the case of multiple moving targets overlapping in the cross-range direction. Thus, the application of spatial windowing also facilitates the visual identification of such targets in the final radar image. The application of the FQ-MUSIC imaging functional to different temporal and spatial windows achieved imaging of different extended targets, exploiting the temporal and spatial diversity of the signals in each sub-differential MDM, in addition to the wide-band content of these signals. Using the WF-MUSIC imaging functional, each pixel of the final radar images contained the strongest contributions from each temporal and spatial window and discrete frequency bins. Thus, targets which appeared in a few, or in just one spatiotemporal window, were revealed in the final radar images. Also, strong detections in at least one spatiotemporal window which appeared weak in other windows appear strong in the final radar image.

We applied our TWRI approach on a simulated practical case scenario involving five moving human-like targets hidden behind a brick wall. Our approach achieved the detection of all targets. The spatiotemporally windowed UWB-MUSIC method in [4] detected only two targets in this scenario. The use of our proposed process to determine the signal subspace of each sub-differential MDM was significant for the imaging performance of our approach. This is because the conventional approaches (the 10% method [45] and the ratios method [4]) reduced the number of targets detected in the final radar image and introduced artefacts in the final radar image.

With our approach, one target may produce multiple detections in the final radar image. Our approach cannot determine the size of targets under radar interrogation or which part of the target is detected in the final radar image. Also, the proposed approach cannot determine the direction or amount of displacement of the detected targets. One more limitation of our approach is that it produces artefacts in the final radar image. Such artefacts are introduced in individual spatiotemporal window FQ-MUSIC images due to spatial or temporal windowing of the full differential MDM and are projected in the final radar image.

6.1.2 Resolution enhancement of TR imaging in dispersive media

The TR imaging resolution is degraded in dispersive media relative to the case of lossless propagation. The method in [1] provides an adaptive-window approach

on compensating for the effects of medium dispersion using inverse filters in the wavelet domain and without requiring the realisation of prior experiments. However, the algorithm in [1] considers the electrical properties of the propagation medium only at the centre frequency of the radar system's excitation pulse. In addition, the wavelet-domain model for the attenuation used by the method in [1] does not relate the wavelet transform's scales to frequencies correctly, and is thus unreliable.

Our work corrected and improved the approach in [1]. Our algorithm for the resolution enhancement of UWB TR radar imaging employs the frequency-dependent complex permittivity of the dispersive propagation medium across the *whole* spectrum of interest, for the computation of the attenuation which the interrogating UWB pulse undergoes during TR forward propagation. Also, our algorithm introduced a smart selection of wavelet scales on which to obviate the inverse filtering process.

We simulated a practical case scenario involving a brain tumour in the head of the DHP as the target of the TR imaging. In this scenario, our proposed approach achieved a better cross-range resolution of the TR imaging by a factor of 1.3 and a better range resolution by a factor of 1.56 relative to the conventional TR approach. The approach in [1] failed to achieve refocusing in this scenario.

We also simulated a canonical case scenario involving a PEC target and homogeneous dispersive muscle tissue as the propagation medium. The approach in [1] degraded the refocusing performance of the TR method by producing a weak refocusing in this scenario. In this canonical case scenario, our proposed algorithm achieved better cross-range resolution of the TR imaging by a factor of 2.03 and better range resolution by a factor of 2.17 relative to the conventional TR method. Also, in this scenario, the refocusing produced with our approach had 1.92 times better cross-range resolution and 1.52 times better range resolution compared to the weak refocusing produced by the approach in [1].

However, the magnitude of $|E_z|$ with our method was 30.75 times greater than the lossless case. We speculate that the reason for this over-amplification of $|E_z|$ is due to our method employing the wavelet transform to perform the inverse filtering for amplification: The quantity $\gamma(f,t)$ is a function of both frequency and time. $\gamma(f_0,t)$ is the attenuation that the single frequency f_0 undergoes with respect to t. We model $\gamma(f_0,t)$ in the wavelet domain as $\Gamma(a_j,t)$. $\Gamma(a_j,t)$ is not a function depending on f, but rather on a_j. While a_j can be associated with

one equivalent Fourier frequency, the contents of $\Gamma(a_j, t)$ do not contain a single frequency for any specific a_j. Therefore, when we amplify $X[a_j, n]$, in reality we amplify multiple frequencies and adjacent scales can share frequency content. Hence, we surmise that the reason for the over-amplification is due to multiple frequencies being amplified multiple times, each time in each nearby wavelet scale. A meticulous investigation of the reasons for the over-amplification of $x[n]$ using our approach is left as part of future work.

6.2 Future work

One limitation the work in this thesis has is that it does not take into account effects due to finite dipole size or mutual coupling between the TRA elements, as the focus is more on the algorithm development. As part of future work based upon this thesis, more realistic simulation models can be developed to assess any possible impact these effects have on the radar imaging. This may include the simulation of realistic antennas for the TRAs or the realisation of practical experiments with actual antennas. Future work could also extend our proposed algorithms to perform radar imaging in three spatial dimensions. Such an extension of our work could be computation-expensive. Hence, special consideration may be given on the optimisation of our methods' usage of computational resources. Also, both our proposed algorithms assume a stationary TRA. Further research can investigate modifications of our algorithms for cases where the TRA elements are moving, e.g. Synthetic Aperture Radar (SAR), GPR, or tactical TWRI scenarios. Furthermore, we propose a list of future studies based upon this thesis, which we outline below in this section.

6.2.1 Through-the-wall radar imaging of extended moving targets

This thesis' proposed approach for the radar imaging of multiple extended moving targets produced encouraging imaging results for targets which are hard to detect using other approaches such as the UWB-MUSIC approach. Nevertheless, there are no elements in our research to suggest that this proposed approach is statistically stable. Hence, in addition to the aforementioned discussion on future studies, future experiments can introduce random dispersive media parameters (media randomness) to verify whether our proposed approach indeed lacks statistical stability. One more limitation of our TWRI approach for multiple extended moving targets is that it produces artefacts in the final radar image. Work to ameliorate this limitation needs to be carried out in the future.

Moreover, our TWRI method for multiple extended moving targets may yield multiple detections corresponding to one target in $\tilde{\mathcal{M}}[\boldsymbol{x}]$. This hinders the identification of the total number of targets and makes the obtainment of situational awareness more difficult for the operator of our proposed TWRI method. The design of a process to associate each detection in $\tilde{\mathcal{M}}[\boldsymbol{x}]$ to specific targets can be part of future work. Also, the development of Moving Target Indication (MTI) and moving target tracking techniques based upon our work can be investigated as part of future research.

In our simulations where we applied our proposed TWRI method for multiple extended moving targets, we could not extract any information on the approximate shape or size of the extended targets. Our relevant experiments used a limited number of TRA elements due to lack of additional computational resources. As a consequence, the size of the signal and null subspaces in our experiments was also limited. Future work needs to examine the imaging performance of our approach using TRAs containing significantly more transmit/receive elements and whether or not the approximate shape or size of the targets can be deduced in these cases.

The practical case scenario in Section 4.1.3 consists of a simplistic model for the human targets. Further study can incorporate cross sections of a realistic DHP in place of the simplistic human target model used in Section 4.1.3. This way, a more accurate assessment of our TWRI method for multiple extended moving targets can be made. Furthermore, the wave propagation environments in typical TWRI scenarios are lossy and noisy in most real-life situations. Therefore,

future work based on our TWRI approach for multiple extended moving targets can examine the performance of our approach in noisy environments and the application of loss compensation techniques.

Currently, our TWRI approach for multiple moving targets requires the manual adjustment of the fixed parameters $\mathcal{N}_{\text{sw}}$ and P for the spatial and temporal windows. Future work also includes the optimisation or automatic adjustment of the parameters $\mathcal{N}_{\text{sw}}$, P for the spatiotemporal windows. Also, the development of variable-size spatiotemporal window techniques can be investigated.

6.2.2 Resolution enhancement of TR imaging in dispersive media

Our method for the resolution enhancement of the UWB TR radar imaging in dispersive media uses the complex Morlet wavelet function for the DTWT of the signals received by the TRA. As future research, the performance of our resolution enhancement method can be examined with different wavelet functions as the analysing wavelet for the inverse filters.

To construct the inverse filters $H_{\text{s}}[a_j, n]$ in inhomogeneous scenarios, our work uses the complex permittivity of the dominant medium in the calculation of Γ. Our work defines the dominant medium as the medium which occupies the largest area of the propagation space. Future extensions of our study could examine the imaging performance of our resolution enhancement algorithm when using other criteria for the selection of the dominant medium.

Our work applies the inverse filters on the signals received by the TRA to compensate for the effects of the losses which these signals undergo during the TR forward propagation. After the inverse filtering is applied on the received signals, these compensated signals are time-reversed and backpropagated collectively into the dispersive medium. However, these time-reversed signals undergo additional attenuation during the TR backpropagation, as the waves travel in the same dispersive medium. Works [16, 71] take into consideration the attenuation during backpropagation and apply additional compensation for the attenuation assuming a stationary medium. On the contrary, our work, as well as the work in [1] do not compensate for the effects of the attenuation that affects the backpropagating waves. Future work based upon on our research could investigate the additional compensation for the effects of the attenuation that backpropagating

time-reversed signals undergo.

In this thesis, we applied our TR imaging resolution enhancement approach on single cylindrical and spherical stationary targets. Our results are encouraging and can be followed by experiments involving single or multiple targets of various shapes and sizes placed in varied distances relative to each other and to the TRA. In this way, we can further examine the merit of our approach in terms of resolution enhancement of the TR radar imaging. Future work can also focus on applying our resolution enhancement approach on TR-based radar imaging of moving targets. Future studies can also investigate the applicability and imaging performance of our resolution enhancement approach on more TR-based techniques, such as the DORT, Time Reversal MUSIC (TR-MUSIC) and UWB-MUSIC imaging methods.

Also, the statistical stability of the proposed approach can be examined. The experiments considered in this thesis did not consider random media. Future work can further test the imaging performance of our approach when random dispersive media parameters are introduced, to explore whether the proposed approach is statistically stable.

Finally, future research needs to carry out a rigorous investigation on why the canonical experiment for our proposed approach resulted to a larger signal magnitude after the inverse filtering than the corresponding lossless case. If future research obtains a definite answer to this question, then further study may examine the use of our approach for dispersion compensation applications beyond the context of TR radar imaging.

Bibliography

[1] A. M. Abduljabbar, M. E. Yavuz, F. Costen, R. Himeno, and H. Yokota, "Continuous wavelet transform-based frequency dispersion compensation method for electromagnetic time-reversal imaging," *IEEE Transactions on Antennas and Propagation*, vol. 65, pp. 1321–1329, Mar. 2017.

[2] L. El Sahmarany, L. Berry, N. Ravot, F. Auzanneau, and P. Bonnet, "Time reversal for soft faults diagnosis in wire networks," *Progress in Electromagnetics Research M*, vol. 31, pp. 45–58, 2013.

[3] V. R. N. Santos and F. L. Teixeira, "Application of time-reversal-based processing techniques to enhance detection of GPR targets," *Journal of Applied Geophysics*, vol. 146, pp. 80 – 94, 2017.

[4] V. C. Odedo, M. E. Yavuz, F. Costen, R. Himeno, and H. Yokota, "Time reversal technique based on spatiotemporal windows for through the wall imaging," *IEEE Transactions on Antennas and Propagation*, vol. 65, pp. 3065–3072, June 2017.

[5] C. Zhang, Y. Kuga, and A. Ishimaru, "Hard-wall radar imaging: Localization of objects shadowed by metallic walls with MIMO radar," *IEEE Transactions on Antennas and Propagation*, vol. 66, pp. 4240–4251, Aug. 2018.

[6] R. C. Qiu, C. Zhou, N. Guo, and J. Q. Zhang, "Time reversal with MISO for ultrawideband communications: Experimental results," *IEEE Antennas and Wireless Propagation Letters*, vol. 5, pp. 269–273, 2006.

[7] Y. Chen, Y. Yang, F. Han, and K. J. R. Liu, "Time-reversal wideband communications," *IEEE Signal Processing Letters*, vol. 20, pp. 1219–1222, Dec. 2013.

[8] H. T. Nguyen, I. Z. Kovcs, and P. C. F. Eggers, "A time reversal transmission approach for multiuser UWB communications," *IEEE Transactions on Antennas and Propagation*, vol. 54, pp. 3216–3224, Nov. 2006.

[9] S. Mukherjee, L. Udpa, S. Udpa, E. J. Rothwell, and Y. Deng, "A time reversal-based microwave imaging system for detection of breast tumors," *IEEE Transactions on Microwave Theory and Techniques*, vol. 67, pp. 2062–2075, May 2019.

[10] P. Takook, H. Dobsicek Trefna, X. Zeng, A. Fhager, and M. Persson, "A computational study using time reversal focusing for hyperthermia treatment planning," *Progress in Electromagnetics Research B*, vol. 73, pp. 117–130, 2017.

[11] M. D. Hossain and A. S. Mohan, "Cancer detection in highly dense breasts using coherently focused time-reversal microwave imaging," *IEEE Transactions on Computational Imaging*, vol. 3, no. 4, pp. 928–939, 2017.

[12] P. Kosmas and C. M. Rappaport, "Time reversal with the FDTD method for microwave breast cancer detection," *IEEE Transactions on Microwave Theory and Techniques*, vol. 53, pp. 2317–2323, July 2005.

[13] P. Kosmas and C. M. Rappaport, "A matched-filter FDTD-based time reversal approach for microwave breast cancer detection," *IEEE Transactions on Antennas and Propagation*, vol. 54, no. 4, pp. 1257–1264, 2006.

[14] M. D. Hossain, A. S. Mohan, and M. J. Abedin, "Beamspace time-reversal microwave imaging for breast cancer detection," *IEEE Antennas and Wireless Propagation Letters*, vol. 12, pp. 241–244, 2013.

[15] M. E. Yavuz and F. L. Teixeira, "Full time-domain DORT for ultrawideband electromagnetic fields in dispersive, random inhomogeneous media," *IEEE Transactions on Antennas and Propagation*, vol. 54, pp. 2305–2315, Aug. 2006.

[16] M. E. Yavuz and F. L. Teixeira, "Frequency dispersion compensation in time reversal techniques for UWB electromagnetic waves," *IEEE Geoscience and Remote Sensing Letters*, vol. 2, pp. 233–237, Apr. 2005.

[17] C. Debes, J. Hahn, A. M. Zoubir, and M. G. Amin, "Target discrimination and classification in through-the-wall radar imaging," *IEEE Transactions on Signal Processing*, vol. 59, no. 10, pp. 4664–4676, 2011.

[18] S. Guo, G. Cui, L. Kong, and X. Yang, "An imaging dictionary based multipath suppression algorithm for through-wall radar imaging," *IEEE Transactions on Aerospace and Electronic Systems*, vol. 54, no. 1, pp. 269–283, 2017.

[19] S. Guo, G. Cui, L. Kong, Y. Song, and X. Yang, "Multipath analysis and exploitation for MIMO through-the-wall imaging radar," *IEEE Journal of Selected Topics in Applied Earth Observations and Remote Sensing*, vol. 11, no. 10, pp. 3721–3731, 2018.

[20] L. Qu, X. Cheng, Y. Sun, and T. Yang, "Compressive sensing-based two-dimensional diffraction tomographic algorithm for through-the-wall radar imaging," in *2018 Progress In Electromagnetics Research Symposium (PIERS-Toyama)*, pp. 2384–2388, IEEE, 2018.

[21] E. J. Baranoski, "Through-wall imaging: Historical perspective and future directions," *Journal of the Franklin Institute*, vol. 345, no. 6, pp. 556–569, 2008.

[22] M. Wang, G. Cui, L. Kong, and X. Yang, "First-order rear-wall multipath positioning and suppression for through-wall imaging radar," *IEEE Sensors Journal*, vol. 18, no. 20, pp. 8261–8274, 2018.

[23] G. Gennarelli and F. Soldovieri, "Radar imaging through cinderblock walls: Achievable performance by a model-corrected linear inverse scattering approach," *IEEE Transactions on Geoscience and Remote Sensing*, vol. 52, no. 10, pp. 6738–6749, 2014.

[24] M. G. Amin, *Through-the-wall radar imaging*. CRC press, 2017.

[25] F. Soldovieri, F. Ahmad, and R. Solimene, "Validation of microwave tomographic inverse scattering approach via through-the-wall experiments in semicontrolled conditions," *IEEE Geoscience and Remote Sensing Letters*, vol. 8, no. 1, pp. 123–127, 2010.

[26] M. Ascione, A. Buonanno, M. D'Urso, L. Angrisani, and R. S. L. Moriello, "A new measurement method based on music algorithm for through-the-wall detection of life signs," *IEEE Transactions on Instrumentation and Measurement*, vol. 62, no. 1, pp. 13–26, 2012.

[27] G. Gennarelli, G. Vivone, P. Braca, F. Soldovieri, and M. G. Amin, "Multiple extended target tracking for through-wall radars," *IEEE Transactions on Geoscience and Remote Sensing*, vol. 53, no. 12, pp. 6482–6494, 2015.

[28] I. Kurtoğlu, M. Çayören, and ı. H. Çavdar, "Microwave imaging of electrical wires with MUSIC algorithm," *IEEE Geoscience and Remote Sensing Letters*, vol. 16, no. 5, pp. 707–711, 2018.

[29] V. Odedo, *High Resolution Time Reversal (TR) Imaging Based on Spatio-Temporal Windows*. PhD thesis, The University of Manchester (United Kingdom), 2017.

[30] O. P. Gandhi, B. Gao, and J. Chen, "A frequency-dependent finite-difference time-domain formulation for general dispersive media," *IEEE Transactions on Microwave Theory and Techniques*, vol. 41, pp. 658–665, Apr. 1993.

[31] J. P. Bérenger, "Numerical reflection from FDTD-PMLs: a comparison of the split PML with the unsplit and CFS PMLs," *IEEE Transactions on Antennas and Propagation*, vol. 50, pp. 258–265, Mar. 2002.

[32] M. Fink, C. Prada, F. Wu, and D. Cassereau, "Self focusing in inhomogeneous media with time reversal acoustic mirrors," in *Proceedings., IEEE Ultrasonics Symposium,*, pp. 681–686, IEEE, 1989.

[33] R. Sorrentino, L. Roselli, and P. Mezzanotte, "Time reversal in finite difference time domain method," *IEEE Microwave and Guided Wave Letters*, vol. 3, no. 11, pp. 402–404, 1993.

[34] H. Tortel, G. Micolau, and M. Saillard, "Decomposition of the time reversal operator for electromagnetic scattering," *Journal of electromagnetic waves and applications*, vol. 13, no. 5, pp. 687–719, 1999.

[35] G. Lerosey, J. De Rosny, A. Tourin, A. Derode, G. Montaldo, and M. Fink, "Time reversal of electromagnetic waves," *Physical review letters*, vol. 92, no. 19, p. 193904, 2004.

[36] J. de Rosny, G. Lerosey, and M. Fink, "Theory of electromagnetic time-reversal mirrors," *IEEE Transactions on Antennas and Propagation*, vol. 58, no. 10, pp. 3139–3149, 2010.

[37] W. M. G. Dyab, T. K. Sarkar, A. García-Lampérez, M. Salazar-Palma, and M. A. Lagunas, "A critical look at the principles of electromagnetic time reversal and its consequences," *IEEE Antennas and Propagation Magazine*, vol. 55, no. 5, pp. 28–62, 2013.

[38] M. E. Yavuz, *Time reversal based signal processing techniques for ultrawideband electromagnetic sensing in random media*. PhD thesis, The Ohio State University, 2007.

[39] M. Fink, "Time-reversal acoustics in complex environments," *GEOPHYSICS*, vol. 71, no. 4, pp. SI151–SI164, 2006.

[40] M. E. Yavuz and F. L. Teixeira, "Ultrawideband microwave sensing and imaging using time-reversal techniques: A review," *Remote Sensing*, vol. 1, no. 3, pp. 466–495, 2009.

[41] A. Devaney, "Time reversal imaging of obscured targets from multistatic data," *IEEE Transactions on Antennas and Propagation*, vol. 53, pp. 1600–1610, May 2005.

[42] N. Nikolova, *Introduction to Microwave Imaging*. EuMA High Frequency Technologies Series, Cambridge University Press, 2017.

[43] C. Prada, S. Manneville, D. Spoliansky, and M. Fink, "Decomposition of the time reversal operator: Detection and selective focusing on two scatterers," *The Journal of the Acoustical Society of America*, vol. 99, no. 4, pp. 2067–2076, 1996.

[44] M. Fink, D. Cassereau, A. Derode, C. Prada, P. Roux, M. Tanter, J.-L. Thomas, and F. Wu, "Time-reversed acoustics," *Reports on progress in Physics*, vol. 63, no. 12, p. 1933, 2000.

[45] M. E. Yavuz and F. L. Teixeira, "On the sensitivity of time-reversal imaging techniques to model perturbations," *IEEE Transactions on Antennas and Propagation*, vol. 56, no. 3, pp. 834–843, 2008.

[46] J. Ebrahimi-Zadeh, M. Dehmollaian, and K. Mohammadpour-Aghdam, "Electromagnetic time-reversal imaging of pinholes in pipes," *IEEE Transactions on Antennas and Propagation*, vol. 64, no. 4, pp. 1356–1363, 2016.

[47] M. H. Bah, J.-S. Hong, and D. A. Jamro, "UWB patch antenna and breast mimicking phantom design and implementation for microwave breast cancer detection using time reversal MUSIC," *Microwave and Optical Technology Letters*, vol. 58, no. 3, pp. 549–554, 2016.

[48] C. Prada and M. Fink, "Eigenmodes of the time reversal operator: A solution to selective focusing in multiple-target media," *Wave motion*, vol. 20, no. 2, pp. 151–163, 1994.

[49] M. H. Bah, J. Hong, and D. A. Jamro, "Ground slotted monopole antenna design for microwave breast cancer detection based on time reversal MUSIC," *Progress In Electromagnetics Research C*, vol. 59, pp. 117–126, 2015.

[50] H. Lev-Ari and A. J. Devaney, "The time-reversal technique re-interpreted: subspace-based signal processing for multi-static target location," in *Proceedings of the 2000 IEEE Sensor Array and Multichannel Signal Processing Workshop. SAM 2000 (Cat. No.00EX410)*, pp. 509–513, 2000.

[51] G. Micolau and M. Saillard, "D.o.r.t. method as applied to electromagnetic subsurface sensing," *Radio Science*, vol. 38, no. 3, pp. 4–1–4–12, 2003.

[52] E. A. Marengo, F. K. Gruber, and F. Simonetti, "Time-reversal MUSIC imaging of extended targets," *IEEE Transactions on Image Processing*, vol. 16, pp. 1967–1984, Aug. 2007.

[53] W. Zhang, A. Hoorfar, and L. Li, "Through-the-wall target localization with time reversal MUSIC method," *Progress in Electromagnetics Research*, vol. 106, pp. 75–89, 2010.

[54] A. E. Fouda and F. L. Teixeira, "Imaging and tracking of targets in clutter using differential time-reversal techniques," *Waves in Random and Complex Media*, vol. 22, no. 1, pp. 66–108, 2012.

[55] M. Davy, T. Lepetit, J. de Rosny, C. Prada, and M. Fink, "Detection and imaging of human beings behind a wall using the DORT method," *Progress in Electromagnetics Research*, vol. 110, pp. 353–369, 2010.

[56] Y.-S. Yoon and M. G. Amin, "High-resolution through-the-wall radar imaging using beamspace MUSIC," *IEEE Transactions on Antennas and Propagation*, vol. 56, no. 6, pp. 1763–1774, 2008.

[57] G. Zhang, W. W. Wang, and W. Wang, "Energy estimation based TR-MUSIC microwave imaging for extended targets," *Progress in Electromagnetics Research*, vol. 47, pp. 107–126, 2013.

[58] X. Zhong, C. Liao, and W. Lin, "Space-frequency decomposition and time-reversal imaging," *IEEE Transactions on Antennas and Propagation*, vol. 63, no. 12, pp. 5619–5628, 2015.

[59] D. Ciuonzo and P. S. Rossi, "Noncolocated time-reversal MUSIC: High-SNR distribution of null spectrum," *IEEE Signal Processing Letters*, vol. 24, no. 4, pp. 397–401, 2017.

[60] H. Zhao, "Analysis of the response matrix for an extended target," *SIAM Journal on Applied Mathematics*, vol. 64, no. 3, pp. 725–745, 2004.

[61] C. Fan, L. Yang, S. Wu, and Y. Zhao, "Ultrasonic time reversal based imaging for extended target," in *2019 Far East NDT New Technology & Application Forum (FENDT)*, pp. 1–5, IEEE, 2019.

[62] S. Hou, K. Solna, and H. Zhao, "A direct imaging algorithm for extended targets," *Inverse Problems*, vol. 22, no. 4, p. 1151, 2006.

[63] S. Hou and S. Zhang, "An improved imaging method for extended targets," *Journal of Computational Physics*, vol. 333, pp. 321–330, 2017.

[64] B. Hu, X. Cao, L. Zhang, and Z. Song, "Weighted space-frequency time-reversal imaging for multiple targets," *IEEE Signal Processing Letters*, vol. 26, no. 6, pp. 858–862, 2019.

[65] C. Balanis, *Advanced Engineering Electromagnetics*. CourseSmart Series, Wiley, 2012.

[66] C. Johnk, *Engineering Electromagnetic Fields and Waves*. Wiley, 1988.

[67] M. Pastorino and A. Randazzo, *Microwave Imaging Methods and Applications*. Artech House microwave library, Artech House, 2018.

[68] M. Tanter, J.-L. Thomas, and M. Fink, "Focusing and steering through absorbing and aberrating layers: Application to ultrasonic propagation through the skull," *The Journal of the Acoustical Society of America*, vol. 103, no. 5, pp. 2403–2410, 1998.

[69] T. Folégot, C. Prada, and M. Fink, "Resolution enhancement and separation of reverberation from target echo with the time reversal operator decomposition," *The Journal of the Acoustical Society of America*, vol. 113, no. 6, pp. 3155–3160, 2003.

[70] K. Yee, "Numerical solution of initial boundary value problems involving Maxwell's equations in isotropic media," *IEEE Transactions on Antennas and Propagation*, vol. 14, no. 3, pp. 302–307, 1966.

[71] A. M. Abduljabbar, M. E. Yavuz, F. Costen, R. Himeno, and H. Yokota, "Frequency dispersion compensation through variable window utilization in time-reversal techniques for electromagnetic waves," *IEEE Transactions on Antennas and Propagation*, vol. 64, pp. 3636–3639, Aug. 2016.

[72] L. Peretto, R. Sasdelli, and R. Tinarelli, "Uncertainty propagation in the discrete-time wavelet transform," *IEEE Transactions on Instrumentation and Measurement*, vol. 54, no. 6, pp. 2474–2480, 2005.

[73] I. L. S. Braga and F. S. Moraes, "High-resolution gathers by inverse Q filtering in the wavelet domain," *GEOPHYSICS*, vol. 78, no. 2, pp. V53–V61, 2013.

[74] M. E. Yavuz and F. L. Teixeira, "Space-frequency ultrawideband time-reversal imaging," *IEEE Transactions on Geoscience and Remote Sensing*, vol. 46, pp. 1115–1124, Apr. 2008.

[75] A. E. Fouda and F. L. Teixeira, "Imaging and tracking of targets in clutter using differential time-reversal techniques," *Waves in Random and Complex Media*, vol. 22, no. 1, pp. 66–108, 2012.

[76] A. E. Fouda and F. L. Teixeira, "Performance of differential time-reversal for imaging and tracking of targets in clutter," in *2011 IEEE International Symposium on Antennas and Propagation (APSURSI)*, pp. 2565–2568, 2011.

[77] W. Verhelst, "Overlap-add methods for time-scaling of speech," *Speech Communication*, vol. 30, no. 4, pp. 207–221, 2000.

[78] P. S. Addison, *The Illustrated Wavelet Transform Handbook: Introductory Theory and Applications in Science, Engineering, Medicine and Finance, Second Edition*. CRC Press, 2017.

[79] M. J. Shensa, "The discrete wavelet transform: wedding the À Trous and Mallat algorithms," *IEEE Transactions on Signal Processing*, vol. 40, no. 10, pp. 2464–2482, 1992.

[80] C. Torrence and G. P. Compo, "A practical guide to wavelet analysis," *Bulletin of the American Meteorological Society*, vol. 79, no. 1, pp. 61–78, 1998.

[81] M. Farge, "Wavelet transforms and their applications to turbulence," *Annual review of fluid mechanics*, vol. 24, no. 1, pp. 395–458, 1992.

[82] L. Angrisani, P. Daponte, M. D'apuzzo, and A. Testa, "A measurement method based on the wavelet transform for power quality analysis," *IEEE Transactions on Power Delivery*, vol. 13, no. 4, pp. 990–998, 1998.

[83] S. D. Meyers, B. G. Kelly, and J. J. O'Brien, "An introduction to wavelet analysis in oceanography and meteorology: With application to the dispersion of Yanai waves," *Monthly Weather Review*, vol. 121, no. 10, pp. 2858–2866, 1993.

[84] E. Sitnikova, A. E. Hramov, A. A. Koronovsky, and G. van Luijtelaar, "Sleep spindles and spike–wave discharges in EEG: Their generic features, similarities and distinctions disclosed with Fourier transform and continuous wavelet analysis," *THE JOURNAL OF NEUROSCIENCE METHODS*, vol. 180, no. 2, pp. 304 – 316, 2009.

[85] Y. Wang, "Q analysis on reflection seismic data," *Geophysical Research Letters*, vol. 31, no. 17, 2004.

[86] Y. Wang, "Inverse Q -filter for seismic resolution enhancement," *GEOPHYSICS*, vol. 71, no. 3, pp. V51–V60, 2006.

[87] Y. Wang, *Seismic Inverse Q Filtering*. Wiley, 2009.

[88] M.-C. Huang, "Wave parameters and functions in wavelet analysis," *Ocean Engineering*, vol. 31, no. 1, pp. 111 – 125, 2004.

[89] R. Carmona, W. Hwang, and B. Torresani, *Practical Time-Frequency Analysis: Gabor and Wavelet Transforms, with an Implementation in S*. ISSN, Elsevier Science, 1998.

[90] A. Deliu and B. Deng, "On progressive functions," *Journal of Mathematical Analysis and Applications*, vol. 423, no. 1, pp. 336–357, 2015.

[91] Y. Huang and D. Parsons, "A time domain approach for measuring the dielectric properties and thickness of walls of a building," in *IEE Colloquium on Propagation Aspects of Future Mobile Systems (Digest No: 1996/220)*, pp. 7/1–7/7, Oct. 1996.

[92] A. Thiry, *Efficient FDTD for broadband systems*. The University of Manchester (United Kingdom), 2006.

[93] F. Costen, J.-P. Bérenger, and A. K. Brown, "Comparison of FDTD hard source with FDTD soft source and accuracy assessment in Debye media," *IEEE Transactions on Antennas and Propagation*, vol. 57, no. 7, pp. 2014–2022, 2009.

[94] T. D. Bufler, R. M. Narayanan, and T. Dogaru, "Radar signatures of furniture elements," *IEEE Transactions on Aerospace and Electronic Systems*, vol. 51, pp. 521–535, Jan. 2015.

[95] RIKEN, Wako Saitama, Japan, "Media parameters for the Debye relaxation model." `http://cfd-duo.riken.jp/cbms-mp/`. [Online; accessed 20-February-2020].

[96] S. M. Moghadasi and M. Dehmollaian, "Buried-object time-reversal imaging using UWB near-ground scattered fields," *IEEE Transactions on Geoscience and Remote Sensing*, vol. 52, pp. 7317–7326, Nov. 2014.

[97] D. Liu, G. Kang, L. Li, Y. Chen, S. Vasudevan, W. Joines, Q. H. Liu, J. Krolik, and L. Carin, "Electromagnetic time-reversal imaging of a target in a cluttered environment," *IEEE Transactions on Antennas and Propagation*, vol. 53, no. 9, pp. 3058–3066, 2005.

[98] M. Pastorino, *Microwave Imaging*. Wiley Series in Microwave and Optical Engineering, Wiley, 2010.

[99] K. Aldape, K. M. Brindle, L. Chesler, R. Chopra, A. Gajjar, M. R. Gilbert, N. Gottardo, D. H. Gutmann, D. Hargrave, E. C. Holland, D. T. W. Jones, J. A. Joyce, P. Kearns, M. W. Kieran, I. K. Mellinghoff, M. Merchant, S. M. Pfister, S. M. Pollard, V. Ramaswamy, J. N. Rich, G. W. Robinson, D. H. Rowitch, J. H. Sampson, M. D. Taylor, P. Workman, and R. J. Gilbertson, "Challenges to curing primary brain tumours," *Nature Reviews Clinical Oncology*, vol. 16, no. 8, pp. 509–520, 2019.

[100] R. L. Siegel, K. D. Miller, and A. Jemal, "Cancer statistics, 2016," *CA: A Cancer Journal for Clinicians*, vol. 66, no. 1, pp. 7–30, 2016.

[101] E. J. Joseph, K. A. H. Ping, K. Kipli, D. A. A. Mat, S. Sahrani, D. N. A. Zaidel, M. I. Sariphn, and M. H. Marhaban, "Integration of image segmentation method in inverse scattering for brain tumour detection," *Progress in Electromagnetics Research*, vol. 61, pp. 111–122, 2017.

[102] T. Wuren, T. Takai, M. Fujii, and I. Sakagami, "Effective 2-debye-pole FDTD model of electromagnetic interaction between whole human body and UWB radiation," *IEEE Microwave and Wireless Components Letters*, vol. 17, pp. 483–485, July 2007.

[103] C. Gabriel, S. Gabriel, and y. E. Corthout, "The dielectric properties of biological tissues: I. Literature survey," *PHYSICS IN MEDICINE AND BIOLOGY*, vol. 41, no. 11, p. 2231, 1996.

[104] S. Gabriel, R. Lau, and C. Gabriel, "The dielectric properties of biological tissues: II. Measurements in the frequency range 10 Hz to 20 GHz," *PHYSICS IN MEDICINE AND BIOLOGY*, vol. 41, no. 11, p. 2251, 1996.

[105] D. Yoo, "The dielectric properties of cancerous tissues in a nude mouse xenograft model," *Bioelectromagnetics*, vol. 25, no. 7, pp. 492–497, 2004.